Team AeroSwitch presents

TRYBRID - A new concept for GA trainer

AIAA Graduate Team Aircraft Competition 2019-2020

AERO SWITCH

Design project submitted in May 2020

POLITECNICO
MILANO 1863

Team members

Lorenzo Alberti
AIAA Number 1097797

Davide Pasquali - Team leader
AIAA Number 1070899

Andrea Santeramo
AIAA Number 1097796

Matteo Tombolini
AIAA Number 1097798

Team advisors

Lorenzo Trainelli
AIAA Number 436564

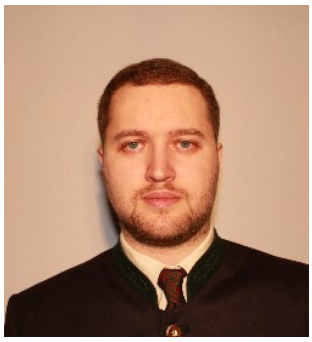

Carlo E.D. Riboldi
AIAA Number 1083869

Executive summary

In response to the Request For Proposal of the 2019-2020 American Institute of Aeronautics and Astronautics (AIAA) Graduate Team Aircraft Design Competition, the AeroSwitch team has the great honor to present the *Trybrid* (trainer + hybrid), a new concept for General Aviation (GA) trainer. The study starts with market analysis and descriptions of the design methods. The core is devoted to the innovative idea on which *Trybrid* is based: exploit the hybrid-electric propulsion to overcome the dualism between single-engine and multi-engine aircraft and revolutionize the GA world. Subsequently, performance and cost analysis are performed, along with certification and safety considerations. *Trybrid* has an innovative key feature: it is technically multi-engine, but flyable as a single-engine under all respects (including typical flight characteristics and handling qualities) by a single-engine rated pilot. Furthermore, it is capable of flying even at 160 knots true airspeed and up to FL230 in full instrument meteorological condition. It is equipped with anti-ice system and autopilot, while hybrid propulsion guarantees a hourly cost well below its competitors. Finally, *Trybrid* can be easily converted to pure-electric propulsion, conveniently trading off range performance with higher comforts standards and lower operating costs.

Contents

List of symbols and acronyms

Symbols

Symbol	Definition	Unit
α	Angle of attack	deg
β	Sideslip angle	deg
δ	Control surface deflection	deg
δ_T	Thrust lever setting percentage	–
η	Efficiency	–
γ	Flight path angle	deg
λ	Taper ratio	–
$\mathbb{E}$	Energy density	Wh/kg
$\mathbb{P}$	Power density	W/kg
$\mathcal{E}$	Endurance	h
$\mathcal{L}, \mathcal{M}, \mathcal{N}$	Rolling, pitching, yawing moments	N m
$\mathcal{R}$	Range	NM
$\mathcal{T}$	Period of oscillation	s
AR	Aspect ratio	–
ϕ	Bank angle	deg
ρ	Density	kg/m^3
σ	Crab angle	deg
σ	Stress	Pa
τ	Control surface effectiveness parameter	–
ξ	Non-dimentional x-axis coordinate	–
b	Span	m
c	Mean aerodynamic chord	m
C_d, C_l, C_m	2D drag, lift, pitching moment coefficients	–
c_p	Brake specific fuel consumption	N/(W s)
C_{D_0}	Zero-lift drag coefficient	–
D, Y, L	3D Drag, sideforce, lift	N
E	Energy	J, Wh
e	Oswald's efficiency factor	–
F	Control force	N, lbs
F	Power index	–
f	Frequency	Hz
G	Gearing ratio	rad/ft
g	Gravitational acceleration	m/s^2
h	Altitude	ft
H_n	Static margin	–
i	Incidence	deg
K	Induced drag coefficient	–
L/D	Lift-to-drag ratio	–
L_t	Distance between AC of the wing and of the tail	m
L_{TO}	Take-off length	m, ft
M	Mach number	–
m	Mass	kg
M_h	Hinge moment	N m
n	Load factor	–

P	Power	W, hp
p, q, r	Roll, pitch, yaw rates	rad/s
P_b	Shaft brake power	W, hp
q	Dynamic pressure	Pa
Re	Reynolds number	–
S	Surface	m^2, ft^2
T	Temperature	°C
t	Thickness	m
V	Airspeed	m/s, kt
V_A	Maneuvering speed	m/s, kt
V_D	Design diving speed	m/s, kt
V_F	Designed flap speed	m/s, kt
V_V	Vertical speed	fpm, m/s
V_X	Steepest climb speed	kt
V_Y	Fastest climb speed	kt
V_1	Take-off decision speed	kt
V_{NE}	Velocity never exceed	m/s, kt
V_{ht}, V_{vt}	Horizontal and vertical tail volume coefficients	–
$V_{max\mathcal{E}}$	Max endurance speed	kt
$V_{max\mathcal{R}}$	Max range speed	kt
V_{MC3}	Velocity minimum control with 3 EMI	kt
V_{S0}	Stall speed with fully deployed flaps	kt
V_{S1}	Stall speed in clean configuration	kt
W	Weight	N, lbs

Super/subscripts

Symbol	**Definition**
a	Airframe or aileron
bat	Batteries
C	Cruise
e	Elevator
est	Estimated
F	Fuel
f	Flap
fus	Fuselage
h	Hinge
ht	Horizontal tail
$misc$	Miscellaneous
p	Propulsive
pl	Payload
r	Rudder
rec	Recharge
ref	Reference
$regr$	Regression
t	Trim tab
vt	Vertical tail
w	Wing
wet	Wetted

Abbreviations and acronyms

(M)TO M/W	(Max)Take-Off Mass/Weight
AC	Aerodynamic Center
AOA	Angle Of Attack
AV	AVionic system
BP	Battery Pack
C/E/T AS	Calibrated/Equivalent/True Airspeed
CAD	Computer Aided Graphics
CFD	Computational Fluid Dynamics
CG	Center of Gravity
DEP	Distributed Electric Propulsion
DR	Dutch Roll
EM	Electric Motor
EPMS	Energy and Propulsion Management System
ESC	Electronic Speed Controller
FAR	Federal Aviation Regulation
FL	Flight Level
FQ	Flying Qualities
GA	General Aviation
HE	Hybrid Electric
HUMS	Health and Usage Monitoring System
ICE	Internal Combustion Engine
IFR	Instrument Flight Rules
IMU	Inertial Measurement Unit
ISA	International Standard Atmosphere
L/T E	Leading/Trailing Edge
LND	Landing
MAC	Mean Aerodynamic Chord
ME	Multi Engine
MEW	Maximum Empty Weight
MFD	Multi-Function Display
NC	Non-Continuous
OEI	One Engine Inoperative
OEMI	One Electric Motor Inoperative
P/C PL	Private/Commercial Pilot License
PE	Pure Electric
PFD	Primary Flight Display
PGS	Power Generation System
PH	Phugoid
PIC	Pilot In Command
SE	Single Engine
SEP	Single Engine Piston
SMP	Sizing Matrix Plot
SP	Short Period
TBO	Time Between Overhaul
TO	Take-Off
VFR	Visual Flight Rules
ZL	Zero-Lift

1. Market analysis

1.1 Introduction

Environmental sustainability is nowadays one of the biggest issues faced by mankind. Everyone should never forget what sustainability means: «Development that meets the needs of the present without compromising the ability of future generations to meet their own needs».

AIAA's RFP for GA Trainer Family for Graduate Student highlights how the average age of airline pilots is increasing, while the number of military pilots decreases. To make this framework worse, worldwide civil pilot number is decreasing but the number of airliners routes and markets is enlarging.

A possible way to face this issue is to look at past, present and future GA market. Key strengths of existing aircraft are taken as reference, leading to the decision of a traditional design from aerodynamics and structural point of view to make it easy to fly and affordable. Furthermore all design choices are made focusing on a trainer aircraft. To reduce pollution, noise and costs, the first aim is to build a hybrid aircraft, but it is not enough: to go further in cost reduction, but at the same time increase safety level, a single aircraft responding to ME and SE has been envisioned.

1.2 Technological context and global pollution

These are revolutionary days: worldwide internet connection rapidly grows, smartphones and personal computer are fast and affordable, "4.0" industry and electric cars market is booming thanks to every day more reliable and capable batteries. In this revolutionary framework, aviation starts to peer out with concepts and ideas, but still fails to catch up.

Many airports, either small or big, are experiencing many issues with neighbor communities regarding noise and atmospheric pollution. National aviation agencies developed approach and departure procedures specifically designed for noise abatement [54] and introduced additional fees both for commercial and general aviation airports [14]. In the same way greenhouse emissions responsible for climate change must be reduced, even if aviation only represents a small percentage of World's total emissions, with GA even less.

Propulsive electric motors and specifically designed propellers can help cutting down noise, especially in terminal airspace [15]; an electric or hybrid aircraft can cut pollution near to airports [16], even if battery production and disposal is still an issue.

Necessity of hybrid propulsion is due to low specific energy content of modern battery packs: while *AVGAS 100LL* is around 44 MJ/kg, state-of-the-art batteries can barely reach 1 MJ/kg [17], making a huge bottleneck in electric aircraft development. Hybrid-electric aircraft seems to be the connection between yesterday's and tomorrow's powertrain, assuring noise and greenhouse abatement close to airports area and assuring good range performance [18].

Electric propulsion brings many advantages: low maintenance of electric motors, less bulkiness, less vibrations and a negligible effect of altitude on power available. This latter aspect leads not only to high ceilings and climb rate, but also to high true airspeed with small used power. Electric propulsion even allows new and alternative motor positioning, for instance distribute propulsion, which promise major advantages in lift-to-drag ratio [19].

1.3 Present GA fleet, training and competitors

Analyzing the General Aviation fleet spread in the US, from the yearly FAA survey [55] at the end of 2018 there were 143,040 active GA piston aircraft: 75% of these are for personal use, while 10% for training purposes. Of the total amount, just 9% are twin-engine, despite being

safer. This tendency could be justified being a twin-engine more costly than a single-engine, hence non-affordable by the majority of pilots or student pilots (hourly rate in Table 8.1).

A research on collegiate aviation schools [20] shows that 65% of employed aircraft are *Cessna 172* and *Piper Warrior*. These aircraft are basically designed in the '50s, and 29% of in-service aircraft have more than 20 years. *Cessna* still governs piston engine market, even if an opening towards other manufacturers is noticeable; in 1999 50% of total GA piston aircraft sold were *Cessna*, and in 2009 this falls to 36%[21]. Pilot training is also evolving; following some accidents involving spatial disorientation and upset recovery, for instance *AF 447*, national agencies emitted recommendations for improving flight training [22, 56].

From these considerations and from forecast on the increasing number of commercial pilots needed, as emphasized by RFP, comes the necessity of a brand new affordable and reliable aircraft trainer, able to train pilots in the new evolving scenario, speaking of which main competitors are in Table 1.1. In this respect, *C-172*, *C-152*, *PA-28* and *PA-44* are old designs with intrinsic limitations, even if newly built. *Cirrus SR-22* and twin-engine *Diamond DA-42* are newly thought, but performance oriented, high-end products cruising fast and in luxurious comfort. *Tecnam P2006T* is the cheapest twin-engine on the market, both in procurement and operating costs, but powered by a traditional powertrain, and obviously more expensive than a single-engine. *Pipistrel Panthera Hybrid* will probably be the first hybrid aircraft to be produced in series, with many advantages on competitors; however, it is based on *Panthera*, with a traditional powertrain, and not training oriented, as well as *SR-22*.

	C172R	**SR22**	**Panthera-H**	**PA44**	**DA42**	**P2006T**
MTOM	1043 kg	1026 kg	1315 kg	1724 kg	1785 kg	1180 kg
Power	160 hp	310 hp	272 hp	2 x 180 hp	2 x 135 hp	2 x 98 hp
Max range	580 nm	660 nm	$>$ 1000 nm	820 nm	917 nm	620 nm
Cost	274 900 $	629 900 $	$<$ 500 000 $	663 500 $	650 000 $	443 900 $

Tab. 1.1: Main on-market competitors

1.4 Survey

In order to better understand market needs, the Team released a survey addressed to flight schools in USA and Canada. Answers came from 55 different organizations. Survey population is described in Figure 1.1 in terms of number of owned aircraft.

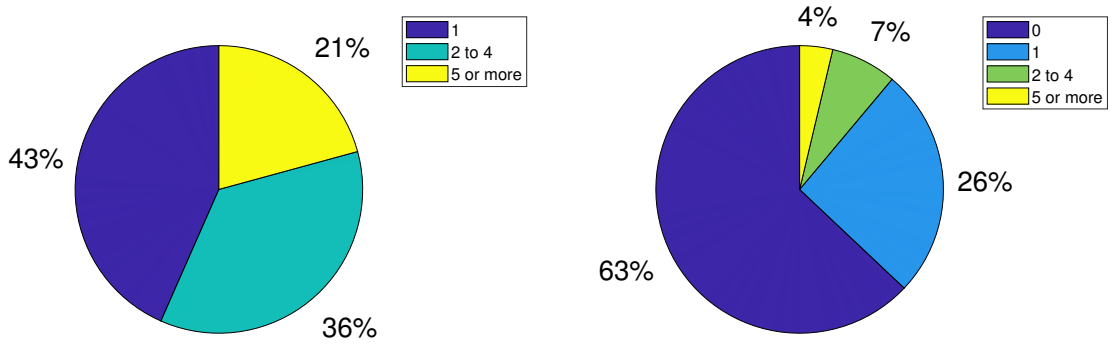

(a) Single engine **(b)** Twin engine

Fig. 1.1: Number of owned planes

Organizations were classified as small, medium and big also according to hours flown, that goes from less than 150 h per year to more than 6000 h.

One of the first questions examined what **kind of missions** are done and how often long-transfer missions are practiced. Results in Figure 1.2 show that great part of training missions last less than 2 h.

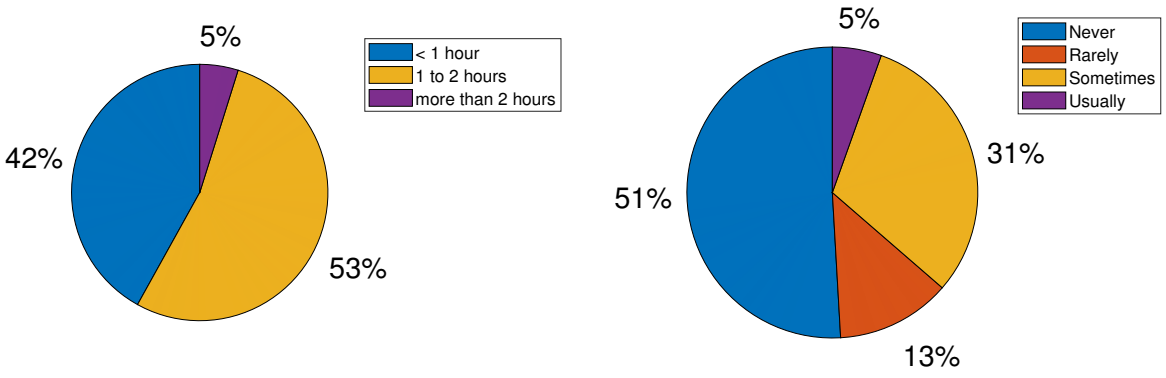

(a) Typical training mission duration **(b)** 800 nm mission frequency

Fig. 1.2: Typical mission flown

The third part of the survey concerned **maintenance staff** of the organizations. It was inquired whether organizations did maintenance on their own flying field and consequently if they had technicians employed on a regular basis or on call. Results in Figure 1.3 show that the majority of the organizations have stably employed technicians. This would mean better maintenance performance in case recursive intervention on the aircraft was needed (e.g. battery substitution between flights).

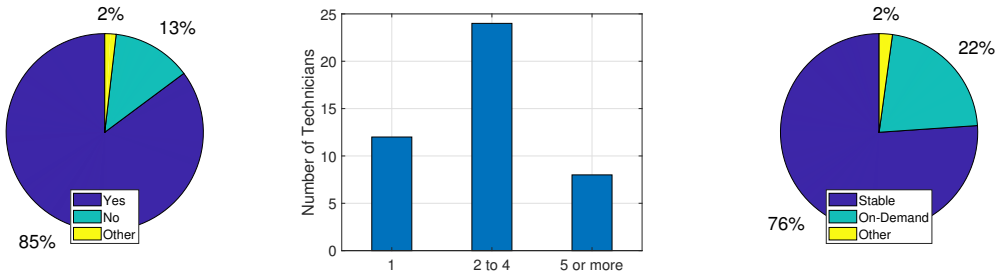

(a) Maintenance done at field **(b)** Technicians employed **(c)** Technicians agreement

Fig. 1.3: Maintenance topic

Fuel availability is an important topic: understanding what kind of fuel organizations already have is crucial to discriminate between different engine technologies. For example, the adoption of fuel cells would be a problem, as no one of the respondents had hydrogen tanks in their flying field. Figure 1.4 shows availability of different aeronautical fuels: it is clear how *MOGAS* is less diffused than the others, but hopefully its diffusion will increase [23].
Figure 1.5 reports statistics about **costs breakdown**: the most oppressive item is fuel, equated by overhaul and maintenance altogether.

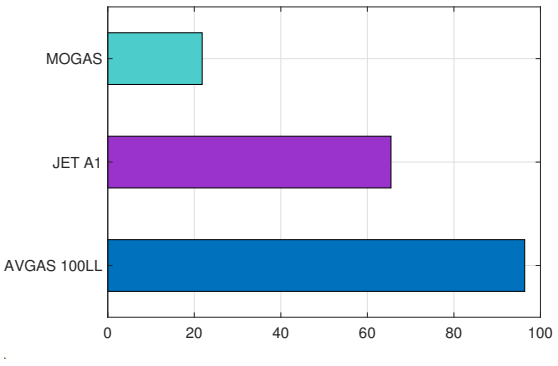

Fig. 1.4: Fuel availability at flying fields

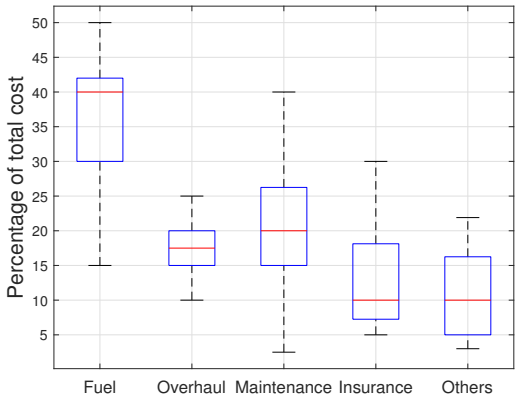

Fig. 1.5: Cost breakdown for a flight hour

In conclusion, the Team asked for personal considerations and if the respondents would buy an aircraft with a non-traditional configuration (like a canard configuration or a tandem wing) in case this would provide better performance. Results of this inquiry are reported in Figure 1.6, which points out how "General Aviation people" are conservative: only 12% of interviewed said "Yes" to a configuration different from commonality, despite potential advantages. Furthermore 53% of respondents answered with a straight "No", whereas 35% of them are not sure. This is of course a deterrent for alternative configurations.

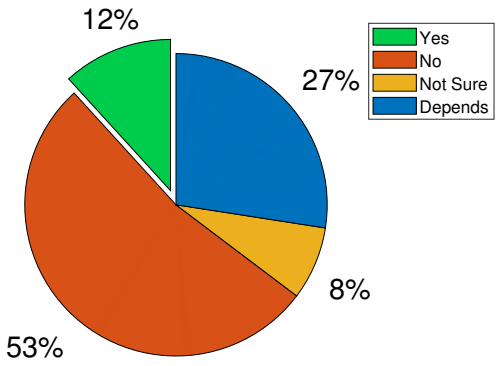

Fig. 1.6: Non-traditional configuration approval

Some of the received personal opinions are reported in the following:

> *"Cessna 172 best; Diamond DA20/DA40 worst: very expensive and don't hold up as well as the Cessnas"*
>
> *"Cessna C172S: Extremely durable, airframe is metal and very easy to maintain"*
>
> *"We do not find Continental engines to be robust when compared to the Lycoming; engine that have a gearbox is an added cost."*
>
> *"I think electric propulsion is going to be what I will look for next. High wing is much preferred for fixed gear airplanes."*
>
> *"Cost is always a consideration, but I feel the future is electric"*
>
> *"We do not look for high performance in a trainer. At present most non-traditional aircraft are built of composite material which is difficult to repair in the field."*

To sum up, what emerges from market analysis is that the aircraft should be **easy to fly** and **to maintain**, being **simply constructed**. Moreover, they must **reduce pollution and noise**, being **safer** and **cheaper** than competitors. Their operational employment must cover several types of missions, with **training in the first place**. This implies the aircraft must be able to spin and do upset training, with performances that could even satisfy **private customers**.

2. Preliminary studies

2.1 Initial concept

2.1.1 Choice of the powertrain

Adopting a traditional powertrain system would be the simplest and easiest solution, but this hackneyed technology is affected by intrinsic issues, such as noise and pollution. Conversely, a pure-electric aircraft coping with requirements is not feasible with today or 2025 technology, due to the limited energy density of batteries. To accomplish the 1000 NM ferry range mission, a preliminary calculation shows that for an aircraft with a MTOM of 1000 kg it would be necessary the energy stored into a 3.7 t battery pack.

The best solution seems to be a trade-off: **hybrid-electric propulsion** with a **series architecture**, allowing to accomplish **terminal maneuver in full-electric mode** to cut down greenhouse gases emission and noise in proximity of the flying field. Then, a **power generation system** (PGS) used as **range-extender** to fulfill range and endurance requirements. Moreover, aircraft and PGS integration will be designed to allow to unload PGS and substitute it with a battery pack of same weight and balance to allow aircraft full-electric flight of at least 1 hour. Cost reduction would even come from PGS always used in a controlled environment and with TBO referred to real engine-on time, not to be confused with airframe time. This architecture offers the possibility to improve technological level of battery pack at every substitution. This would allow to have an "even more electric aircraft" along its lifespan.

2.1.2 Requirements and preliminary design

Our aircraft should be simply-constructed, easy to fly (as mentioned in the survey) like a *C-172* or *PA-28*, but also maneuverable to cope with step turns or unusual attitude request in training. In order to be inexpensive, they should be designed to be easily and rapidly serviced and repaired.

To reach all goals, making innovation but limiting costs, one focal choice has been performed: **design of just one aircraft satisfying requirements for both SE and ME**, also in terms of certification, training and employment, thanks to a novel design. This new configuration brings in new difficulties, but allows savings in terms of procurement cost, hangar space and spare parts. It will raise aircraft utilization with less off-duty time and also increases safety.

Furthermore, a small flight school could buy just one aircraft still doing SE and ME training, or a big flight school could buy 10 aircraft instead of 18, accounting for spare aircraft.
Indeed, three different preliminary concepts have been investigated:

"Modular Concept" - an aircraft whose configuration could be rapidly changed between 1 electric motor in the nose to 2 electric motors in wings. Disadvantages of this concept are weight, complexity and reliability of such a dismantling system and the necessity of a technician always available to make the swap.

"Tri-Motor Concept" - an aircraft with 1 electric motor in the nose and 2 electric motors in wings, with an on-board device allowing the pilot to fly the aircraft as a SE or ME configuration. Besides advantages such as an increase of safety drawbacks are additional drag and weight and unlikelihood purchase from a private customer with only SEP rating.

"Switch Concept" - an aircraft with motors on wings with fixed configuration, equipped with on-board hardware and software able to let the aircraft fly as a normal multi-engine but also to simulate the single-engine mode controlling electric motors in different manners. This concept got the highest number of pros (high safety, no added drag or weight, no need of ballistic parachute, highly versatile and also possibly simulating other aircraft dynamic), while its cons are basically the certification and regulation aspects.

2.2 Preliminary data collection

2.2.1 Airframe mass estimation

In order to estimate aircraft empty mass, a logarithmic regression as suggested by Roskam has been worked out [1]. It takes into account the airframe mass, namely the empty mass deprived of engine(s) mass, to couple with hybrid-electric propulsion choice. The regression (Figure 2.1a) considers FAR-23 SE and ME 4-seater aircraft from year 2000.

2.2.2 Electric motors

Similarly, a linear regression for existing electric motors has been developed, accounting for EM used in air sports sector. All EM considered present a high efficiency (≥ 0.93). Data in Figure 2.1b are visibly scattered as EM tested for aeronautic applications are few at present.

2.2.3 Power Generation System

Main alternatives for ICE are gasoline reciprocating engines (running on *AVGAS 100LL* or *MOGAS*), diesel piston engines (running on *JET A1*) and small turbine engines. Figure 2.1c collects data related to gasoline engines, from which regression for PGS is obtained adding the weight of electric generator, equivalent with an EM. The same has been done for the other two candidate technologies.

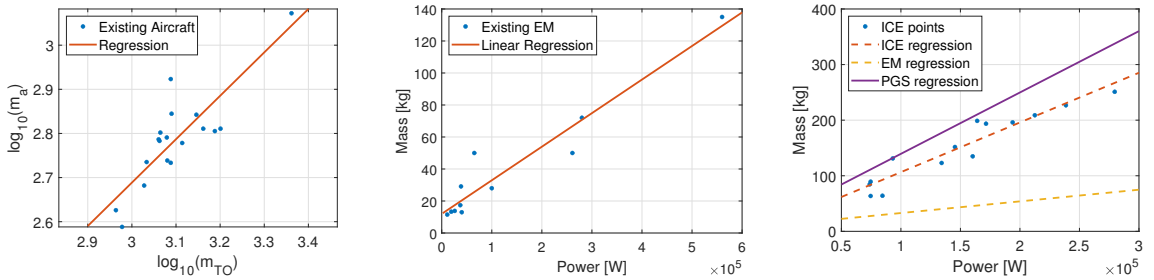

(a) Airframe mass (logarithmic) **(b)** EM **(c)** PGS w/ gasoline engines

Fig. 2.1: Statistical regressions for parameters estimation

2.2.4 Batteries

Batteries are now the biggest bottleneck in the development of hybrid/electric airplanes. Limits in specific energy, safety and durability make a real challenge for an aircraft designer.

The battery pack technology must be safe, reliable and well performing. Three mature battery technologies satisfy these requirements: Lead-based, Nickel-based and Lithium-based. Table 2.1 reports the reference specific energy available on market now for each technology [24]. Comparing the values, it is clear that Lithium-based batteries have the highest one. There are many possible realizations of Lithium batteries, which differ from the internal chemistry. As reported in [24], Lithium Manganese Oxide (LMO) and Lithium Iron Phosphate (LFP) have the lowest specific energy, 140 W h/kg, insufficient for our purposes. Lithium Cobalt Oxide (LCO) is the oldest technology on the market and presents strong limits in safety and availability. The last choice remained between Nickel Cobalt Aluminum (NCA) and Nickel Manganese Cobalt (NMC).

Technology	$\mathbb{E}$ [W h/kg]
Lead-based	50
Nickel-based	80
Lithium-based	200

Tab. 2.1: Specific energy values

NCA batteries have the highest specific energy in the Lithium-ion paramount: they can have

over 260 W h/kg. However, NMC batteries are not far from this value: some realizations have more than 200 W h/kg. Conversely, NMC have longer durability, up to 2000 life cycles [25], while limit for NCA batteries is 1500 [24] and common realizations reach only 500 cycles.

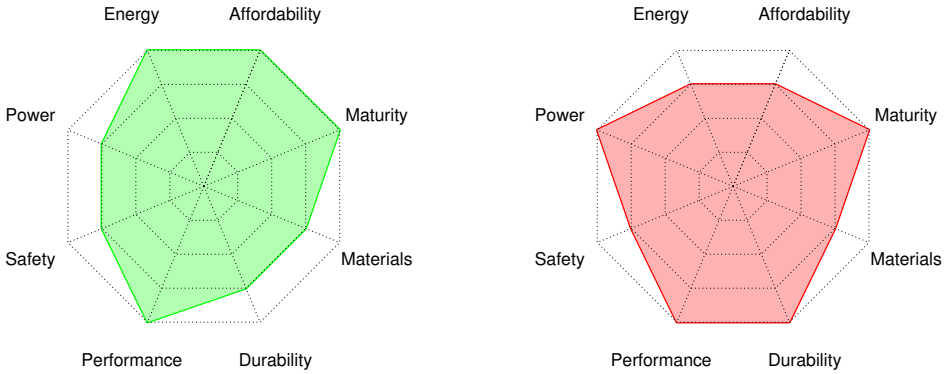

(a) NCA **(b)** NMC

Fig. 2.2: Batteries features diagrams

Previous considerations led to the definition of features diagrams for NCA and NMC, reported in Figure 2.2. Being also the dominant chemistry on market and in EVs industry, the Team selected **NMC chemistry for battery pack**.

The efficiency of the battery pack has been estimated using automotive typical values and it has been assumed of 80% [26]. Assuming an 8% yearly increase [27], specific energy projections are reported in Figure 2.3.

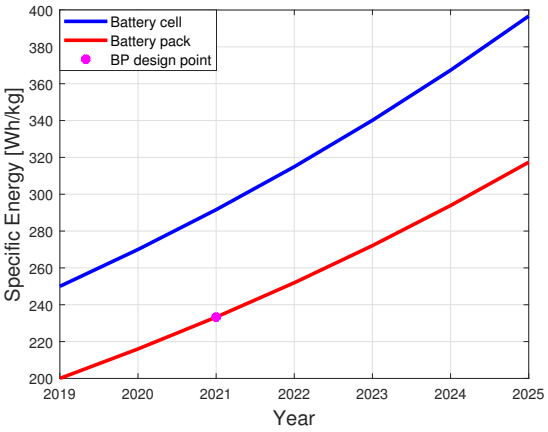

Fig. 2.3: Specific energy projections

As the aircraft must be operative in 2025, it must be realized and tested some years before. So the Team chose the value of **specific energy of 2021**, which is 230 W h/kg. Volumetric specific energy of the cell estimated is instead 450 W h/l.

Specific power depends on many factors, including temperature and state of charge. Studies from [25] suggest NMC models can have a Power/Energy ratio from 6.7 to 8. Thus, it is assumed battery pack has a Power/Energy ratio of 7.

Recharge efficiency of a Lithium-ion battery ranges from 95% to 99% [28]. In order to be conservative, the Team chose the lowest value as reference, so 95%. As a further performance

limitation, the energy that a battery can store drops with use. The battery can be considered exhausted when it cannot be charged more than the 80% of the nominal capacity. A mature NMC battery can have from 1000 to 2000 complete discharge-charge cycles, on average. Assuming that the battery pack will be a high-performance realization operating under challenging conditions, operative life has been estimated in 1000 cycles.
In 2012 the averaged prize of a battery pack was 707 \$/kWh, in 2018 it was 176 \$/kWh and the projection for 2025 is 94 \$/kWh [29].

$\mathbb{E}$ [W h/kg]	$\frac{\mathbb{E}}{V}$ [W h/l]	$\mathbb{P}$ [W/kg]	η_{rec} [−]	η_{bat} [−]	**Life cycles**	**Cost** [$\$_{2025}$/kWh]
230	450	1610	95%	80%	1000	94

Tab. 2.2: Battery parameters recap

Once batteries reach the end of their operative life, they can be reused in second life application, for example in stationary-storage applications. Second-life batteries can reach 200 GW h/y in 2030 [57], avoiding disposal issues and depreciating batteries procurement costs.

2.2.5 Avionics and sub-systems

To estimate aircraft total energetic needs, also avionics and systems power have been considered. For avionics needs, considered required power is that of *Garmin G1000* complete suite in different scenarios [30], accounting also for power required for anti-ice purposes.

2.2.6 Preliminary aerodynamics parameters

Assuming a **parabolic drag polar**, the drag coefficient of an airplane can be written as:

$$C_D = C_{D_0} + \underbrace{\frac{1}{\pi A R e}}_{K} C_L^2 \tag{2.1}$$

Oswald efficiency factor e depends on aspect ratio, whose value has been fixed to $AR = 7$, typical of GA aircraft. Following [2], it is possible to derive $e = 0.84$.

Zero-lift drag build up

Zero-lift drag has been derived following a **bottom-up approach**, as reported in [2]: each contribution to zero-lift drag (wing, fuselage, tail, ...) is evaluated in order to provide aircraft value. As later explained in Section 2.3, this procedure is incorporated in an optimization process for the estimation of aircraft parameters. Thus, input parameters were updated in parallel with results from other preliminary analysis, till overall convergence was achieved.

Each contribution of the wing, fuselage, horizontal and vertical tail depends on:

- *skin friction drag coefficient* C_{fric}

  The extent to which the aircraft has laminar flow over its surfaces is assumed to be 35%, as suggested for a GA aircraft with smooth metal structure. Surface roughness is that of smooth paint.

- *ratio between wetted area and reference area* $\frac{S_{wet}}{S}$

  A uniform airfoil, straight-tapered, unswept wing was assumed. Wing surface and span were guessed at this stage. Their ultimate values are reported in Table 2.7. On the other hand, taper ratio was set at $\lambda = 0.65$, while relative thickness for the wing was $t/c = 0.12$. Selected fuselage fineness ratio is $\lambda_{fus} := \frac{\ell_{fus}}{d_{fus}} = 5.5$. Fuselage length was derived from MTOM estimation considering the statistical power law reported in [1]. In particular, power law coefficients were those of a twin engine aircraft, meaning ultimately $\ell_{fus} = 6.74\,\text{m}$.

  To conclude, tail volume coefficients are respectively $V_{ht} = 0.66$ and $V_{vt} = 0.04$, whereas aspect ratio and taper ratio were chosen in alignment with typical values reported in [3].

- *form factor* FF, computed following [31]

- *interference factor* Q, which takes into account the interference drag

  Adopted values were $Q_w = 1.1$, for the wing, whereas for both horizontal and vertical tail $Q_{ht} = Q_{vt} = 1.04$ were assumed.

Zero-lift drag is thus:

$$C_{D_0} = \sum_{i=1}^{n} C_{fric_i} FF_i Q_i \frac{S_{wet_i}}{S} + \Delta C_{D_0} \tag{2.2}$$

The term ΔC_{D_0} in Equation (2.2) accounts for additive drag, induced by non-smooth components sticking out into the flow. Each of these contributions is expressed making use of related empirical

coefficient $C_{D_\pi} := \frac{D/q}{A_\pi}$, being A_π the frontal area of the component. This coefficient multiplied by frontal area and divided by reference area gives zero-lift drag contribution: $\Delta C_{D_0} = C_{D_\pi} \frac{A_\pi}{S}$. For what concerns landing gear (non-retractable), $C_{D_{\pi_{wheel}}} = 0.15$ has been assumed for both main and nose wheels [4]. Diameter and width of the tires have been set to respectively 15 in and 5 in. The contribution of struts, one per wheel is added as well: circular struts provide $C_{D_{\pi_{strut}}} = 0.3$ [2] and in advance $d_{strut} = 6$ in and $\ell_{strut} = 1$ ft have been assumed.

A further drag source is the cockpit window, due to reduction in airspeed over the geometry. Considered cockpit features a curved windscreen with a sharp upper edge ($C_{D_\pi} = 0.005$) and a frontal area corresponding to the maximum area of the fuselage.

As a result, it is possible to provide an estimation of the overall zero-lift drag, with single contributions reported in Table 2.3. An extra miscellaneous term of 30 drag counts has been added to the total to account for antennas, other surfaces and trim drag.

Component	**Zero-lift drag**
Wing	0.0054
Fuselage	0.0038
Horizontal tail	0.0012
Vertical tail	0.0007
Landing gear	0.0042
Cockpit window	0.0038
Total	**0.0213**

Tab. 2.3: Zero-lift drag build-up

For take-off and landing, effects of flaps (and landing gear if retractable) need to be accounted for, as they are responsible for an increment in zero-lift drag. These increments and decrements of Oswald's efficiency factor are reported in Table 2.4, in accordance with [1].

Configuration	ΔC_{D_0}	C_{D_0}	Δe	e
Take-off	0.015	0.0363	−0.05	0.79
Landing	0.065	0.0863	−0.10	0.74

Tab. 2.4: Zero-lift drag and Oswald's efficiency factor variations at take-off and landing

Maximum-lift coefficient

Maximum-lift coefficient in all three main configurations (with plain/split flap), is assumed following [1]. Values considered are well beneath the state-of-the art: $C_{L_{max}} = 1.4$, $C_{L_{max}}^{TO} = 1.6$ and $C_{L_{max}}^{LND} = 2$.

2.3 Preliminary design parameters

Enforcing parameters assumed in previous sections, take-off mass can be determined. The method used for "traditional" propulsive system is not applicable for a hybrid solution. An iterative **optimal approach** similar to that reported in [32] has been adopted. It is based on:

1. preliminary estimation of parameters and of the design mission;
2. choice of design point on the sizing matrix plot, based on performance requirements;
3. calculation of take-off mass with an optimal numerical procedure based on ICE regressions;
4. re-calculation with a more sophisticated optimizer model, accounting for available ICE;
5. verification of design point on sizing matrix plot;
6. reinstatement of points 1-5 to tune the solution until all requirements are fulfilled and output parameters do not change in a substantial way; conduct a sensitivity analysis in order to consolidate the solution and to be aware of most critical parameters.

2.3.1 Design mission

The optimizer requires a reference mission to calculate aircraft energetic needs. Designed mission should be a trade-off. For example, if sizing was performed to optimize long missions it would lead to a too heavy aircraft. On the contrary, if sizing mission were too short it would move the point far from ferry range requirement, making it unreachable. In addition, for short mission the aircraft is potentially in full-electric configuration, so the hybrid configuration must not overlap the field of missions covered by the pure-electric one. Hence, design mission considers **4 people on-board** (for a mass of 320 kg) and 40 kg of baggage, and consists of:

1. 2 minutes of taxi in electric mode (PGS off) at 10 kt

2. electric take-off
3. electric climb up to a transition altitude *
4. hybrid climb (PGS on) up to cruising altitude
5. **500 NM** cruise, whose range is a trade-off value in operational employment
6. descent to 3000 ft and loiter for 30 minutes
7. descent and landing in electric mode (PGS off)
8. 2 minutes of taxi in electric mode (PGS off) at 10 kt.

2.3.2 Sizing matrix plot

Sizing matrix plot allows to establish wing loading and power-to-weight ratio of the aircraft based on imposed punctual requirements. In Table 2.5 are depicted all SMP entries, from AIAA RFP, FAA FAR-23 and Team choices based on market analysis.

Adopting EM as propulsive sources brings an advantage: **available power does not depend on altitude**. This is evident in SMP as service ceiling requirement is far away from where it should be with a conventional power plant.

Most binding constraints are take-off distance, stall speed and rate of climb, as shown in Figure 2.4. Wing loading has been chosen to fulfill requirements and to be similar to values of *Cessna C-172* and *Piper PA-28*, in order to have comparable handling qualities. Power-to-weight ratio is chosen to observe continuous constraint but not the non-continuous one (i.e. take-off distance), for which non-continuous power can be employed.

Resulting design point enforces:

- **Wing loading** = 13.5 psf
- **Weight-to-Power ratio** = 19.5 lbs/hp (continuous) / 16.0 lbs/hp (non-continuous)

Non-continuous power is only $\simeq$ **22%** higher than continuous, thus **bearable for an EM operation of a few minutes duration**, as for take-off.

*initially supposed to be 2000 ft, later incremented to 4500 ft (see Section 2.3.5)

Constraint	Configuration	Imposed by	Parameters
Stall speed	LND	Team	45 kt
Take-off distance	TO	AIAA RFP	$<$ 1500 ft @ 5000 ft
Landing distance	LND	AIAA RFP	$<$ 1500 ft @ 5000 ft
Max cruising speed	Cruise	Team	@ 10 000 ft and 120 kt
Service ceiling	Cruise	AIAA RFP	@ 18 000 ft and +100 fpm
Rate of climb	Cruise	Team	@ 0 ft and +750 fpm
Climb gradient All EMs operative	Cruise	FAR-23	@ 0 ft and 8.3%
Climb gradient Balked landing	LND	FAR-23	@ 0 ft and 3.0%
Climb gradient 1/2 EMs inoperative	Cruise	FAR-23 alike	@ 5000 ft and 1.5%
Instantaneous turn	Cruise	Team	$n = 2.5$ and 90 kt

Tab. 2.5: Sizing matrix plot entries

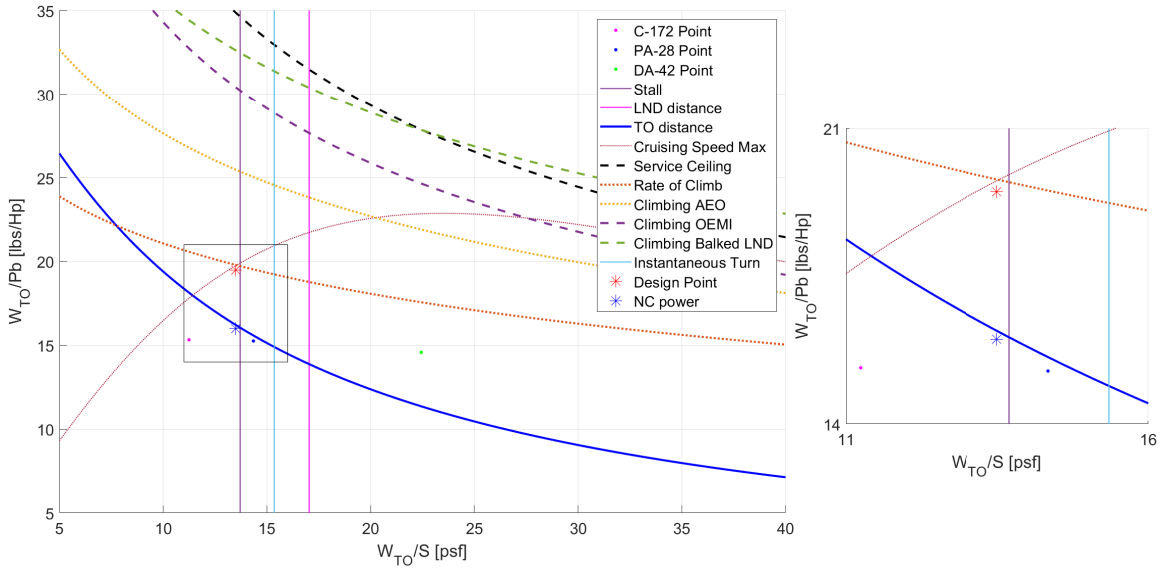

Fig. 2.4: Sizing matrix plot representation, with zoom of interest zone

2.3.3 Optimal approach

In accordance with [32], functional to be minimized is:

$$\mathcal{J} = \left(\frac{W_{ICE}}{W_{ICE,ref}}\right)^2 + \left(\frac{W_F}{W_{F,ref}}\right)^2 + \left(\frac{W_{EM}}{W_{EM,ref}}\right)^2 + \left(\frac{W_{bat}}{W_{bat,ref}}\right)^2 \tag{2.3}$$

The choice of this functional allows to **minimize take-off weight** and, subsequently, energy needed to complete every mission, production cost and operating cost. At denominator, $(\cdot)_{ref}$ indicates reference values (typical) for every partial weight, in order to normalize and give their relative importance. These are fixed values, but later modified to check robustness of solution.

At every iteration, the optimizer chooses values for every quantity and makes computation of $\mathcal{J}$, until it reaches a stationary point. At this level physics and flight-mechanics come into play imposing the following constraint for parameters selection:

1. Logarithmic regression $W_{TO} - W_a$: supposing that W_{TO} for the hybrid plane will be greater than W_{TO} of current aircraft, this has been implemented as bounds: $W_{TO} \geq W_{TO,regr}$ and $W_{TO} \leq 1.4 \cdot W_{TO,regr}$;
2. Total energy in BP at take-off: accounting for pure-electric taxi, take-off, electric climb and energy needed for turnaround at landing if PGS would not start, plus 10% reserve: $E_{bat} \geq 1.1 \cdot E_{req}$, where $E_{bat} = \frac{W_{bat} \cdot \mathbb{E}_{bat}}{g}$;
3. Max power drained from battery pack, with a safety factor: $\frac{W_{bat} \cdot \mathbb{P}_{bat}}{g} \geq 1.1 \cdot P_{req}$;
4. Power values from SMP and EMs regression: $W_{TO} = P_{EM} \cdot \left(\frac{W_{TO}}{P}\right)_{SMP}$;
5. Fuel needed to complete mission from ICE efficiency and fuel specific energy, with upper and lower bound: $W_F \leq \frac{E_{ICE} \cdot g}{\eta_{ICE} \cdot \mathbb{E}_F} \leq 1.2 \cdot W_F$;
6. Minimum power coming from ICE that matches 95% of power needed for hybrid climb: $P_{ICE} \geq 0.95 \cdot P_{req_{climb}}$.

This procedure has been repeated for every ICE regression made.

2.3.4 ICE choice and second-stage-optimizer

Optimizer output for piston diesel engines matches a point far from existing engines. Therefore, this kind of ICE has been excluded. In the case of turbine engines, the best-fitting ICE seemed

to be *Solar T62T2A1*. However, shaft power is far from regression line, resulting into a too low charging contribution. Moreover, high consumption, high noise and the necessity of an extensive re-training of maintenance technicians results in excluding this kind of engine, too.

Regarding gasoline reciprocating engines, **optimizer returns a point very close to *Rotax 915 iSc***. This has been employed into the second-stage of the optimizer, which takes a freezed PGS point and initial condition from first stage optimizer outputs. Then, it returns optimal values for the other quantities of interest, this time with a more refined flight mechanics model. Also cruising altitude and cruising speed are outputs of this more refined optimizer. Since all constraints result satisfied, these values have been considered for sensitivity analysis.

2.3.5 Sensitivity analysis and final outputs

Parameter	Constraint
C_{D_0}	< 0.025
K	≤ 0.06
η_{EM}	≥ 0.92
η_P	≥ 0.76

Tab. 2.6: Main parameters constraints

Sensitivity analysis has been conducted varying parameters one at a time and relaunching again optimization process. Most critical ones are depicted in Table 2.6. As a side effect, sensitivity analysis showed the best **transition altitude** from electric to hybrid climb for this mission is **4500 ft**. This altitude reduces fuel needed and working time of ICE, as limitation on BP comes from power needed.

Another verification was performed changing initial values and reference values for the optimizer to assess robustness of the solution. This is confirmed by negligible variations of output weights throughout all modifications.

The optimal solution is stable with respect to ranges of input parameters. Final results are reported in Table 2.7. Span value has been accepted as not too much dissimilar from common values for the considered aircraft segment, so needed hangar space will not be a problem. Also wing surface is not far from average, with wings for sure capable of providing enough volume for fuel, having a MAC whose length is **c=1.52 m**.

Parameter	Value
m_{PGS}	117.7 kg
m_{fuel}	119.4 kg
m_{EM}	30.3 kg
m_{bat}	60.1 kg
m_a	351.2 kg
m_{TO}	1038.7 kg
S	15.76 m^2
b	10.50 m
P_{EM}	117.2 hp
V_{cruise}	101 kt
h_{cruise}	9759 ft

Tab. 2.7: Optimizer outputs

3. Configuration selection

3.1 Propulsive configuration

Among solutions presented in Section 2.1.2, the Team chose the **"Switch Concept"**, which is basically a simulation of SE mode, because it is the most convenient as already mentioned.

An **even number of EM are placed symmetrically** with respect to longitudinal axis and SE or ME flight modes are obtained via software and hardware implementation. Electric motors on the left and right side spin in opposite direction. It must be avoided that a SE rated pilot or student pilot finds himself into an asymmetric thrust condition, which would be extremely dangerous.

Adopting just two motors would be sufficient for normal flying, but not in emergency. Configurations with 4, 6 or 8 EMs are taken into account, since increasing the number of electric motors would have benefit in safety. However, it increases complexity, cost and drag. Furthermore, there are no available motors on market to fit the 8 EMs configuration, consequently **6 EMs configuration** is chosen.

To forestall the event of asymmetric flight a specific system logic and redundancy of the electric motors management is developed, outlined in Figure 3.1. Battery packs and PGS are managed by two distinct **Energy and Propulsion Management System** (EPMS), collaborating and communicating each other and with the avionic suite. EPMS are responsible for feeding EMs and for the entire power and energetic management, charge or discharge of BPs, PGS management and 6 independent electric motor throttling regulations. One EPMS is responsible for 3 electric motors, **placed so that their equivalent moment is zero**, as described by Equation (3.1)

$$\begin{cases} \sum_{n=1}^{6} \mathcal{N}_G^{EM_n} = 0 \\ \mathcal{N}_G^{EM_1} = \mathcal{N}_G^{EM_4} + \mathcal{N}_G^{EM_5} \quad \wedge \quad \mathcal{N}_G^{EM_2} + \mathcal{N}_G^{EM_3} = \mathcal{N}_G^{EM_6} \end{cases} . \tag{3.1}$$

Even in case of failure of one EPMS, 50% of continuous power is still available and capable of granting symmetric flight. Moreover, by enforcing non-continuous power previous percentage can rise to 75%.

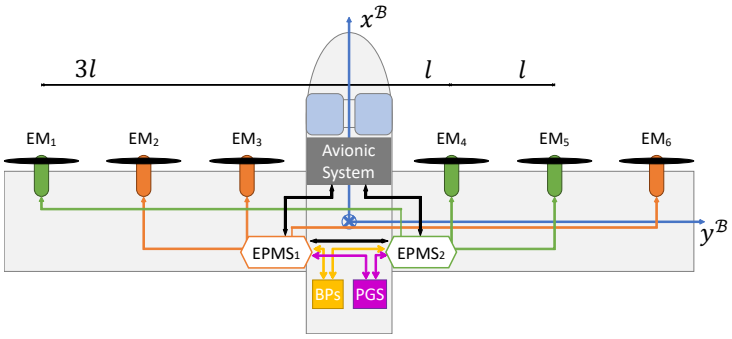

Fig. 3.1: Propulsive system architectural schematics

In this specific architecture, the two EPMS units are not in a redundant configuration, but **cooperant**. This strategy is lighter, simpler, cheaper and still represents a safe solution in case of one EPMS failure, as residual thrust is sufficient to satisfy climb prescriptions from FAR-23. EPMSs embed a small inertial unit with MEMS (Micro Electro-Mechanical Systems). An example of feedback control logic is presented in Figure 3.2. This logic can be implemented via a PID or LQR controller.

Propellers design takes advantage of electric propulsion being foldable. Thanks to foldable propellers system can **switch-off pairs of EMs** depending on power required at the moment. This leads to a drag reduction in cruise and to employ remaining EMs at highest efficiency. Motor controllers can simply impose to stop rotation for **blade closure**.

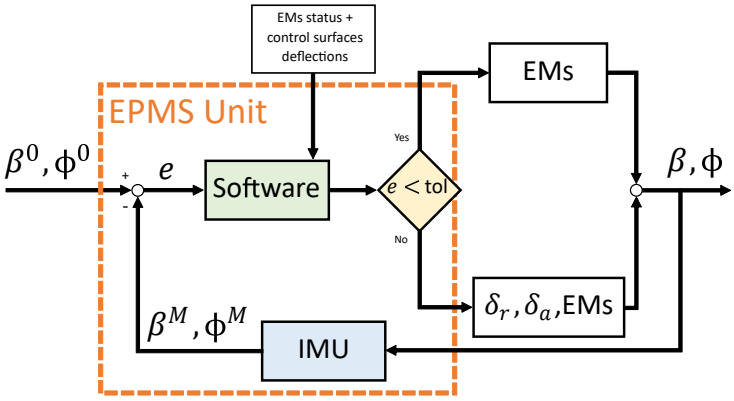

Fig. 3.2: EPMS unit feedback plant example

EPMSs are responsible for identification and management of failures. Potential malfunctions are:

- communication lost with avionic suite or other EPMS unit;
- one motor struck or malfunctioning, or a propeller broken, or electrical connection lost, identifiable comparing electric current normally needed with the actual one;
- battery pack malfunctioning or PGS failure

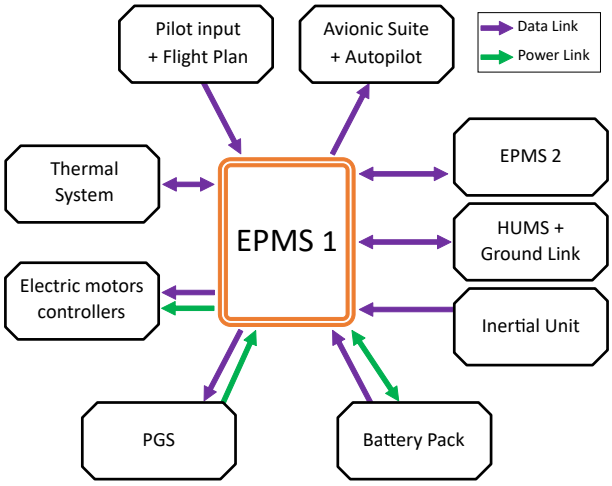

Fig. 3.3: EPMS unit connections

EPMSs must identify the situation, take the right corrective action and communicate it to the pilot. The units also include an Health and Usage Monitoring System (HUMS) for BPs, PGS, EMs and electrical systems, which records abnormal parameters values. This whole integrated system increases overall safety level. Chance of full power loss is really unlikely compared to conventional aircraft, especially SE ones, and must be the result of multiple failures. This aspect is a driver over certification restriction and hopefully could lead to a reduction of insurance premiums. EPMS schematic interconnection is outlined in Figure 3.3.

Employing the described system allows to produce just one aircraft, and **commonality requested between two designs by AIAA RFP is obviously** 100%. This entire concept has been in-depth studied, up to the point a **patent application has been registered for a concrete realization** [11].

Pilot interface

PIC must switch between SE or ME mode via MFD only on ground before starting operations. PFD must show selected mode all the time in a clear and unmistakable way. Moreover, pilot can choose the preferred energetic strategy for the mission, or leave the decision to EPMSs. PFD and MFD show fictitious parameters based on selected flight mode, for instance manifold pressure for one or two engines, one or two propellers RPM and so on.

Each propulsive side have its own thrust lever and they are normally joined together. Their position will not be directly related to electric motors RPMs, but to the power needed in percentage of total available. They will also account for non-continuous power adjustment.

An emergency "Panic Button" on-board can give authority to the system to exit from an incidental spin, acting motors with differentiated thrust.

During training, flight instructor will assist the student pilot formation via MFD. **Failures can be injected** so that the student response could be tested.

SE Mode

The main difference between SE and ME aircraft is that single-engine aircraft is not symmetric: β angle induced by propeller rotation must be corrected through aerodynamic forces asymmetry. Aircraft are usually designed to fly symmetrical in cruise configuration, while pilot must act on the rudder when at full power or in idle, due to different propeller spinning. This behavior is simulated by EPMSs acting differently on one of the outboard motors, for instance asking 95% of power instead of 100% when adding power. In descent EPMSs could close 5 propellers out of 6. Differential power ratios have to be tested in flight testing campaign. An example of working logic for SE configuration is in Figure 3.4.

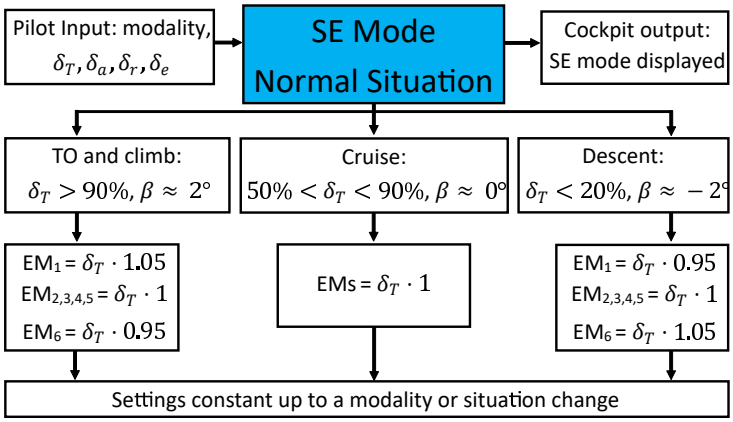

Fig. 3.4: Working logic for SE mode - Normal Situation

Gyroscopic effect due to propeller rotation of a single-engine airplane could be even simulated acting differently on the electric motors when maneuvering. Furthermore, normal reciprocating engine working mode can be simulated, introducing a loss of available power with increasing altitude, different power supply curve and irregularities.

To manage **Emergency Situation**, it is not admissible to fly in a **non-symmetric condition** with a single-engine rated PIC or SPIC. Let's examine the following potential threats:

- motor failure, propeller failure, bird-strike: these three situations share same output, namely thrust asymmetry. EPMSs will manage power given to singular motors to keep zero sideslip; if this is not enough, EPMSs will also command autopilot's rudder and ailerons actuator to prevent sideslip. This could also work for a minor structural damage resulting in an asymmetric drag;

- one EPMS failure: this only affects maximum power available, because as previously stated one thrust line can sustain symmetric flight;

- hardware or software EPMS malfunction: the single EPMS enters in a downgraded

working logic. Same thrust percentage is applied to each EMs under control by that unit. Alternatively, it is automatically switched off, leaving total control to the other unit.

For every situation, acoustic and graphical alerts will warn the pilot to assure situational awareness. A logic scheme for emergency situation in SE mode is outlined in Figure 3.5.

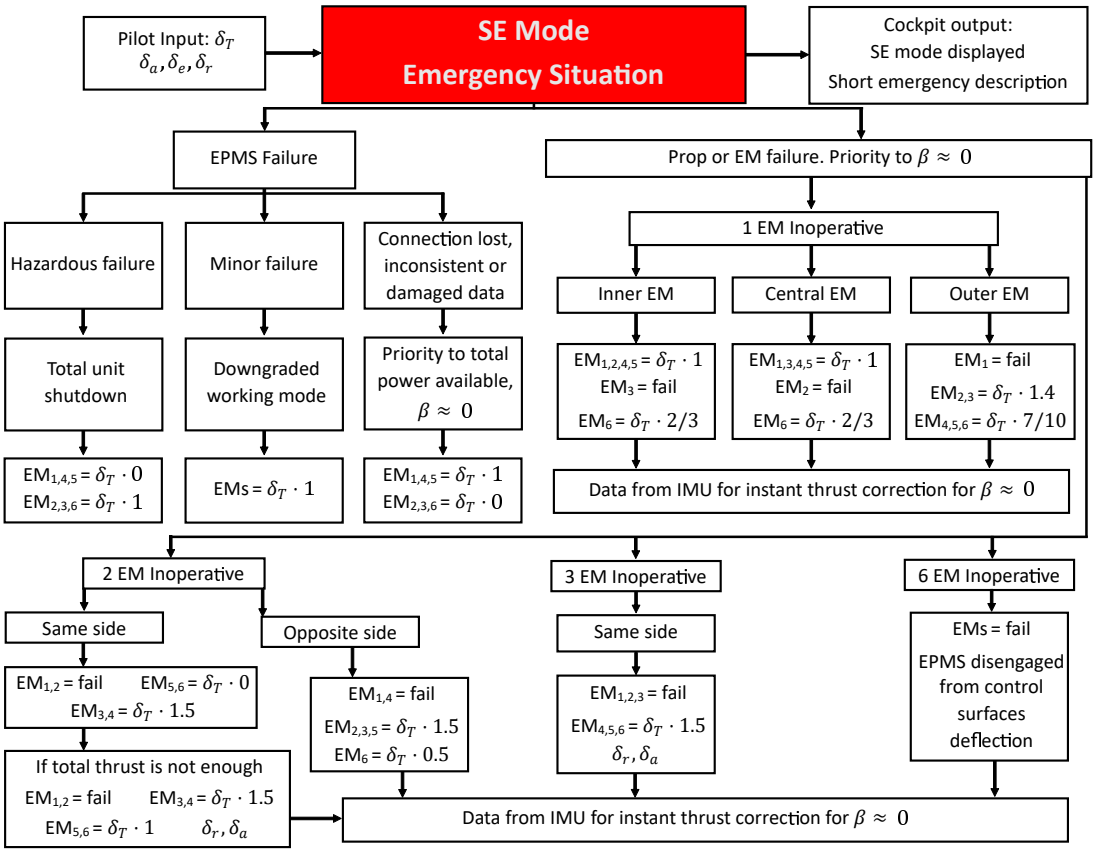

Fig. 3.5: Working logic for SE mode - Emergency Situation

ME Mode

Multi-engine configuration works in a much simpler fashion, as there is no need of simulating unwanted propulsive effect as for SE mode. Thrust levers can be unlocked and used independently, for training or other purposes. PIC has the complete authority on aircraft behavior.

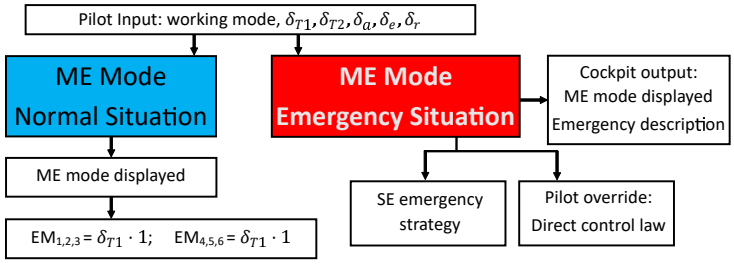

Fig. 3.6: Working logic for ME mode

The same strategy for SE emergency situation is adopted to reduce pilot workload, unless the pilot explicitly decides to bypass it.

Logic for both normal and emergency operations is explained by Figure 3.6.

Turbine simulation

It is also possible for both switch modes to simulate turbine engines behavior. This primary accounts for engine **spool-up time**, forcing student pilots to make high-RPM approach. Secondly, **virtual turbine engine parameters** should be displayed on PFD. This mode could also simulate speedbrakes with differential, but symmetrical, use of the electric motors.

Comfort enhancer

For every working configuration a comfort enhancement mode is available. This will employ EPMSs to suppress Dutch-Roll mode, provide automatic turn coordination and reduce noise and vibrations.

3.1.1 Motors arrangement

Electric motors are disposed symmetrically about aircraft longitudinal axis. Following configurations have been considered:

a) six EMs on wings in tractor or b) pushing configuration;

c) six EMs on wings in pushing configuration;

d) six EMs on wings, two pusher and four tractor or e) vice versa;

f) six EMs on wings, four on tips in pusher-tractor configuration and two at mid-wing;

g) mixed combinations with motors on wings, horizontal and vertical tail and fuselage appendix;

h) mixed configurations with four motors on wings or horizontal tail, one tractor in aircraft nose and one pusher in aircraft tail.

Configurations g) and h) have been excluded because of higher wiring and drag.
Six motors on wings is something close to distribute propulsion (DEP). DEP brings in advantages as wing blowing, with a consistent maximum lift coefficient increment, but also drag increment due to higher dynamic pressure and wake interference. *NASA X-57* exploits this to reduce wing chord, which besides increases wing loading. This is not compatible with a trainer aircraft, particularly in power-off situations. Added drag could be minimized maximizing EM spacing, reducing propellers diameter and putting two EMs in wingtips where half flow affects wings.

Adopting pusher motors would only marginally reduce wing blowing, but motors cooling and inclusion in wings is more difficult. Furthermore control surfaces positioning is not straightforward. Therefore, configuration b), c) and d) are rejected.
Configuration e) is interesting as it significantly reduces blowing, but it brings disadvantages: it requires a bigger rudder to contrast yawing moment with two motors inoperative on a tip. **Configuration a) has been eventually chosen**: initially, on each wing one motor was put in tip and the other two at $\frac{b}{6}$ and $\frac{b}{3}$ distance from centerline. However, this led to an extremely oversized vertical tail to contrast the 3 EMs inoperative situation on one side. To avoid such large vertical tail, **inboard motors are placed at 1.13 m** distance from centerline, while central and outboard are respectively at double and triple distances.

3.1.2 Pure-electric or hybrid-electric configuration

Aircraft is designed to work in pure-electric (PE) or hybrid-electric (HE) configuration thanks to **PGS unloading** possibility. This can be done fast and easily placing PGS in the nose and covering it with a simple and light fairing. PGS is attached to the firewall with only 4 bolts and it is only connected with electric and fuel systems.
Three different battery pack bays are planned:

1. Main BP bay, called **"Hybrid Bay"**: always present on-board and core of the hybrid configuration, but with a reduced capacity;

2. **"Passenger Bay"**: allows allocation of another battery pack on-board, regardless of the configuration. It is installed in place of rear passengers, whose seats must be removed. Hence their hook would be employed as BP bay's fixing points. Number of BPs stored in this bay should vary to cope with different CG and TOM. As this bay is inside the cabin, it must be placed under a self extinguishing fireproof cover;

3. **"Engine Bay"**: in place of PGS, it is used only for PE flight. Its size, weight and balance match those of PGS.

It is possible to fly the aircraft in PE mode loading all the three bays. HE mode can sustain up to 2 people on-board if "Passenger Bay" is fitted on-board.

3.2 Airframe configuration

Selection of most suitable configuration has been undertaken with particular focus on the fact that the aircraft is a trainer. This deeply restricted design freedom, according also to what emerged from market analysis concerning non-traditional configurations (see Section 1.4).

Decisions have been made exploiting ***analytic hierarchical process*** (AHP) [33]. The advantage of this decision support tool is that the final ranking is obtained on the basis of the pairwise relative evaluations of both the criteria and the alternatives provided by the user. Sensitivity analysis are easy to perform to validate the result.

3.2.1 Wing position

The alternatives considered were low, mid and high wing. The criteria adopted to select the most suitable wing configuration are reported in Table 3.1, as well as the partial and overall scores.

Criterion	Weight	High wing	Mid wing	Low wing
Lateral stability	3	**3**	2	1
Longitudinal stability	1	1	2	**3**
Stall characteristics	2	**3**	2	1
Maintenance ease	3	1	2	**3**
Costs	4	**3**	2	1
Drag penalties	4	1	2	**3**
Weight	4	**3**	1	2
Effect on view from cockpit	3	2	1	**3**
Aesthetics	1	2	**3**	**3**
Ergonomics	2	**3**	1	1
Overall score	-	0.4	0.27	0.3

Tab. 3.1: Wing position selective criteria and alternatives scores

High wing proved to be the best alternative and sensitivity studies provided a further confirmation.

3.2.2 Tail configuration

About 85% of flying aircraft exhibit an aft tail configuration, the 10% canard and the remaining 5% have an unconventional configuration. This trend is even more evident with reference to General Aviation. Then again market survey represents a potential acid test from the ideological point of view. Moreover, a configuration as similar as possible to the aircraft used after the training course is paramount for fast adaptation. Conversely, previous considerations led to discard *a priori* canard and unconventional configurations.

Within the aft tail configurations, several characteristics have been taken into consideration: low weight, low cost, simplicity, performance and stall characteristics. T-tail, cruciform, H-tail, V-tail, twin boom-mounted and (of course) traditional configurations were considered as suitable candidates. Nevertheless, even without AHP, there is no doubt **traditional tail** configuration is the most fit for the purpose, thus it has been selected.

3.2.3 Fuselage configuration

Main goals are to minimize cost, weight and wetted surface. The pressure tube fuselage was discarded *a priori* as it is ideal for a pressurized aircraft like a liner, but presents disadvantages for a GA aircraft. The tadpole configuration has a lower weight and wetted surface than the frustum-shaped fuselage, as opposed to the high cost and difficulty of design and production. Since this design considers a small aircraft with low weight, the advantages are not so convenient (compared to the disadvantages) to justify this choice. For these reasons, a **frustum-shaped fuselage** configuration was selected, also enforcing better compatibility with low cost metallic airframe.

4. Propulsion and systems

4.1 Electric motors

Selected propulsive configuration consists of 6 EMs mounted on wings, which must satisfy the requirements reported in Table 4.1. Remaining selective criteria encompass costs and reliability.

Parameter	Constraint
Mass	$\leq 5\,\text{kg}$
Continuous power	$\geq 14.6\,\text{kW}$
Non-continuous power	$\geq 125\%$
Efficiency	$\sim 94\%$

Tab. 4.1: EM requirements

Only **brushless motors** have been considered, as they are more powerful, lighter, more efficient and with less maintenance than brushed ones. The Team contacted several producers; most of them asserted products can be **customized** to guarantee optimized torque, power and RPM at same price as off-the-shelf ones. They even offer to optimize it to maximize compatibility with the chosen propeller, conducting a complete bench test campaign.

EM	Mass	Power	Peak	Efficiency	Dimensions	Retail price
MGM REX30	5.2 kg	15 kW	146%	97%	0.074 x 0.216 m	2366$
Alien P.S. 120100/S	3.9 kg	16 kW	156%	84%	0.120 x 0.216 m	614$
AstroFlight 4535	5.2 kg	15 kW	ND	96%	0.178 x 0.114 m	2490$
Neumotor 12060/10	4.5 kg	20 kW	170%	97%	0.072 x 0.139 m	1399$
Tmotor U15XL	4.4 kg	17 kW	136%	98%	0.086 x 0.151 m	1699$

Tab. 4.2: Candidate electric motors evaluated and their main parameters

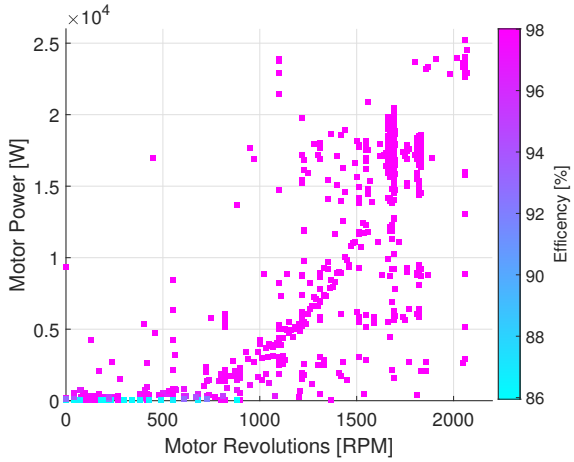

Fig. 4.1: *MGM Rex30* efficiency map

Maximum power is limited by power available from battery pack. EPMSs cover also this aspect in order to preserve BPs, which are anyway sized to fulfill power requirements.

MGM motor producer provided a complete test chart with real measured point for *Rex30*. Efficiency values of those trials are represented in Figure 4.1 as function of RPM and shaft power, highlighting how efficiency is high on a wide op-

erating range. Other components are **Electronic Speed Controllers** (ESC), assumed with a mass of 0.8 kg each and located as close as possible to each motor. Operating voltage is set to 400 V to reduce losses in wires.

After all previous considerations, reasonable parameters are assumed from existing EMs instead of choosing a ready product and customization trade-off is performed to best fit designed propeller. These parameters are reported in Table 4.3.

EM	Mass	Power	Peak	Efficiency	Dimensions	Cost
Custom	4.3 kg	15 kW	150%	96%	0.1 x 0.2 m	3957 $\$_{2025}$

Tab. 4.3: Electric motor selected

Only maintenance needed is lubrication and check of ball bearings, as long as EMs work in planned temperature and loading envelope.

4.2 Propellers

Propellers are sized in parallel with electric motors and wing blowing analysis. Blades can be folded not only in emergency, but also in every case a reduced amount of power is sufficient. In normal cruise, simulations show just 4 EMs in continuous power range are needed to maintain straight level flight. Propellers with folding design do not have significant drawbacks or efficiency losses and are way more simple, lighter and with less maintenance than variable pitch propeller normally required in a complex or ME aircraft for blades feathering. Hub is made of light aluminum, allows blades folding and includes an end-plate. When blades open they form a gap in fairing to let external air enters to cool electric motor.

Blade design process copes with a number of requirements:

- diameter must be minimized, to let blades fold on fairing, reduce tip speed under 200 m/s to limit noise produced, reduce percentage of wing blown to reduce increment of drag and reduce gyroscopic rigidity to preserve maneuverability;
- structural strength must be verified and certifiable;
- cruise efficiency must be optimal;

- thrust produced on ground must be enough to meet take-off run requirement at MTOM.

Software *JavaProp* has been used to design the propeller. The line-up followed in the design process starts from selection of diameter and cruise RPM at maximum continuous power to comply with previous requirements. Then, an optimizer selects best blade airfoils for highest propeller efficiency in cruise, number of blades and the AOA for each section. Concluding, *JavaProp* is used to validate results and build geometry of the propeller.

The preliminary trade-off studies highlighted that higher diameter means higher efficiency in cruise and thrust; eventually 0.75 m seemed to be the best compromise. *MH 116 9.8%* airfoil [58] resulted the one optimizing cruising efficiency at 5000 ft. Parameters are reported in Table 4.4, while side and frontal views of the blade are drawn in Figure 4.2.

Parameter	Value
Number of blades	5
Max TO RPM	4000
Diameter	0.75 m
Spinner diameter	0.10 m
Pitch	1.07 m

Tab. 4.4: Propeller main parameters

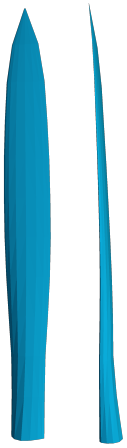

Fig. 4.2: Propeller blade

Blade root chord was at a later time increased to comply with structural requirement, obtaining a **cruising efficiency** of **81.9**%. Even if cruising efficiency is not at the top of diagram reported in Figure 4.3, this value is the highest in number among every other designed propeller.

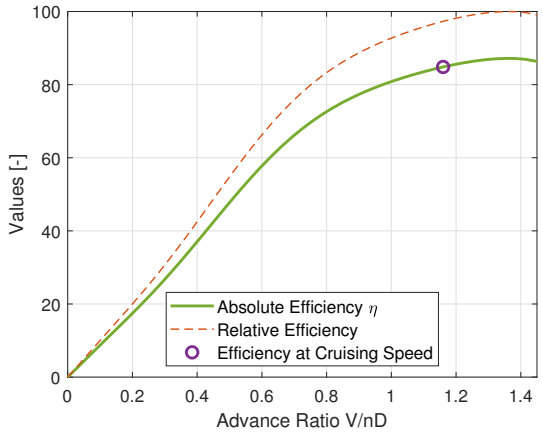

Fig. 4.3: Propeller efficiency plot

Propellers are located in correspondence of pilots' seats since new FAR-23 does not specify angular clearance from the cockpit. On the other hand, structural strength must be assured. Blades are made of **carbon fiber** and **epoxy resin** for best lightweight and strength [59].

In Figure 4.4 the results of Tresca stress analysis are collected. Blades are assumed to work at sea level and stresses developed at max RPM

and twice this value, an unreachable situation, are compared with limit carbon fiber strength.

Blade mass is estimated to be 0.357 kg and complete propeller assembly amounts to 2.2 kg.

In take-off regime, blades tip speed is around 150 m/s, well below 200 m/s needed for noise abatement. This value can rise up to 168 m/s in climb or normal cruise setting.

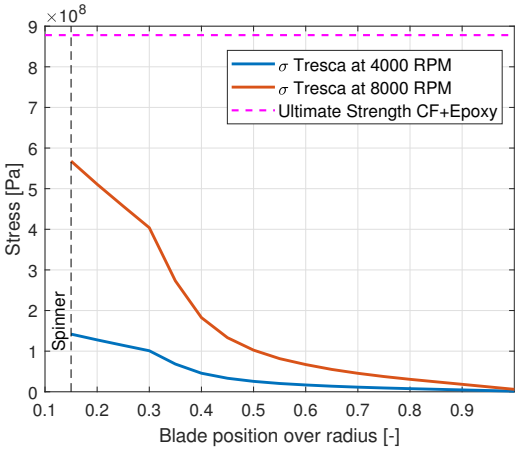

Fig. 4.4: Blade Tresca stress analysis

Reverse thrust

Although propellers are foldable, blades could be operated in opposite rotating direction as air-brakes. *JavaProp* confirmed that the adopted propeller could produce a reverse thrust, of magnitude equal to the 20% of nominal one. The centrifugal force must be enough to oppose this reverse thrust and drag, so that blades do not fold up.

A feasibility study has been carried out using estimated values of thrust given by *JavaProp* at slow flight speed. With an angular speed of 1500 RPM, force opposing to blade opening is 63 N and the opening angle is ~ 88 deg. Holding the same angular velocity and increasing the force up to 120 N, a very high value, the blade is still almost completely opened, with an angle of 86 deg. Opening angle remains acceptable as long as angular speed is higher than 1000 RPM.

4.3 Battery packs

The single BP unit is always the same for interchangeability and to minimize different items produced. The optimizer allocated 60.1 kg mass for "Hybrid Bay", which is split in three handy units for easy and fast substitution. A single BP unit has a mass of 20.04 kg. Table 4.5 collects bays parameters. Fairing volume is not critical at all for installation of "Engine Bay".

Every bay is structured in a **modular architecture**, embedding liquid cooling network and allowing BPs fast substitution [12], as already done by *Rolls-Royce* and *Pipistrel*. Thus, exhausted batteries may be swapped with fully charged ones on ground, reducing off-times. "Passenger bay" can store up to 12 BPs, depending on weight and balance of current loading configuration. In full electric mode maximum energy storable on-board is thus 96 793 kW h, thanks to 21 BPs.

Bay name	BP units	Mass	Energy stored	Power available	Volume
"Hybrid"	3	60.12 kg	13 828 kW h	96 793 kW	30.7 dm^3
"Engine"	6	120.24 kg	27 655 kW h	193 586 kW	61.5 dm^3
"Passenger"	12	240.5 kg	55 310 kW h	387 173 kW	122.9 dm^3

Tab. 4.5: Battery Pack bays

4.4 Power generation system

Engine chosen for PGS is *Rotax 915 iSc* (Figure 4.5*). It is a certified as flat-four turbocharged engine with electronic fuel injection and ignition, capable of nominal 135 hp continuous output and 141 hp non-continuous from 0-FL up to 15 000 ft, with a service ceiling of 23 000 ft and a dry mass of 84.6 kg. Declared TBO is 1200 h, an alarming low value. Unitary price is 45 700 USD at 2020.

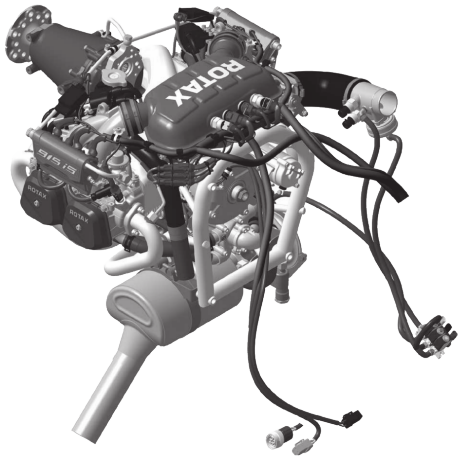

Fig. 4.5: *Rotax 915 iSc drawing*

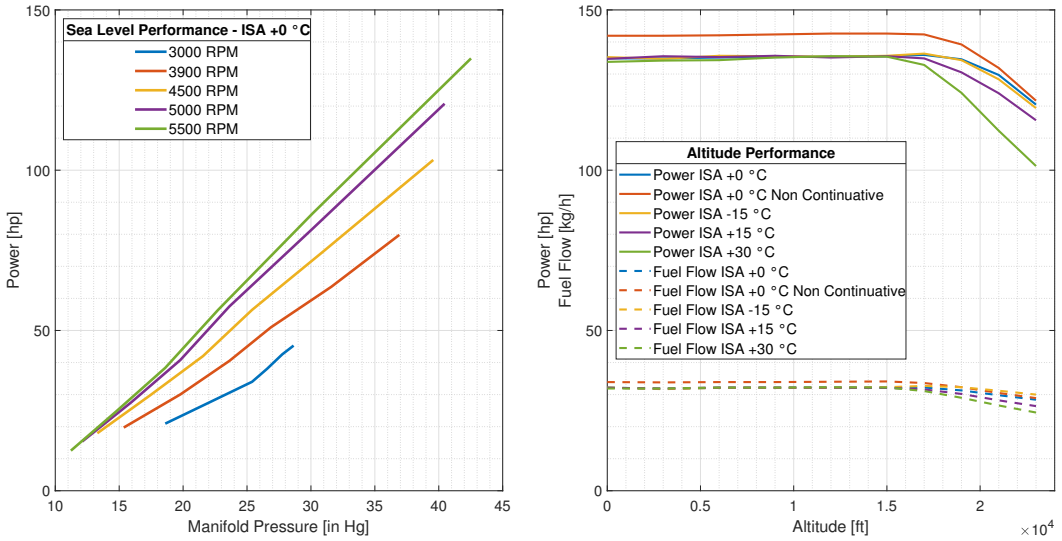

Fig. 4.6: *Rotax 915 iSc* performance map

*taken from service manual

4.4.1 Engine modification to PGS

Adapting ICE to become a PGS requires coupling with an electric generator. According to regression in Section 2.2.2, electric generator to match engine performance has a mass of 33.1 kg and 95% efficiency.

Engine can be modified removing gearbox, hydraulic propeller pitch governor, electric starter motor and freewheel, which is normally subjected to wear. Even the engine alternator can be lightened. The result is a significant weight reduction (just the gearbox itself has a mass of 10 kg) along with removal of components subject to maintenance. As for this mass reduction, **117.7 kg** so far considered can be assumed as PGS wet mass with electric rectifier, engine management and related systems.

Throttle valve will be actuated by an electrical auto-throttle system controlled by EPMS units and include a manual emergency kill-switch. ICE is set to always works in continuous power range, using non-continuous power only in emergency situation.

Engine comes with a pre-installed cylinder air conveyor. Settling an appropriate air intake, engine installation is allowed in any aircraft location without overheating risks. Existing gearbox fitting holes are employed and electric generator shaft is spliced directly on that of the engine. This leads to a linkage without losses or plays, allowing generator to be used as a starter.

4.4.2 Technical issues and maintenance

The Team was able to arrange a meeting with italian *Rotax* dealer to speak with a *Rotax* engineer, Matteo Comencini, about technical aspects.

Turning the engine on and off multiple times in a flight, also at high altitude, do not affects maintenance as confirmed by Comencini. Main concerns about adopting this engine was the short TBO, which would have an important impact on costs. When a *Rotax* engine reaches its TBO, it is usually the entirely substituted, requiring 42 030 USD at 2020.

> *"The 915 is a new engine, and in Rotax is common practice to start with low TBO interval and raise it gradually. It is in Rotax's plan to extend it well beyond* 2000 h*; several engines already passed* 4000 h *without any problem."*
>
> - Matteo Comencini, *Luciano Sorlini SPA*

Another important topic concerns engine warm-up time, as imposing an electric transition altitude several minutes are needed for the engine to reach operating temperature. As a consequence, feasibility of such strategy would not be guaranteed.

> *"Once oil temperature reaches* 50 °C *engine can be operated at full power without any risk or consequence. The 915 reaches fast that temperature with respect to other Rotax engines thanks to the turbocharger and alternator in oil bath, but if you need to be quicker you can consider some expedients."*
>
> - Matteo Comencini, *Luciano Sorlini SPA*

To quicken engine warm-up, electrical resistors are drowned inside oil tank and crankcase. Preheating engine oil to 70 °C on ground, or on initial climb, allows engine start-up just a few seconds before needed. Oil contained into circuit is maximum 3.0 l and energy required to heat it is less than 0.1 kW h, negligible with respect to energy in battery pack. Weight added by resistors is negligible and their reliability is high.

All *Rotax* engines are designed to run on *MOGAS*, but can also run on *AVGAS 100LL*. If this latter is used at least 30% of the time, the interval between servicing must be halved. Eng. Comencini made a maintenance estimation, accounting for spare parts, consumables and labor costs, summoned in Table 4.6, with prices at 2020 and intervals for *MOGAS*. Maximum oil consumption is 0.06 l/h, hence refilling cost is negligible when compared to total maintenance.

25 hours and multiples	**200 hours and multiples**	**600 hours and multiples**
390$	555$	1670$

Tab. 4.6: Ordinary maintenance intervals and costs

4.4.3 Engine procurement

All the above modifications are positively approved by Eng. Comencini. The engine must be certified again after modifications, but it should be anyway coupled with the electric generator. Manufacturer in case of a big prolonged order could produce a customized version of the engine, maybe also releasing an optimized ignition map, and certifying it. Following previous

considerations, TBO interval for future calculations is set to **3000 h**.

4.4.4 Engine pollutants analysis

Main pollutants emitted are: **carbon dioxide**, responsible for greenhouse effect, **carbon monoxide**, **hydrocarbons** and **nitrogen oxides**. These three latters are extremely toxic for the Planet and human beings. It can be said that HC, CO and NO_x are considered as local pollutants and their concentrations must be reduced on the ground or near airports and inhabited centers; instead, CO_2 and NO_x are considered as global pollutants and they must be reduced in any flight phase.

Since *Rotax 915iSc* is a recent engine, no data have been found to carry out an analysis of pollutants emissions. Experimental data for *Rotax 914* [34], pretty similar to the *915*, have been taken into account, as reported in Table 4.7.

Flight phase	$\dot{m}_f$ [kg/s]	EI_{HC} [g/kg]	EI_{CO} [g/kg]	EI_{NO_X} [g/kg]
Take-off	0.0072	14.8	1013	5
Climb	0.0056	12.2	660	15
Cruise	0.0042	16.5	805	8
Approach	0.0029	16.0	776	12
Taxi	0.0018	38.6	944	5

Tab. 4.7: *Rotax 914* experimental pollutant production data

EI_i is the emission factor of the $i-$th component in grams for each kilogram of fuel. No value was assigned to carbon dioxide, therefore it has been calculated starting from fuel carbon content, whose value is 3067 g/kg (assuming *AVGAS 100 LL*), as done in [5].

Pollutants are compared in terms of their ***social cost***, namely the cost to citizens due to aircraft operations, depending on the chemical composition and its dangerousness. Coefficients listed in Table 4.8 are obtained projecting to 2025 the results collected at Taiwan Taoyuan International Airport [35].

Pollutant	**Social cost** [$\$_{2025}$/kg]
CO_2	0.0510
CO	0.1311
HC	6.5094
NO_X	14.6350

Tab. 4.8: Pollutants social cost

4.5 Avionics and electrical system

The Team decided to design a **Technically Advanced Aircraft** (TAA). Choice is driven to avoid "complex aircraft" FAA requirement for training and because a digital and advanced avionic suit with integrated autopilot is mandatory to work and interact with EPMS units.

Despite having assumed power required by avionic system in Section 2.2.5 as the one of *Garmin G1000*, its evolution ***Garmin G2000*** is chosen. This is an high-end and expansive product, allowing great integration with many different plants, sensors, gauges and propulsion systems. Pilot interface is made of PFD and MFD, plus one central pedestal selection screen and a backup display. The avionic suite embeds a complete automatic flight guidance and control system, with *GSA-81* autopilot servos and *GSA-82* trim servos. Suite is IFR certified and embeds all state-of-the-art possibilities of avionics, including touch-screen technology and synthetic view.

Pitot probe could be located in the fairing, but to let this latter be easily removed, it is located on one wingtip.

4.6 Fuel system

Aircraft is equipped with two fuel tanks, installed as close as possible to mean CG location. They are sized to accomplish ferry range requirement, resulting in 225 l total usable fuel. Since fuel falls thanks to gravity to PGS there is no needs for fuel pump. It include only an in-cabin tank selector, filling caps, overfilling and air inlet intake. Fuel tanks are adopted instead of an integral system because the first ones are safer in case of crash landing.

4.7 Cooling and anti-ice system

Electric motors and ESCs receive a great amount of fresh air from the outside, hence this is sufficient for their cooling. A typical air intake is designed to cool ICE and electric generator starting from engine operating manual specifications.

Battery temperature management is extremely critical. They generate a great amount of heat which must be dissipated in order to preserve efficiency, life and being safely operated. Battery pack surface must never exceed 55 °C. On the other hand, batteries suffer low temperature operations and work well only above 15 °C [36]. At the same time, also EPMS units must be

kept at working temperature.

Not to require air intakes of great total area and drag, a **liquid cooling system** embedded in BP bays and EPMSs is exploited [37]. This leads to increments in empty weight and power requested, but the system is thought to perform all its functions:

- cool and maintain the right temperature value for battery packs and EPMSs;
- transfer generated heat to wings, where this is used as thermal anti-ice system;
- warm-up batteries in case of cold weather start.

First of all, it is necessary to understand what "flying in known icing conditions" means: super-cooled droplets are most common up to $-20\,°C$, while below this temperature icing risk is almost null [38]. As a consequence, anti-ice system is sized for full protection up to **-25 °C**.

This complete system is based on a parallel architecture in which the liquid enters in different ducts at the same time. The circuit is split in two for safety reason; left and right wings are interested by liquid of separated plants, actuated by two independent pumps. Cooling fluid is **water mixed with anti-ice liquid**. Battery pack is modeled as a block at constant temperature. First, the mass flow needed to keep batteries at the desired temperature is calculated. Then, hot fluid is divided between the two wings, each composed of two lines: the main line, in charge for the anti-ice effect, and the return line. The first one is close to the leading edge, modeled as an heat exchanger composed by eleven flat pipes posed in direct contact with the wing. They are approximated as rectangles 5.3 cm wide and 1 mm thick. The overall length of each pipe is 4.58 m. The wing plant pipes distribution and main line pipes layout are reported in Figure 4.7.

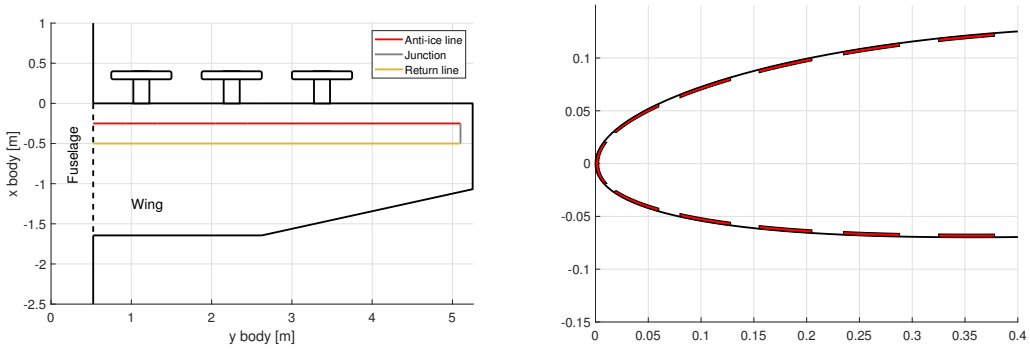

(a) Lines placement in wing plant **(b)** Main line pipes positioning in wing section

Fig. 4.7: Thermal system lines scheme

A system with valves controls number of pipes interested by the flow, function of the external temperature. To guarantee anti-ice effectiveness, nose pipe is always working. Return line is simple: only one cylindrical pipe of 1.5 cm in diameter.

To estimate convective coefficients, empirical correlations have been used, taking into account that only one face of the pipes is in contact, through the wing, with the external airstream. Given the geometry, illustrated plant and water in pipes have a total mass of 13 kg. Simulation computes mass flow rate needed to cool battery packs in present working condition. Highest computed mass flow rate in the plant is 0.64 kg/s, corresponding to an outside temperature of 40 °C at zero altitude and 50 kt. In this extreme condition, batteries are kept at 52 °C. Then, even with a small increase in altitude thermal performance rise significantly, allowing to maintain a lower battery temperature. For what concern anti-ice effectiveness, even with an air temperature lower than working limit temperature in the wing tip is still higher than 20 °C.

Two working simulations for the thermal system are depicted in Figure 4.8.

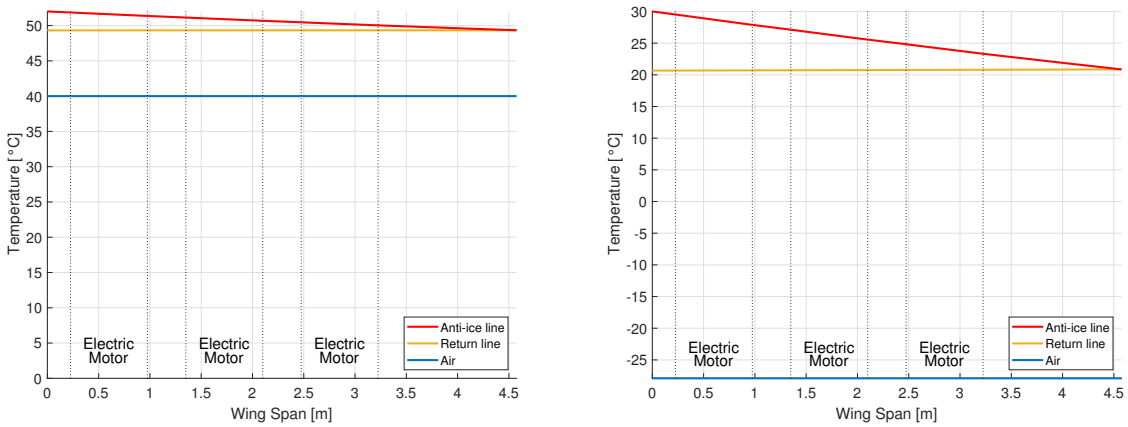

(a) $T_0 = 40\,°C$ at zero altitude, 11 pipes working **(b)** $T_0 = -18\,°C$, $h = 5000\,ft$, 2 pipes working

Fig. 4.8: Thermal system simulations

In case of a cold weather start a resistors group placed at BP bays inlet heats liquid up to 30 °C employing external ground power. Subsequently, current flowing in or out batteries will auto-maintain temperature to a reasonable high value. Resistors guarantees also support to anti-ice when systems do not provide enough heat, as in emergency. Calculated pipes and water total mass is later increased by 30% to account for uncertainties, connections and valves.

To determine pumps weight a regression based on real pumps data has been performed. Result is a singular pump mass of 1.95 kg for a pump with a maximum flow rate of 0.75 kg/s to

account for uncertainties. Pumps must win a pressure difference of 10.1 PSI made by pressure losses in pipes and connections, plus height differences in a max load factor scenario. This maximum pressure difference is well below the maximum operative value of investigated pumps. Water pumps consumption is always considered in aircraft performance determination, as BPs always need to be cooled.

Liquid anti-ice system only interest wings, while for propellers, tail, windshield, static and Pitot probes an electric cyclic anti-ice system [39] is enforced for simplicity. As total surface shielded by this system is 1.38 m^2, total power required is 5 kW and added mass considering graphite foils of thickness 0.5 mm [60] is estimated to be 0.69 kg for film and 0.35 kg for wiring. Lastly, aircraft is equipped with surface illumination lights with split prisms on either side that illuminate both wing and horizontal stabilizer in low-light conditions.

4.8 Environmental control system

Aircraft is **not pressurized**, leading to a lighter and simpler design with less power required and less onboard systems, maintenance and structural issues. The aircraft is equipped with a simple **air system with portable oxygen tanks** placed in baggage compartment, pipes and four masks connections in cabin. Added weight is small, as typical aluminum oxygen tank with pressure gauge and regulating valve have a filled mass of 5.2 kg for serving four people [61]. Since the tank can be removed, total mass for in-cabin pipes and connection is estimated to be 1 kg.

Cabin heating is obtained with heat generated by PGS or "Engine bay" batteries, while cooling is left to external air. An air conditioning system is offered as optional item at procurement or later. For instance, electrically driven *Kelly Aerospace Thermacool* allows environmental control for 56 lbs added and 1260 W peak power or 644 W continuous [62].

4.9 Anti-bird-strike system

This aircraft in terminal operation flies electric, so this problem intensifies due to lower noise. Therefore, an anti-bird-strike system is included. There are several patents for such systems, but the chosen one is based on transponder Mode-S technology [13], already installed on-board. System exploits transponder antenna to radiate an electromagnetic wave in front of aircraft: such radiation should scare birds in front of it.

5. Aerodynamics

5.1 Wing airfoil selection

In order to avoid leading edge stall, provide enough space for fuel and limit wing weight, only airfoils with $t/c \geq 0.12$ were taken into consideration, even if this way drag is probably penalized with respect to thinner airfoils. The following *NACA* airfoils have been compared: *2412, 2415, 4412, 4415, 63212, 63215, 63A415, 64A215, 65415*. Other airfoils considered were *NASA GA-W1*, *Roncz*, *WORTMANN FX 63-137* and *Selig 1223*.

Software *XFLR5* has been adopted to extract aerodynamics data related to isolated airfoils. The analysis has been carried out considering cruise condition, at which $Re = 5 \times 10^6$ and $M = 0.16$. *XFLR5* provides as output pressure distributions and hence the values of C_l, C_d, C_m for a selection of AOAs.

Both quantitative and qualitative criteria were taken into consideration to draft airfoils. Prior selection has been performed to assure gradual stall characteristics, since of primary importance for a trainer aircraft. Ranking was then performed using AHP, comparing:

1. $C_{l_{max}}$: high to minimize V_{stall}
2. l/d: high for better aerodynamic efficiency
3. α_{stall}: high to postpone stall
4. $C_d(C_{l_{max}})$: low to have better performances at take-off
5. $C_{d_{min}}$: low to maximize range
6. $|C_{m_{cruise}}|$: low to reduce trim drag and torsional moment
7. Airfoil geometry (influencing costs and realization complexity)

Two airfoils best suited requirements: *NACA 2412* and *NACA 63212*. Sensitivity analysis confirmed robustness of the ranking to changes in relative importance between criteria: in 16 cases out of 21 experiments the best ranked airfoil (*NACA 2412*) did not change.

Data related to best ranked airfoils were compared with available experimental data in order to validate results. Among the experimental data collected in [40], tests performed at

$Re = 3 \times 10^6$ and $Re = 6 \times 10^6$ were compared with *XFLR5* results performed at $Re = 5 \times 10^6$, showing good match for both selected airfoils in terms of lift curve and polar (Figures 5.1, 5.2).

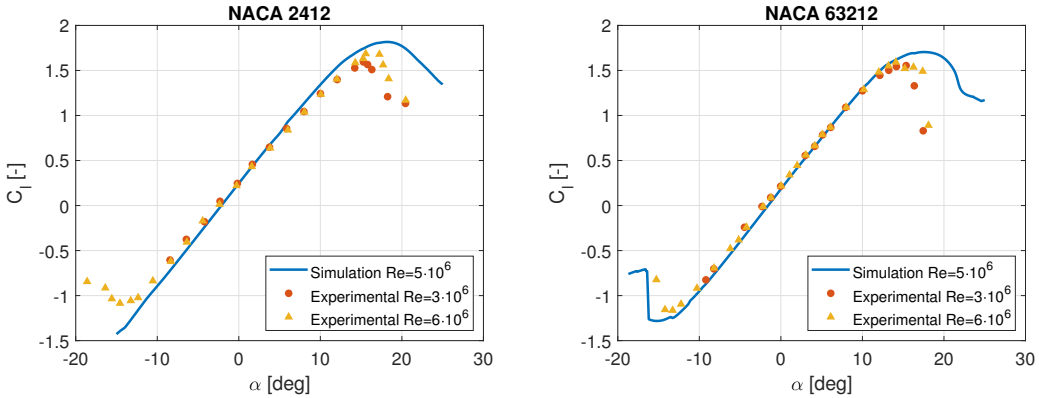

Fig. 5.1: Simulation and experimental lift curves for *NACA 2412* and *NACA 63212*

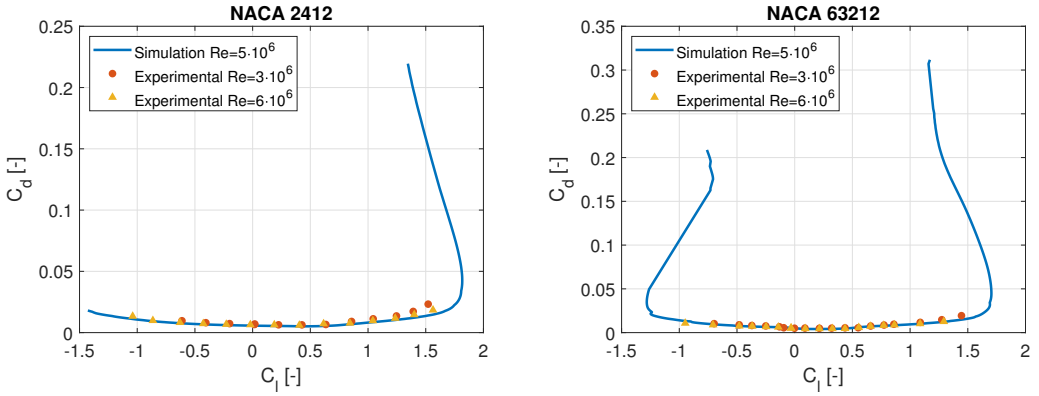

Fig. 5.2: Simulation and experimental polars for *NACA 2412* and *NACA 63212*

A further set of experimental data available in [40] is at "standard roughness", meaning carborundum grains were applied to the surface of wind-tunnel models at the leading edge, to simulate something between manufacturing irregularities and accumulation of ice or mud.

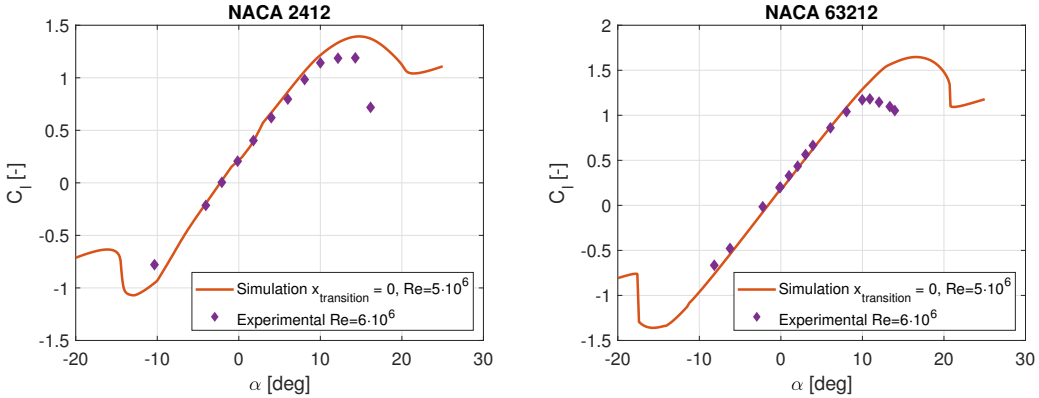

Fig. 5.3: Lift curves at standard roughness

This time corresponding *XFLR5* simulation enforced transition point at the leading edge of the airfoil. Lift curves comparison is reported in Figure 5.3. What emerges is that *XFLR5* is not capable of matching experimental data in case of "standard roughness" for *NACA 63212*. Results confirm expectations, as *NACA 2412* being a four-digit airfoil appears to be less sensitive to surface smoothness than *NACA 63212*.
As a conclusion, ***NACA 2412*** has been selected as the wing airfoil. This should not upset the reader, as this airfoil is adopted by many GA aircraft.

5.2 Wing shape

The selection of the shape of the wing has been carried out comparing different planforms in terms of behavior at stall and cruise. Candidates were rectangular, fully tapered and semi-tapered wings. For the latter, both taper and twist start at half semi-span, namely $k_{taper} = 0.5$.

Aspect ratio and taper ratio are assumed to be $\boldsymbol{AR = 7}$ and $\boldsymbol{\lambda = 0.65}$, as reported in Section 2.2.6. A range of values from 0 deg to -4 deg has been experimented for twist angle, whose effect is to provide a better lift distribution and to postpone stall at the tip. Sweep angle has been instead kept equal to zero for all the planforms studied. It has been added on the wing ultimately selected, obtaining negligible improvements that do not justify related increase in costs. Similarly, dihedral angle is set to zero, as high wing configuration assures sufficient lateral stability.

XFLR5 served to determine lift distribution along the span varying AOA. The approach undertaken to assess stall passes through computation of lift coefficient stall values at each span-wise station, so that they can be compared with lift distribution obtained as result of simulation. First of all, according to experimental data at $Re = 3 \times 10^6$, $C_{l_{max}} = 1.65$. This value is varied linearly along the span according to local Reynolds number, function of local chord. As soon as one station exceeds stall value for a given angle of attack, this is eventually wing α_{stall}.

The result chased is that flow detachment undergoing on the wing perturbs horizontal tail flow-field, providing the pilot a direct feedback through commands. This does not happen for fully tapered and rectangular wing, in which stall arises far from the root and too close to the fuselage, respectively.

The best stall characteristics are achieved by **twisted semi-tapered wing**. In fact, twist

angle moves stall location towards the root and postpones stall at higher angle of attack. Twist angle provides also a better lift distribution along the span, which translates into lower induced drag and bending moment. These aspects are paramount in cruise and simulations at cruise conditions showed optimal twist angle is $\mathbf{-4\,deg}$. Furthermore, k_{taper} have been varied to optimize its effect. Results showed marginal gains are achievable considering $k_{taper} = 0.4$. Nevertheless, stall locations are no more in the designed range, meaning baseline value $\boldsymbol{k_{taper} = 0.5}$ is the best.

It is possible to report lift distribution along the span at different AOA for the selected wing (Figure 5.4). Eventually stall arises at $\alpha = 18\,\text{deg}$ at locations among which the closest to the tip is at $y/(b/2) = 0.32$.

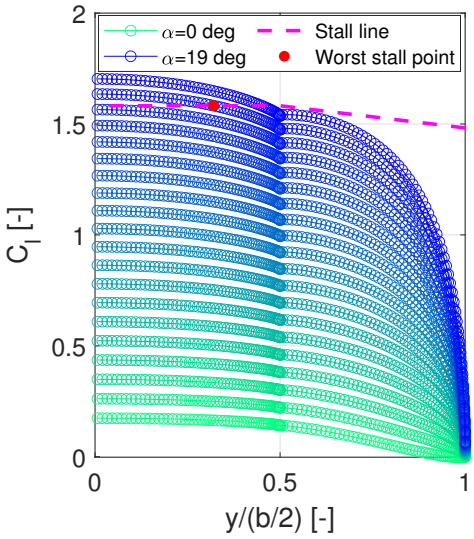

Fig. 5.4: Lift distribution along the span for selected wing at cruise airspeed

Wing root incidence is set at **3.6 deg**. This value minimizes drag in cruise, accounting for wing blowing with 4 electric motors working. It also leads to a positive angle of attack in take-off run, which allows aircraft to be airborne without a strong rotation.

At process ended, **upturned booster wingtips** have been added, preferred to round, square and Hoerner for simplicity, flying qualities and negligible change in total drag.

5.2.1 Effect of wing blowing

To better understand the effect of wing blowing on total lift and drag a semi-empirical model has been implemented, calculating increment in C_L and C_D from reference values [41]. In Figure 5.5 are depicted the effects on cruise of 4 EMs working (not accounting for mutual interference

in driven flow) against the same configuration with no propeller blowing on wings.

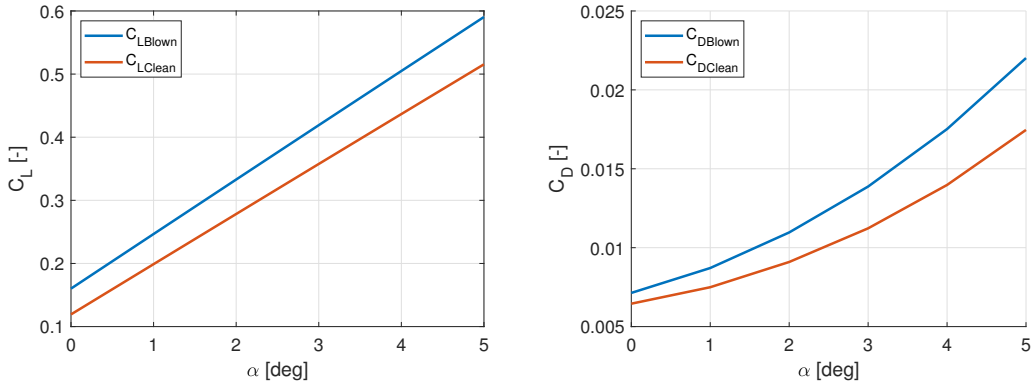

Fig. 5.5: Lift and drag coefficients in cruise with 0 or 4 EMs blowing

Results show how big is the increment achieved in lift, resulting in even shorter take-off run and generally better low speed power-on handling qualities, whereas drag increase due to lift increment is minimal. An angle of attack reduction comes as side effect. For instance, $C_L = 0.4$ at $\alpha = 3.5\,\text{deg}$ corresponds to $C_D = 0.0126$, while with 4 EMs blowing for the same C_L, $\alpha = 2.5\,\text{deg}$ and so $C_D = 0.0130$, therefore added drag in cruise configuration can be neglected.

5.3 High lift devices

Lift enhancement is achieved through installation of **plain flaps**. More complexity of other TE devices such as slotted flaps as well as use LE devices seems not justified in the design.

Parametric studies have been conducted to optimize performance of airfoil with flaps. A first choice was performed upon angle of deflection for landing configuration. The aim in this case is to increase both $C_{l_{max}}$ and $C_d(C_{l_{max}})$ without reducing too much stall AOA.

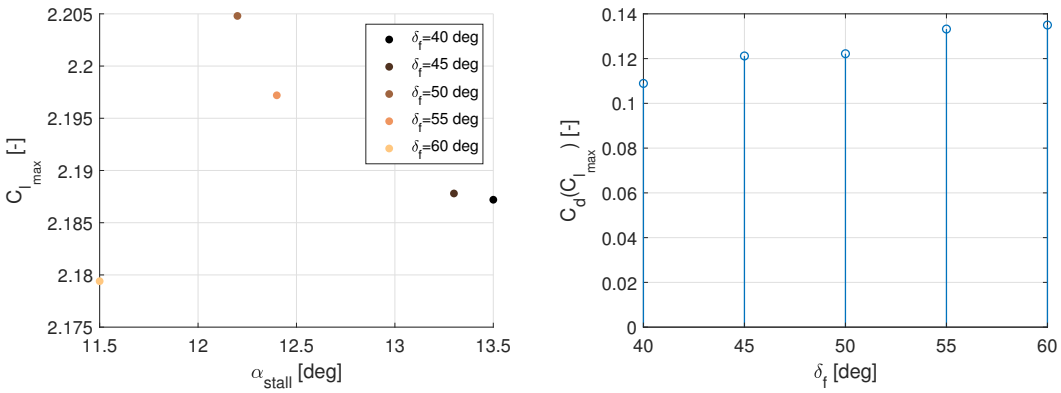

Fig. 5.6: Effect of angle of deflection on stall and drag

Angles in the range 40 deg ÷ 60 deg were considered. Since lift and drag increases for angles above 40 deg is limited, with instead an high penalization on stall AOA, low limit value of the range studied is adopted as landing flap deflection.

Next step of analysis consisted of variation of flap chord percentage (c_f/c). Although it is reported by *NACA* documentation that optimal value is $c_f/c = 0.25$, values of 0.20 and 0.15 were evaluated as well, with results reported in Figure 5.7.

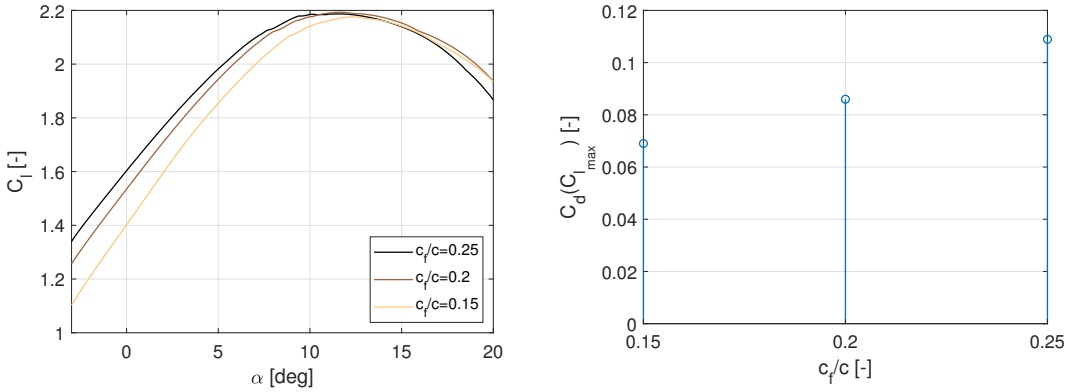

Fig. 5.7: Effect of flap chord percentage on lift and drag

The trade-off value $\boldsymbol{c_f/c = 0.20}$ is eventually the one adopted.

Flaps are installed in the rectangular sector of the wing, with the exception of the inner region in correspondence of the fuselage. At first try it had been tried to replicate the analysis performed through *XFLR5* to the flapped wing, in order to quantify $C_{L_{max}}^{LND}$ and $C_{L_{max}}^{TO}$. Eventually the software could not reach convergence. It was eventually chosen a numerical lifting-line method based on Prandtl's model [42] enforcing a fully three-dimensional vortex lifting law. This method has been translated into a numerical code, called *PNL*. Results of 2D airfoil are exploited with this code for the determination of C_l distribution along the span and $C_L - \alpha$ for clean wing and wing with flaps set to 10 deg, 20 deg and 40 deg. See Section 5.4 for results.

5.4 Aerodynamic verification and final results

All preliminary results were obtained through the software *XFLR5*: it uses a Vortex Lattice Method (VLM) with ring vortexes on a simplified geometry. This method belongs to the class of so-called "low-fidelity" methods. These are inexpensive, under-powered methods, with limited accuracy and low computational load. For these reasons, several simulations with CFD methods

("high-fidelity") have been made in order to verify the accuracy of the results. *OpenFOAM* was used for numerical solving.

First step is to generate a **mesh** in *OpenFOAM* to simulate a 2D airfoil in wind tunnel [63].

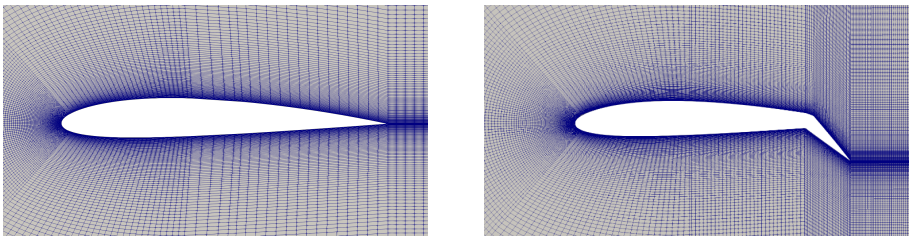

Fig. 5.8: Meshes used for CFD analysis, clean and flapped airfoil

Turbulence model chosen is the *k-ω SST* (k-omega Shear Stress Transport), which includes two additional equations to represent convection and diffusion phenomena of turbulent energy. In order to estimate the initial turbulence values, input required are free stream speed, reference length, kinematic viscosity and turbulence intensity, derived following [64]. To solve the continuity and proximity equations*, the *simpleFoam* solver has been used for clean airfoil. A steady method has been chosen to reduce the computational load and since excellent accuracy results are provided, thanks to the fact there are not important airflow separations. On the other hand, steady solver *pimpleFoam* had to be used in *pisoFoam* mode for flapped airfoil, in order for pressure-momentum coupling to be stable enough to produce a non-diverging solution.

Simulation have been carried out on an airfoil with unitary chord at different angles of attack, from 0 deg to 17 deg. Flow fields at $\alpha = 14$ deg are presented in Figure 5.9.

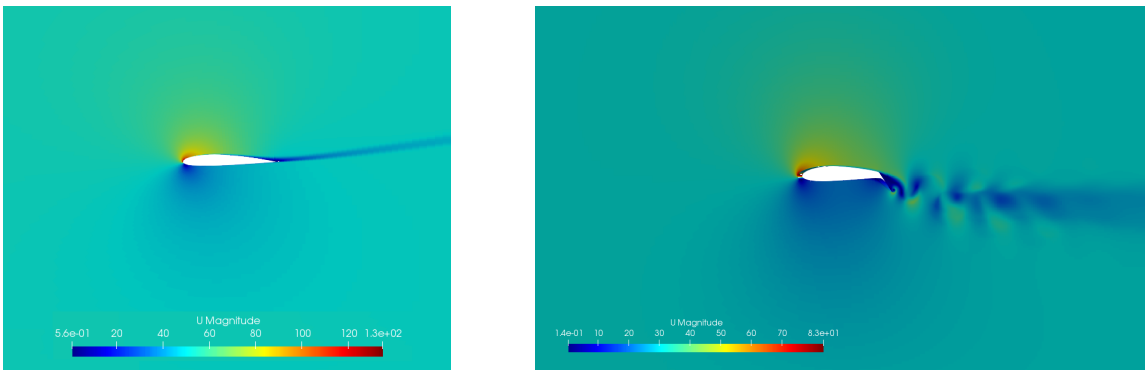

(a) Clean airfoil **(b)** Flapped airfoil

Fig. 5.9: Representation of post-processing at $\alpha = 14$ deg

Results have been obtained enforcing 2D data computed through OpenFOAM into *PNL*.

*coming from simplifications of Navier-Stokes equations

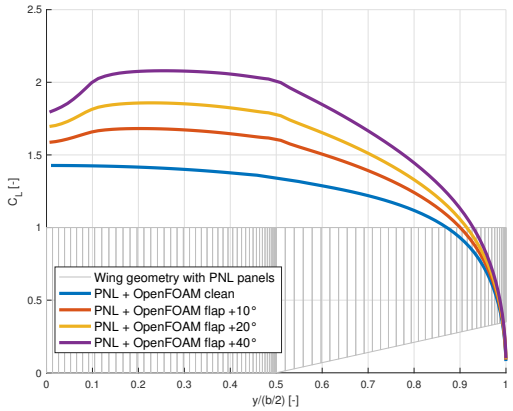

Fig. 5.10: Max lift distributions

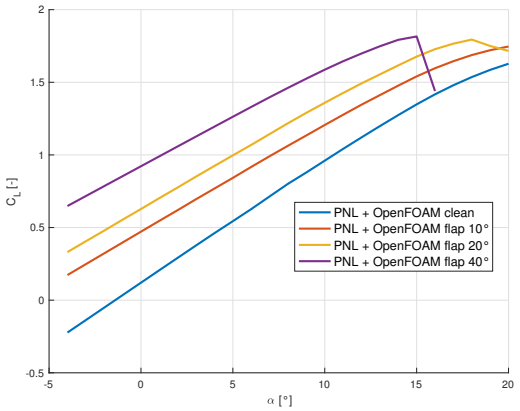

Fig. 5.11: $C_L - \alpha$ curves

Final aerodynamic parameters are reported in Table 5.1. Parameter F is defined as "power index", namely $F := \frac{(C_L)^{3/2}}{C_D}$, and $G := \frac{(C_L)^{1/2}}{C_D}$. Complete aircraft polar in clean configuration is depicted in Figure 5.12.

$\boldsymbol{C^C_{D_0}}$	0.0213	$\boldsymbol{\alpha_0}$	$-1.556\,\text{deg}$	$\boldsymbol{K^C}$	0.0542
$\boldsymbol{C^{TO}_{D_0}}$	0.0363	$\boldsymbol{C_{L_\alpha}}$	$4.383\,\text{rad}^{-1}$	$\boldsymbol{K^{TO}}$	0.0576
$\boldsymbol{C^{LND}_{D_0}}$	0.0863	$\boldsymbol{C^C_{L_{max}}}$	1.623	$\boldsymbol{K^{LND}}$	0.0615
$\boldsymbol{(L/D)_{max}}$	14.71	$\boldsymbol{C^{\delta_f=10\,\text{deg}}_{L_{max}}}$	1.763	$\boldsymbol{\alpha((L/D)_{max})}$	$6.39\,\text{deg}$
$\boldsymbol{F_{max}}$	13.28	$\boldsymbol{C^{TO}_{L_{max}}}$	1.789	$\boldsymbol{\alpha(F_{max})}$	$12.43\,\text{deg}$
$\boldsymbol{G_{max}}$	21.17	$\boldsymbol{C^{LND}_{L_{max}}}$	1.833	$\boldsymbol{\alpha(G_{max})}$	$3.00\,\text{deg}$

Tab. 5.1: Final aerodynamic parameters

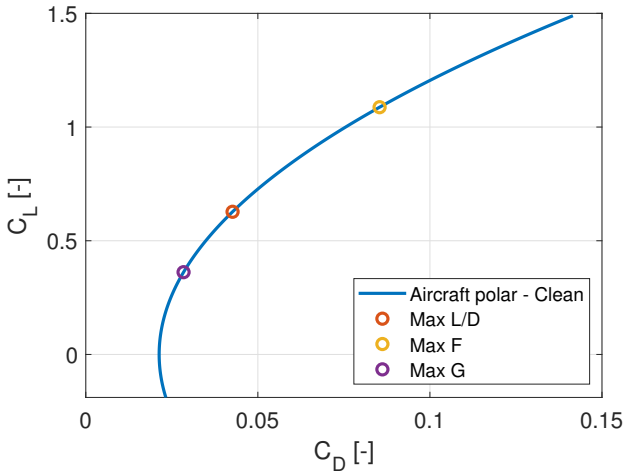

Fig. 5.12: Aircraft $C_D - C_L$ polar plot in clean, un-blown configuration

5.5 Ailerons

Ailerons chord percentage is $c_a/c = 0.2$ as for flaps. Geometrical quantities related to ailerons are b_1 and b_2, respectively the inward and outward spanwise locations of ailerons. In order to maximize ailerons effectiveness their centerline should be located in correspondence of maximum section moment coefficient, namely $\Delta C_{\mathcal{L}} = C_l y$, which averagely occurs at $0.8\frac{b}{2}$ for operative AOAs. Following this prescription it comes with no surprise to set $b_1 = 0.55\frac{b}{2}$ and $b_2 = 0.95\frac{b}{2}$. According to [6], aileron authority derivative is:

$$C_{\mathcal{L}_{\delta_a}} = \frac{2C_{L_\alpha}\tau}{Sb}\int_{b_1}^{b_2} c(y)y \ \mathrm{d}y = 0.2344 \tag{5.1}$$

Roll damping coefficient, namely a measure of the induced moment resisting roll is:

$$C_{\mathcal{L}_p} = -\frac{4C_{L_\alpha}}{Sb^2}\int_0^{\frac{b}{2}} c(y)y^2 \ \mathrm{d}y = -0.6534 \tag{5.2}$$

Starting from equilibrium of rotations of the aileron it is possible to derive the following relations for steady-state helix angle and derived roll rate:

$$\left(\frac{pb}{2V}\right) = -\frac{C_{\mathcal{L}_{\delta_a}}}{C_{\mathcal{L}_p}}\delta_a \implies p = -\frac{C_{\mathcal{L}_{\delta_a}}}{C_{\mathcal{L}_p}}\delta_a\frac{2V}{b} \equiv KV\delta_a \tag{5.3}$$

Besides computation of roll induced by aileron deflection it is necessary to verify the pilot can withstand hinge moment and then perform the maneuver through commands. Limit hinge moment sustainable by the pilot depends on maximum force applied to command, in case of wheel command prescribed by regulations to be $F_{max} = 50\,\mathrm{lbs}$. Besides, control line kinematics introduces a constant of proportionality, namely gearing ratio G_a, so that $F_{max} = G_a M_{h_{max}}$.

Furthermore, hinge moment can be expressed as $M_h = \frac{1}{2}\rho V^2 S_a c_a C_h$. Values for hinge moment derivatives are estimated following the procedure reported in [31], which eventually returns $C_{h_\alpha} = -0.0585\,\mathrm{rad}^{-1}$ and $C_{h_{\delta_a}} = -0.4108\,\mathrm{rad}^{-1}$.

Enforcing (5.3), it can be demonstrated **limit value for roll rate** is proportional to the inverse of velocity:

$$p_{limit} = -\frac{F_{max}}{G_a\rho S_a c_a(C_{h_{\delta_a}}\frac{1}{K} + C_{h_\alpha}y_a)}\frac{1}{V} \tag{5.4}$$

where $y_a = \frac{b_1+b_2}{2}$.

By plotting p_{limit} along with fan-shaped set of curves for different angles of aileron deflection it is possible to graphically visualize region of roll control capability for the pilot. By defining limit lower and upper values for flight speed and desired roll rate a "control box" is visualized.

The case reported in Figure 5.13 is obtained assuming as gearing ratio $G_a = 0.5\,\text{rad/ft}$, in accordance with the value of *Cessna 172* [1]. Control authority is optimal, since maximum deflection line (for which $\delta_a := \frac{1}{2}(|\delta_{a_{UP}}| + |\delta_{a_{DOWN}}|) = 25\,\text{deg}$) is close to the diagonal of the rectangular and its intersection with limit curve is in the middle of roll rate range.

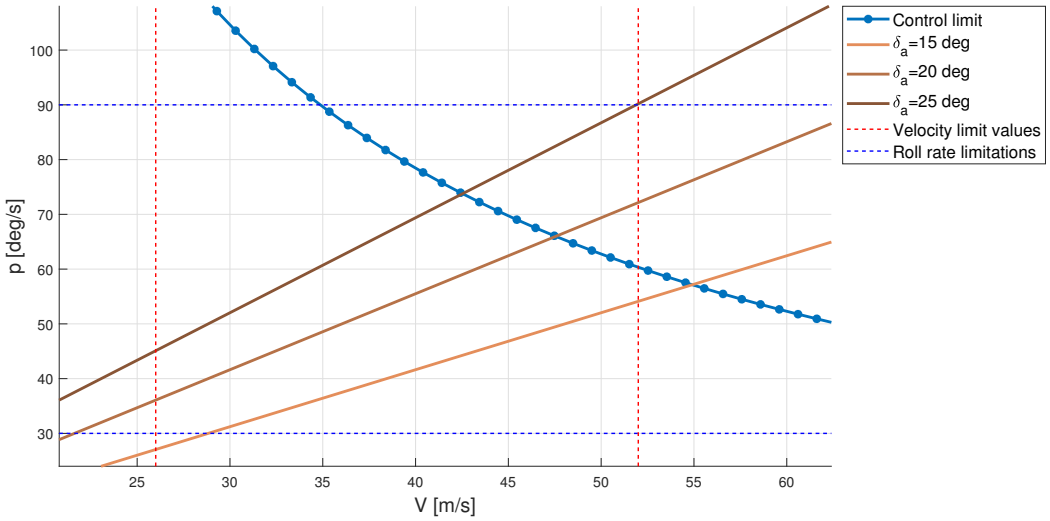

Fig. 5.13: Roll control box

5.6 Tail design

Aircraft tail design is conducted in parallel with propellers design, motors positioning, fuselage, undercarriage and internal weight arrangement with an iterative process. Hangar doors size played a role [65]. A normal surface is adopted to achieve normal flight controllability and handling, as expected from a trainer and to satisfy all requirements for the novel design.
Vertical tail sizing led to distribute motors closer to the fuselage rather than in tip. Indeed, initial motors positioning resulted in the configuration depicted in Figure 5.14, discarded as anyone could expect.

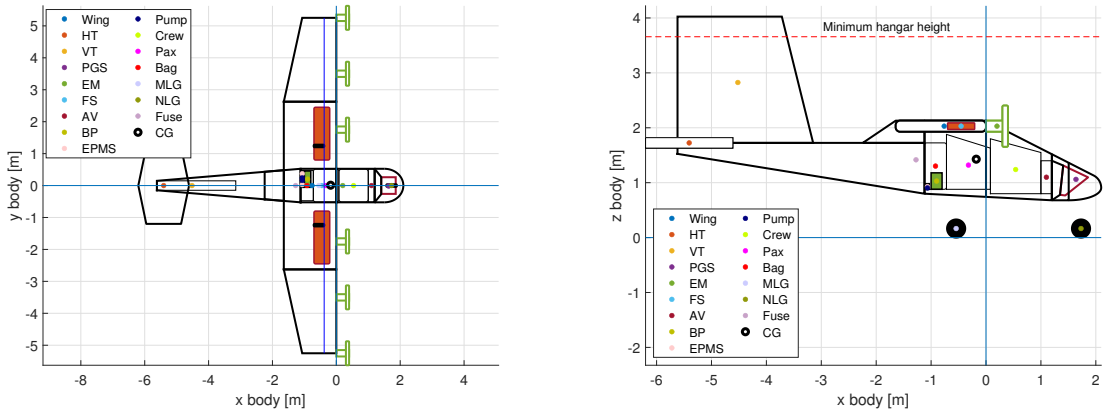

Fig. 5.14: Initial configuration with motors in tip

Second configuration, with close motors, is reported in Figure 5.15.

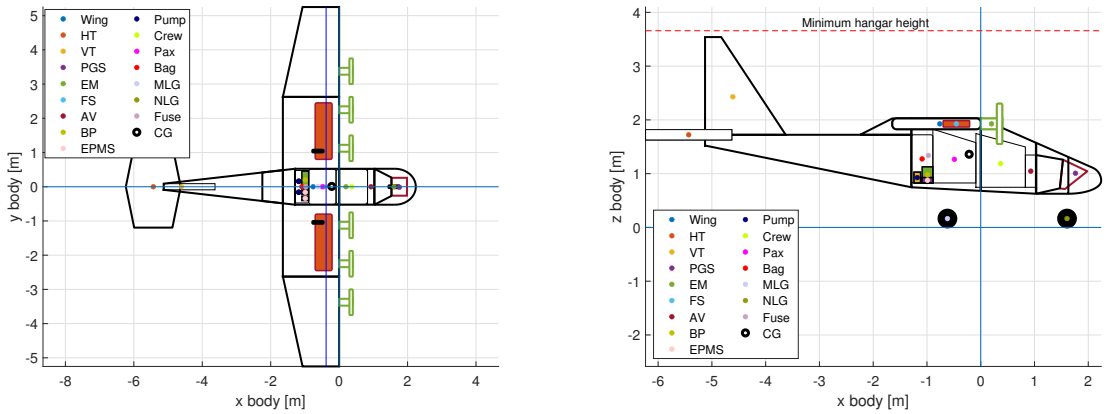

Fig. 5.15: Final configuration with close motors

These simple sketches have been employed to check consistence in all aircraft dimensions and sizes, landing gear sizing and preliminary CG determination. CGs for every sub-components are depicted in Figure together with total mean CG.

For both horizontal and vertical surfaces first design step is airfoil selection, carried out with an AHP approach as done for the wing. After this procedure, an optimizer is developed to find best parameter for vertical and horizontal surfaces altogether. Lastly, rudder and elevator surfaces are designed to meet requirements. For all calculation velocity of minimum control with 3 EMs inoperative on same side is set to $V_{MC3} = 45\,\text{kt}$, while $V_{MC} = 31\,\text{kt}$, well under $V_{S0} = 45\,\text{kt}$. Ground controllability is taken for granted thanks to the steering nose wheel.

5.6.1 Horizontal and vertical surfaces

Horizontal tail airfoil choice considers α_{stall}, $C_{d_{min}}$, C_{l_α} and $\overline{C}_m$: winner airfoil is ***NACA 63012***. For vertical tail drivers are $C_{l_{max}}$, α_{stall} and $C_{d_{min}}$. This time winner airfoil is ***NACA 0012***.

Optimal procedure constraints are negative $C_{\mathcal{M}_\alpha}$ and capability of vertical tail to contrast 3 EMs inoperative on the same side and spinning capability. Spin exiting is ensured placing at least half vertical surface in front of the horizontal one. Parameters to be minimized are total tail length, tail downforce, span of vertical tail and total wetted surface. At process completed, all results are reported in Table 5.2.

To conclude, values of stability and control derivatives are presented in Table 5.4. Both $C_{\mathcal{M}_\alpha}$ and $C_{\mathcal{M}_q}$ are negative, assessing longitudinally stable.

V_{ht}	AR_{ht}	λ_{ht}	l_{ht}	S_{ht}	b_{ht}	i_{ht}	c_{ht}^{root}	c_{ht}^{tip}
0.66	1.74	0.696	4.82 m	3.28 m	2.39 m	2.1 deg	1.60 m	1.12 m
α_{ht}^{cruise}	V_{vt}	c_{vt}^{root}	c_{vt}^{tip}	λ_{vt}	l_{vt}	AR_{vt}	b_{vt}	S_{vt}
−2.2 deg	0.04	1.5 m	0.3 m	0.2	4.07 m	2.02	1.817 m	1.636 m

Tab. 5.2: Final tail parameters

5.6.2 Elevator

For the selected values of span and chord, elevator must be able to exert a sufficient moment to rotate the aircraft at take-off speed and to trim it inside the whole envelope, for every CG setting, altitude, speed, configuration and weight without stalling the horizontal surface. Elevator span is 100%, its chord is 40% of tail MAC and maximum deflection is ±25 deg.

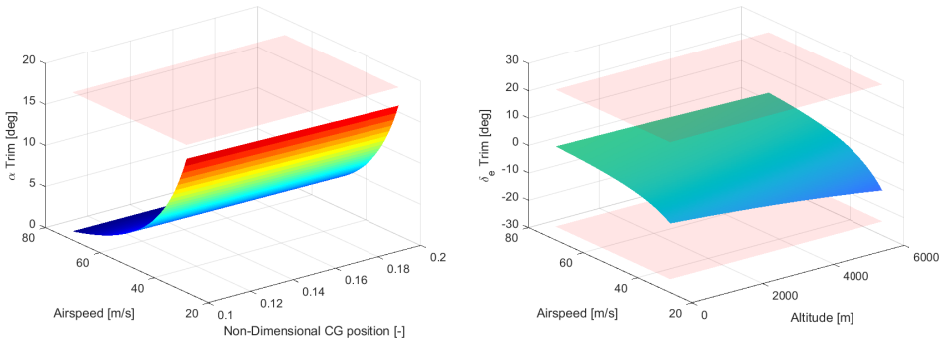

(a) AOA vs. Airspeed & ξ_{CG} **(b)** δ_e vs. Airspeed & Altitude

Fig. 5.16: Angle of attack α and elevator deflection δ_e for trim in clean configuration

Airworthiness requirements state that the stick force gradient $\frac{\mathrm{d}F_s}{\mathrm{d}V}$ must be positive and greater than a certain minimum value at trim. A minimum value suggested is 1 lb/kn (or 8.72 N s/m) [7]. At the same time the value of the force applied to elevator control should not exceed prescribed values (stick force positive in case of push). In particular, for prolonged application, stick force should be something below 44.5 N.

Following the procedure reported in [7] it is possible to write stick force as the combination of a constant term and a term linear with the square of the speed. As a consequence, stick force gradient is just linear with the speed. Without a trim tab stick force is well beyond limit values and stick force gradient is too low. In order to relieve the pilot and make control more intuitive, **trim tab** is thus to be included. Trim tab is installed on the right half of the elevator. The contribution to roll moment is negligible. Trim tab chord length is 40% of elevator.

Elevator hinge moment derivative with respect to trim tab deflection also depends on trim tab span. Eventually a span length of 60% was chosen, representing the best compromise in terms of size of the tab and deflection angle, thus reducing drag penalty.

In order to provide the pilot with sufficient level of control sensitivity, gearing ratio should be $G_e = 7.5\,\mathrm{rad/m}$, a value slightly higher than the ones reported in [1].

To conclude, assuming stick force is trimmed by tab deflection as previously determined, schematic variation of the stick force with velocity is represented in Figure 5.17.

Quantity	**Value**
C_{h_α}	$-0.0135\,\mathrm{rad}^{-1}$
$C_{h_{\delta_e}}$	$-0.2007\,\mathrm{rad}^{-1}$
$C_{h_{\delta_t}}$	$-0.1996\,\mathrm{rad}^{-1}$
$\delta_{t_{trim}}$	$\sim 5\,\mathrm{deg}$
G_e	$7.5\,\mathrm{rad/m}$
$\frac{\mathrm{d}F_s}{\mathrm{d}V}\Big\vert_{trim}$	$8.9\,\mathrm{N\,s/m}$

Tab. 5.3: Elevator and trim tab control

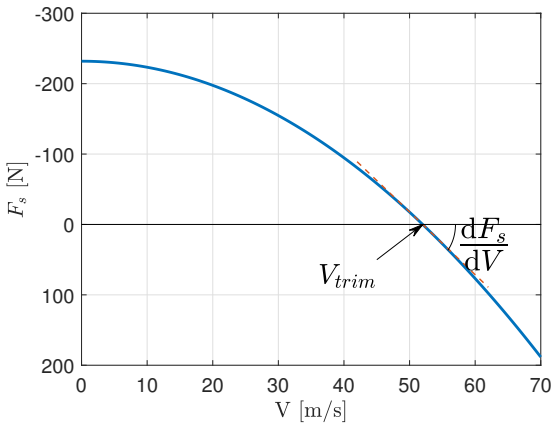

Fig. 5.17: Stick force variation with velocity

5.6.3 Rudder

Rudder design is conducted to contrast 3 EMs inoperative on same side, spin recovery capability and crosswind landing criteria, assuring stall does not occur. Rudder span is 98% of vertical tail, chord is 42% and maximum deflection is ± 30 deg.

3 EMs inoperative: the tightest constraint, satisfied with $\delta_r = 29.2$ deg at V_{MC3}. It is verified the **rudder pedal force** required in this condition is compatible with limitations from regulations, which impose a maximum value of 667.5 N [43]. Assuming a gearing ratio $G_r = 1.68$ rad/ft [1], pedal force to be applied is 340 N, so within limits.

Crosswind: hardest parameter to determine is fuselage side-wash $\frac{d\sigma}{d\beta}$ [44], while others are fuselage lateral pressure center and lateral stability and control derivatives. Given that vertical surface is large, for an approach speed of 58 kt a crosswind speed of even $V_{\perp W}^{max} = 42$ kt is allowed (an extremely high value compared to most GA aircraft), with $\delta_r = 26$ deg rudder deflection and $\sigma = 14$ deg crab-angle;

Spin: highly conservative values have been assumed [45], namely a vertical descent with an absolute velocity $V_{spin} = 42$ kt, a rotational speed of 200 deg /s and an angle of attack $\alpha_{spin} = 40$ deg; then, inertia moments are given by *NeoCASS* (Section 6). Applying full rudder deflection spin exiting occurs after 3.3 s and 326 deg of rotation after command input, corresponding to 151 ft lost, without necessity of differential setting of motors.

A further condition in which rudder is deflected is when operating in SE mode. In particular, climb could represent a condition in which rudder pedal force is required for a prolonged time. Anyway it has been verified required force does not exceed value for prolonged application, namely 20 lbs. Thus, **no** device is explicitly prescribed at this stage of design to relieve pilot workload. In conclusion, main stability and control derivatives are reported in Table 5.4.

$C_{\mathcal{M}_\alpha}$	$C_{\mathcal{M}_q}$	$C_{\mathcal{M}_{\delta_e}}$	$C_{L_{\delta_e}}$	$C_{D_{\delta_e}}$	C_{h_β}
$-1.24\,\text{rad}^{-1}$	$-13.4\,\text{rad}^{-1}$	$-1.1\,\text{rad}^{-1}$	$0.35\,\text{rad}^{-1}$	$0.0023\,\text{rad}^{-1}$	$-0.0737\,\text{rad}^{-1}$
$C_{\mathcal{N}_{\delta_r}}$	$C_{\mathcal{N}_\beta}$	$C_{Y_{\delta_r}}$	C_{Y_β}	$C_{\mathcal{L}_{\delta_r}}$	$C_{h_{\delta_r}}$
$-0.073\,\text{rad}^{-1}$	$0.1\,\text{rad}^{-1}$	$0.188\,\text{rad}^{-1}$	$-0.472\,\text{rad}^{-1}$	$-0.0728\,\text{rad}^{-1}$	$-0.2418\,\text{rad}^{-1}$

Tab. 5.4: Stability and control derivatives

6. Airframe structure

6.1 Structural model

Politecnico di Milano developed a tool called *NeoCASS*, whose idea is not only to provide a realistic estimation of structural weights, but also to enforce structural and aeroelastic analysis at conceptual design levels. First feature of the software is a coarse estimation of the weights and inertia of the aircraft based on empirical regressions from geometry and non-structural masses. These parameters can be set directly through the CAD module embodied in the suite, called *ACBuilder*.

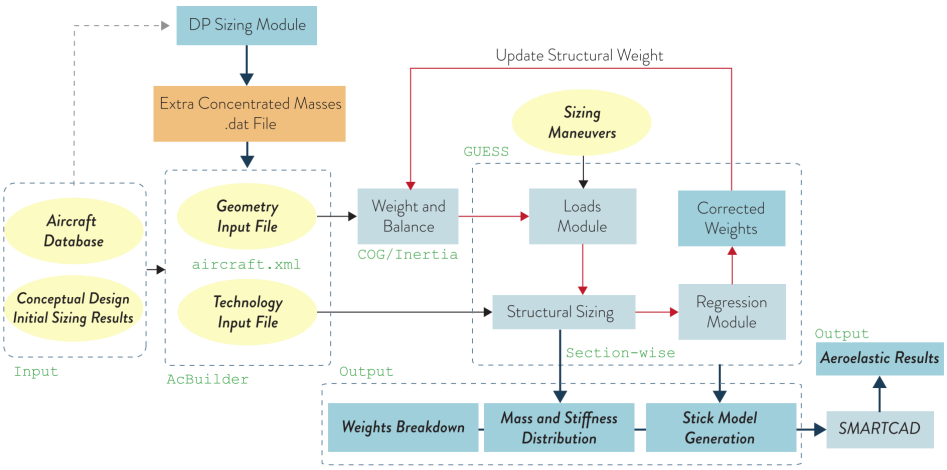

Fig. 6.1: *NeoCASS* road map

The fuselage has been modeled with **z-stiffened shells** with thickness of frames optimized for buckling, whereas lifting surfaces exhibit wingbox layout with semi-monocoque section [46]. By the way, alongside wing structural configuration, it is also possible to specify wing ribs and stiffeners spacing, which in the current analysis have been set to 0.55 m and 0.1 m.

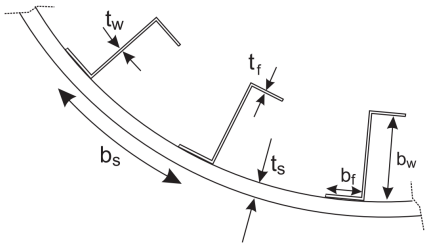

Fig. 6.2: Fuselage z-stiffened shell

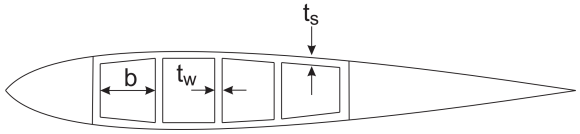

Fig. 6.3: Lifting surface wingbox configuration

6.1.1 Fuselage and cabin design

Every internal component is placed inside the fuselage according to its size, function and effect on aircraft balancing in every loading condition. Ultimate result is shown in Figure 5.15.

In order to let PGS unloading in a fast and easy way, it is **placed in the nose**, covered by a lightweight fairing with air intakes sized according to *Rotax* installation manual. Since thermal unit is not connected to a propeller, it can be mounted in desired orientation if complying with operating limits. Nose is slightly tilted down to improve aerodynamics, have an inclined firewall frame to increase safety in a crash landing [66] and for better pilot visibility.

"Hybrid bay", EPMS units and water pumps are placed under baggage compartment, exploiting baggage door opening for battery packs substitution. Internal dimensions of *C-172* and *PA-28* have been taken as reference to design a comfortable and ergonomic aircraft for four occupants. This novel design assures optimal visibility in every direction: vertical field of view from the cockpit window is 113 deg, of which 12 deg are below the horizon, as shown in Figure 6.4.

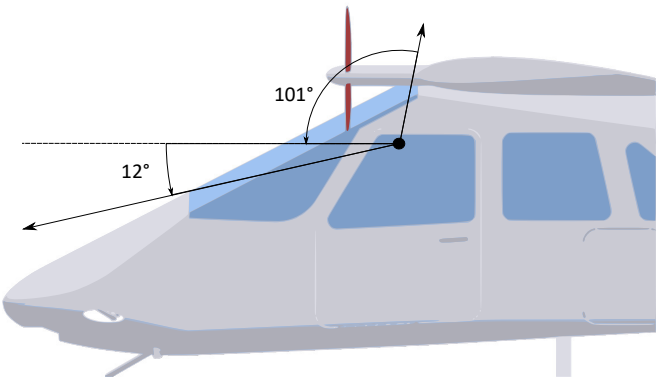

Fig. 6.4: Pilot eyesight representation on vertical plane

6.1.2 Materials selection and properties

A preliminary comparison between aluminum alloy and composite materials has been conducted. Composite construction could provide a slightly lighter airframe, but advantages of a metallic one are:

- cheaper cost of production. Eastlake & Blackwell model, updated by [3] in 2012, considers an increase between 30% and 45% of procurement cost for a composite aircraft;
- simpler and well-diffused realization, with minor repairing potentially done at airfield;
- in a composite structure a copper net must be drowned in order to limit lightning consequences;
- higher aluminum thermal conduction is used for BPs cooling and anti-ice system.

Eventually, previous statements drove the choice to **metallic construction**. A combination of **Al-2024-T3** and **Al-7075-T6** has been chosen for structural components, whose mechanical properties serve as inputs for *NeoCASS* sizing. Values are reported in 6.1, taken from MIL-HDBK-5J.

Property	**Al 2024-T3**	**Al 7075-T6**
Density [kg/m^3]	2780	2810
Tensile modulus [GPa]	73.1	71.7
Shear stress [MPa]	283	331
Ultimate tensile stress [MPa]	483	572
Yield tensile stress [MPa]	345	503
Components	Lifting surfaces skins Lifting surfaces webs Fuselage shells	Fuselage frames

Tab. 6.1: Materials properties of structural components

Al 2024-T3 is suitable for high-strength tensions. It has good fracture toughness, slow crack growth, and good fatigue life compared to other aluminum alloys. Al 7075-T6 has higher strength but also lower fracture toughness and fatigue resistance. This is why it has been employed only for fuselage frames.

6.2 Initial sizing

Previous estimations of MTOW and MEW center of gravity position, moments of inertia and total weight are required to identify the inertial loads to be applied during the sizing maneuvers routine implemented in the module called *GUESS*.

Module *GUESS* generates the structural stick model, performs structural sizing and generates a finite-element mesh to be used in aeroelastic analysis. The approach is the one introduced by [47] for wing and fuselage sizing and extended to other structural components by *NeoCASS* developers. For this approach, the weight estimate is driven by material properties, load conditions and vehicle size and shape, considering classic failure modes based on maximum stress and/or instability. The analysis is performed station by station, giving as result minimum distributed

integrated weight capable of withstanding most critical loads as well as the estimation of the stiffness distribution of the whole airframe.

During the sizing process, shear and bending loads are determined along the fuselage and on the lifting surfaces through Vortex Lattice Method (VLM), whereas Doublet Lattice Method (DLM) manages to provide oscillatory loads estimation, crucial for flutter assessment. Stability and control derivatives are computed enforcing the method reported in [67].

Once the load-carrying structural weight is computed, the overall weight of each component is corrected through statistical regressions in order to add extra weight related to secondary structural elements not included before, such as control surfaces. Then, the corrected weights are fed-back to update the estimations of non-structural masses and refresh the inertial loads, to continue the iterative process until convergence is achieved.

6.3 Sizing maneuvers and V-n diagram

Due to absence of specifications in Amendment 64 of FAR 23, the previous edition has been taken into consideration to develop $V-n$ diagram. One aircraft of the family must be certified under "**utility**" category, hence limit positive load factor is $\boldsymbol{n_{max} = 4.4}$ and limit negative load factor is $\boldsymbol{n_{min} = -1.76}$.

The loading scenario is performed at MTOW and includes the set of maneuvers described in Table 6.2. A safety factor of 1.5 is applied to each load case.

ID	Condition	Ref.
1-4	Maximum positive load factor @ V_C, V_D at different height	§23.333
5-6	Flaps extended @ V_F with $n = 2$ and gusts	§23.345
7-12	Sudden aft-forward elevator control inputs @ $V > V_A$	§23.423
13-24	Yawing maneuvers (max rudder deflection, sideslip)	§23.441
25-28	Aileron abrupt deflection	§23.455
29-32	Gusts @ V_C, V_D	§23.333
33	Tail-down landing	§23.481

Tab. 6.2: Set of sizing maneuvers

The sizing approach undertaken has been performed through iterations. In fact, a *GUESS*

value for MTOW was needed to develop the flight envelope and set sizing maneuvers. The structural weight computed to withstand loading conditions was then used to update MTOW estimation. The process was repeated till guessed value coincided with the one computed, giving as results the airframe characterization as well as $V-n$ diagram, which is reported in Figure 6.5.

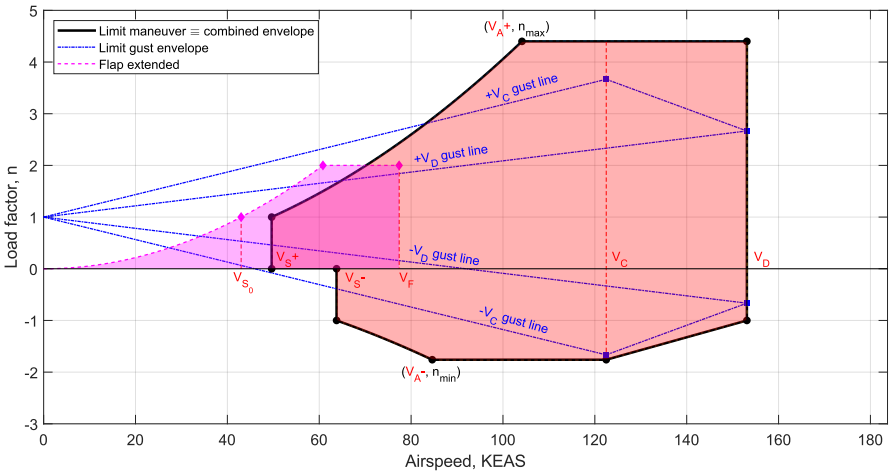

Fig. 6.5: $V-n$ Flight envelope

Limit gust envelope never contributes to combined envelope. At the same time it is necessary to highlight that design cruise speed is slightly higher than optimal and expected cruise speed. Regulations impose as minimum certifiable cruising speed $V_{C_{min}} = 63\,\mathrm{m/s}$, which was then adopted as V_C. This results in a higher V_D, thus airframe is slightly heavier than expected, but compliance with regulations could not be overlooked.

Loads at different maneuvers* concur to define envelopes for shear force, bending and torsional moment at each given section. For example, Figure 6.6 refers to loads acting on the structural node of the fuselage in correspondence of the wing-fuselage intersection and on the node of the wing at 10% span. Same considerations are applied for each component.

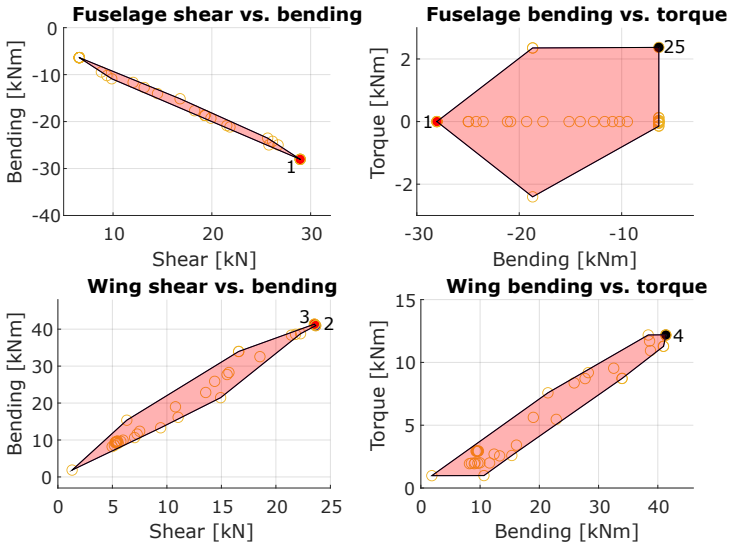

Fig. 6.6: Loads envelope at different maneuvers

*maneuvers ID as in Table 6.2

A graphical representation of **stick-model** and aerodynamic mesh is provided in Figure 6.7, along with a recap of most critical maneuvers for each component.

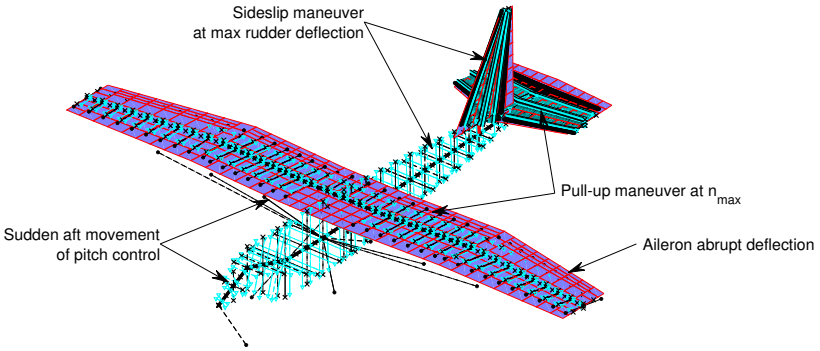

Fig. 6.7: Stick model with critical sizing maneuvers

6.4 Preliminary mass breakdown

Results of structural analysis are compatible with traditional statistical methods, as the ones reported in [2] and [8]. The only visible incompatibility in the adoption of regressions suggested by [47] appears to be the overestimation of secondary masses of the wing. This could be explained by looking at the simple high lift device technology here implemented. Hence, the coefficient of linear regression from primary to total mass of the wing has been reduced, according to the estimation of flaps weight performed following [8].

The relative mass distribution of the fuselage and the wing is reported in Figure 6.8. It shows structural mass reflects positioning of lumped masses, for example in the case of the wing there are local peaks in correspondence of the EMs.

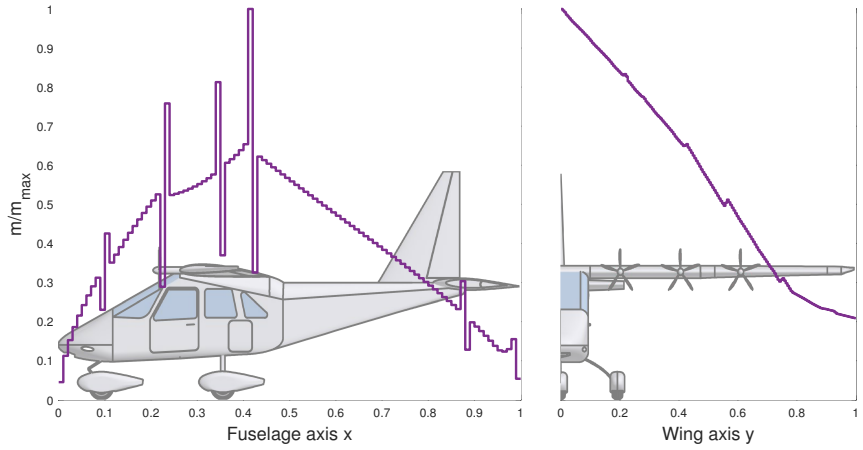

Fig. 6.8: Relative mass distribution along the fuselage and the wing

Table 6.3 specifies aircraft mass breakdown per components, also showed in Figure 6.9. Structural items are *NeoCASS* outputs, while every other entry comes from real values, estimations or statistical regressions. Empty mass comprehends "Hybrid" battery pack but not fuel.

Structure		**Powertrain**	
Wing	128.5 kg	PGS	117.7 kg
Fuselage	67.7 kg	Fuel system	21.9 kg
Horizontal tail	22.7 kg	Electric motors	25.8 kg
Vertical tail	16.1 kg	EPMS and ESCs	10.4 kg
Landing gear	32.8 kg	Hybrid bay with BP	61.9 kg
Furnishing	32.7 kg	Propellers and hubs	13.2 kg
Systems		**Totals**	
Avionic suite	33.4 kg	Airframe	300.5 kg
Oxygen system	1 kg	Airframe and systems	389.1 kg
Flight control system	10.5 kg	Empty mass	618.2 kg
Cooling and anti-ice system	21.8 kg	MTOM	1069 kg

Tab. 6.3: Aircraft components masses breakdown

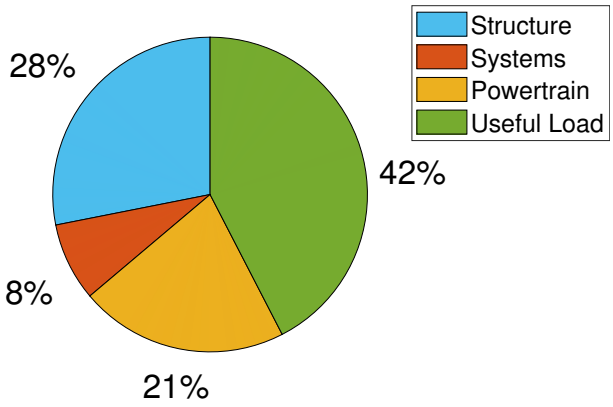

Fig. 6.9: Masses breakdown in macro-sections

6.5 Flutter analysis

NeoCASS aeroelastic solver *SMARTCAD* can perform several kinds of analysis, including flutter assessment. First step is modal analysis of the structure sized through *GUESS* module. In the

current analysis the first 20 modes have been considered (6 rigid modes and 14 deformation modes). Then, flutter problem is modeled as an eigenvalue problem and solved through *continuation method* developed in [48]. It is thus possible to build up $V-f$ and $V-g$ diagrams representation, being $g := 2\frac{\mathfrak{Re}(s)}{|\mathfrak{Im}(s)|}$ stability indicator related to damping factor $\xi = -\frac{\mathfrak{Re}(s)}{|s|}$.
The analysis have been carried out at speed up to 150 m/s, thus well beyond flight envelope.

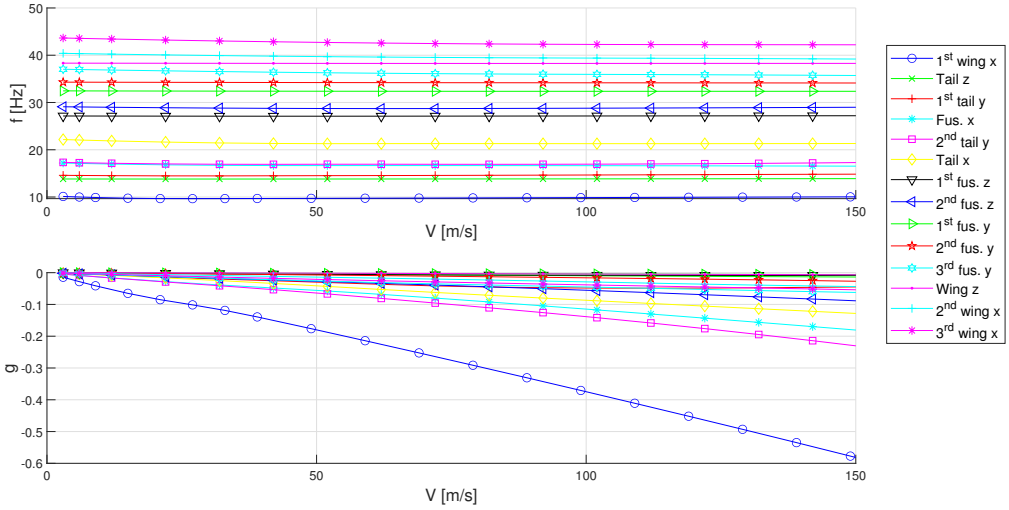

Fig. 6.10: V-f and V-g diagrams for flutter assessment

It is possible to notice there is no mode frequencies coalescence as well no mode stability indicator g ever becomes positive. **Flutter is not supposed not arise** inside and close to designed flight envelope, but of course compliance must be proved through flight testing.

6.6 Landing gear

A student pilot could land in a rough way, providing undesired stresses on the landing systems. On the other hand, saving money in a component with no innovation is essential. Therefore, landing gear sizing is conducted thinking of the simplest and cheapest undercarriage and providing a strong and reliable landing gear.

Configuration chosen is **non-retractable tricycle** with leaf-spring for main landing gear and a small shock absorber in the nose leg. It is cheaper, stronger and more reliable than retractable one. Fairings cover wheels to reduce drag. Main landing gear position guarantees a rotation of 15 deg without touching the ground with the tail during take-off. The position of the nose wheel has been determined combining maneuverability requirements with structural ones. Easy

maneuverability on ground is guaranteed through combined action of nose gear steering and differential brakes.

Tires selection has been done from the *Goodyear* catalog [68] meeting requirements on ground grip, pressure and minimum diameter. Finally, a landing simulation has been done to estimate the braking load needed to stop the airplane and the kinetic energy produced by brakes.
Data of the landing gear structure, tires and brakes are collected in Table 6.4.

Main landing gear position (wrt wing LE)	−30.88 in
Nose landing gear position (wrt wing LE)	56.69 in
Minimum ground-fuselage distance	24.67 in
Wheel track	78.74 in
Wheelbase	87.57 in
Tires model	*Goodyear Flight Special II*
Tires rated inflation	70 PSI
Maximum braking load per wheel	1400 N
Maximum energy dissipated by brakes per wheel	212 880 J

Tab. 6.4: Landing gear data

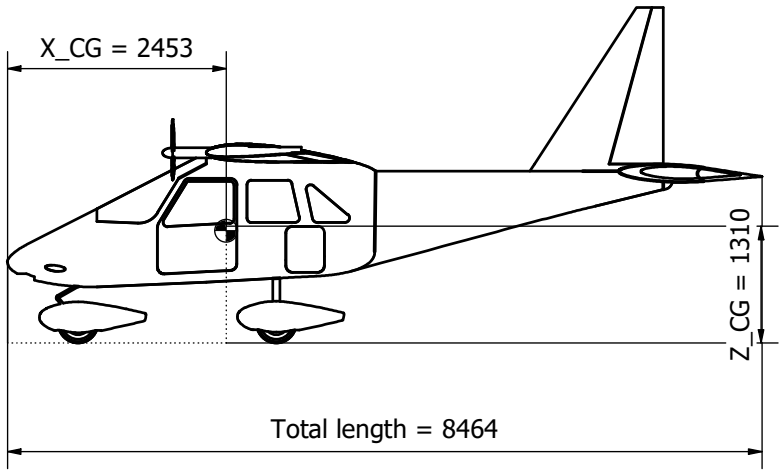

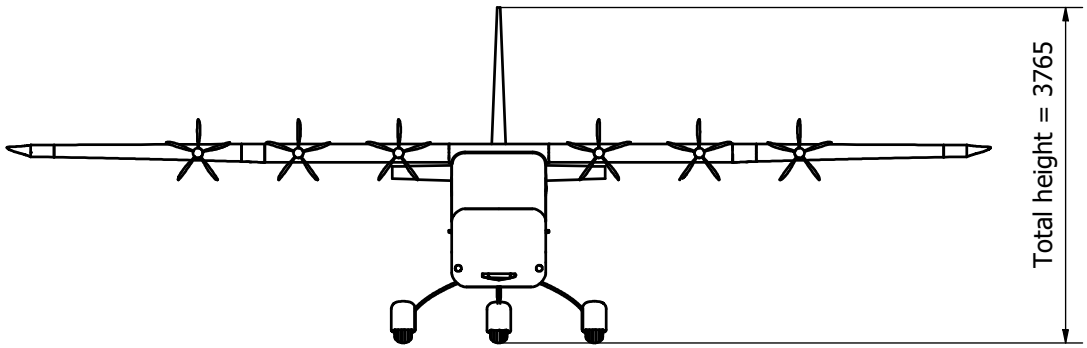

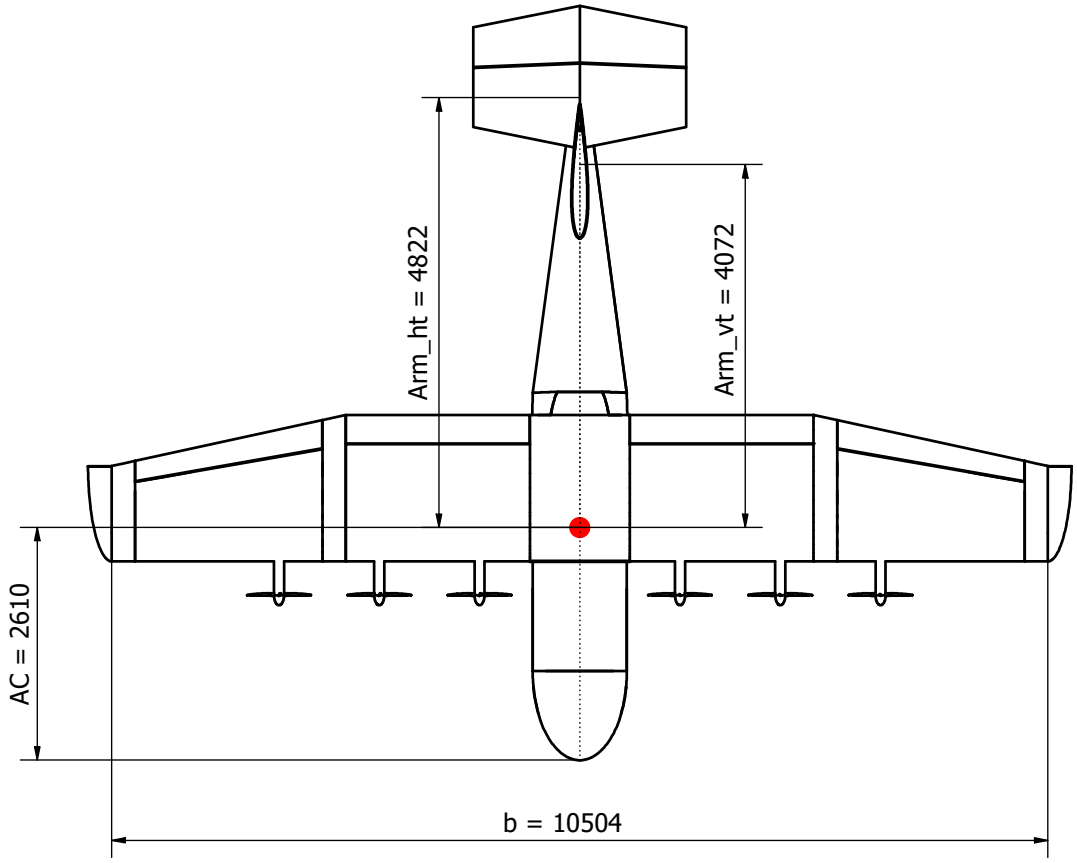

Dimensions are all expressed in [mm]
Scale of 1:60

7. Performance analysis

Current chapter reports an extensive analysis of aircraft performance. These results do not differ between pure-electric and hybrid aircraft configuration, except for integral performances. Final value for MTOM is assumed to be 1069 kg, as this is the ultimate value that respects imposed weight-to-power ratio without affecting stalling speed too much, as shown in Figure 7.1. Aircraft characteristic calibrated airspeeds are instead reported in Table 7.1.

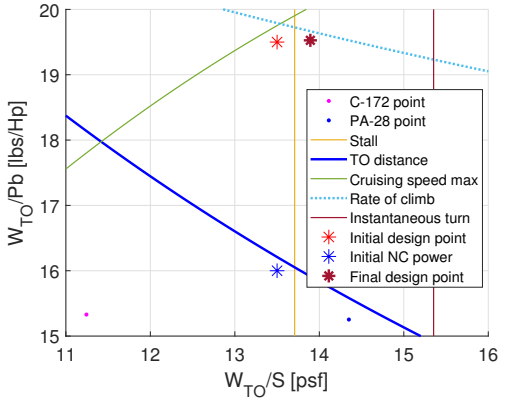

Fig. 7.1: Final point on sizing matrix plot

V_{S0}	45 kt	V_{S1}	54 kt
V_1	44 kt	V_A	104 kt
V_X	59 kt	V_Y	61 kt
V_{NE}	184 kt	V_{MC3}	45 kt
$V_{max\mathcal{R}}$	80 kt	$V_{max\mathcal{E}}$	61 kt

Tab. 7.1: Aircraft airspeeds in CAS

7.1 Take-off and landing performance

Take-off simulation (Figure 7.2) considers wing blowing, flap set to 20 deg and three configurations: MTOM with continuous power, MTOM with non-continuous power and a lightweight one.

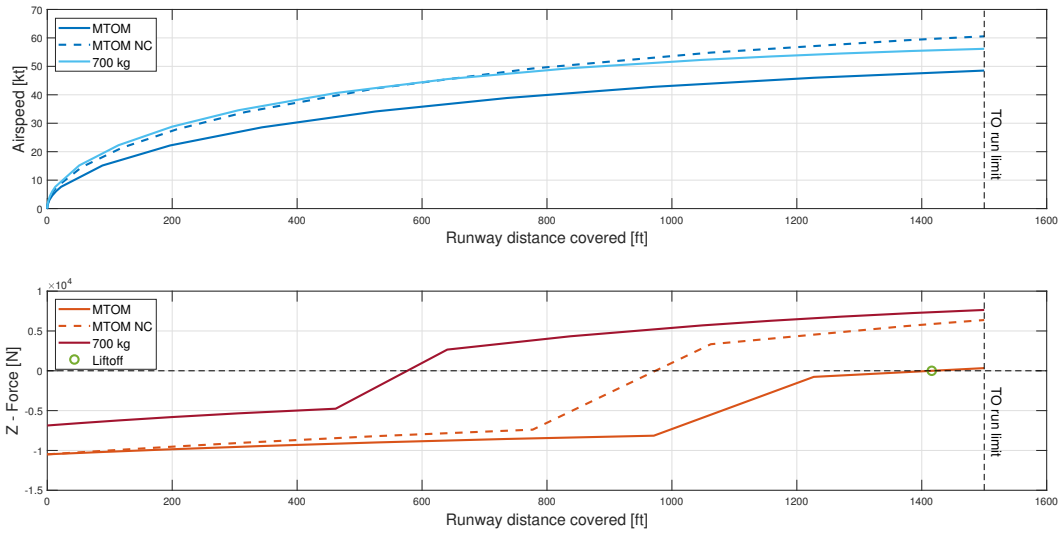

Fig. 7.2: Take-off run simulation

For the MTOM one, rotation is assumed at about 1000 ft, clearly fulfilling RFP requirement. The same analysis is done for landing distance, at an approach speed of 68 kt, full flap setting and MTOM. Soon after touchdown pilot applies maximum breaking action arresting the aircraft in **584 ft**. Exploiting these two simulations it is possible to draw a balanced field length diagram, presented in Figure 7.3.

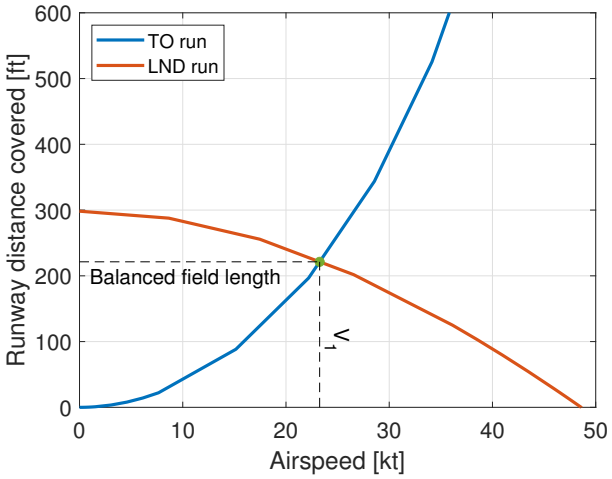

Fig. 7.3: Balanced field length at MTOM

7.2 Integral performance

Range and endurance for pure-electric aircraft are simply derived from total energy stored in BPs, flying respectively at best L/D and best F, accounting for efficiency. Total propulsive system efficiency is 0.745 from singular cell to electric motors shaft, and 0.603 accounting for propellers.

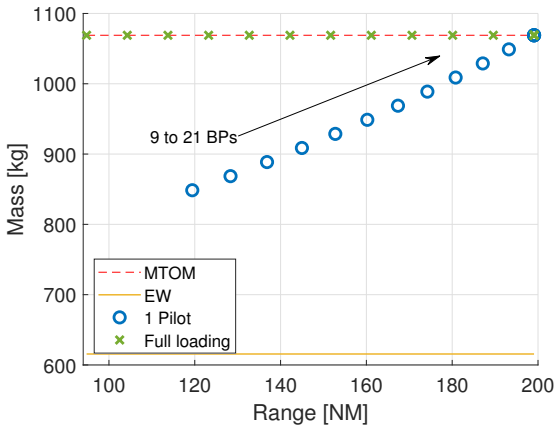

Fig. 7.4: Payload-range diagram in PE

Max range with all BPs onboard is $\boldsymbol{\mathcal{R}_{PE}}$ = **199 NM** flying at $V^{CAS}_{(L/D)_{max}} = 80$ kt whereas max endurance is $\boldsymbol{\mathcal{E}_{PE}}$ = **2 h 48 min** flying at best endurance speed $V^{CAS}_{F_{max}} = 61$ kt.

Payload-range diagram represented in Figure 7.4 is constructed in two situations: the first is with only one pilot on-board and the number of BPs in "Passengers bay" is progressively increased; the second adds payload till MTOM is reached.

In hybrid configuration, integral performance can be determined as in Equation (7.1)

$$\mathcal{R}_{\text{HE}} = \frac{\eta_p}{c_p} \cdot (L/D)_{max} \cdot \log\left(\frac{W_{in}}{W_{fin}}\right), \qquad \mathcal{E}_{\text{HE}} = \frac{\eta_p}{c_p} \cdot F_{max} \cdot \sqrt{2\rho S} \cdot (W_{fin}^{-1/2} - W_{in}^{-1/2}) \,. \quad (7.1)$$

The previous expressions can be employed even for a hybrid aircraft when the "Throttling" usage strategy (explained in Section 7.7) is employed, as this latter directly relates fuel flow and weight loss in flight with flight mechanics quantities. All parameters are known, except for

$c_p := \frac{\dot{W}}{P_B}$. To gather it, brake power is assumed to be equivalent with electric motors power in cruise, while fuel flow is the one of PGS. Resulting values are $c_p = 9.68 \times 10^{-7}\,\mathrm{N/(W\,s)}$ for best range and $c_p = 9.95 \times 10^{-7}\,\mathrm{N/(W\,s)}$ for best endurance setups, which respectively correspond to $\boldsymbol{\mathcal{R}_{HE}}$ **= 1183 NM** and $\boldsymbol{\mathcal{E}_{HE}}$ **= 17 h 38 min**. By way of comparison, conventional *BRM Bristell* has a maximum range of 700 NM with 120 l of fuel available and a similar engine, *Rotax 912*, which has a slightly lower consumption [69].

Payload-range diagrams are made with reference to three different hybrid setups: with just "Hybrid bay", with "Passengers bay" with 6 BPs and with 12 BPs, reported in Figure 7.5.

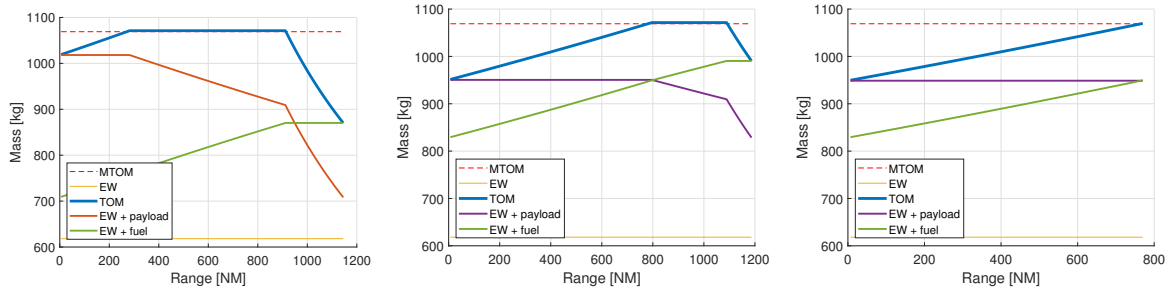

(a) "Hybrid bay" **(b)** "Passenger bay" w/ 6 BPs **(c)** "Passenger bay" w/ 12 BPs

Fig. 7.5: Payload-range diagrams for hybrid configuration

7.3 Flight envelopes

The following analysis is performed for MTOM, assuming standard ISA conditions and CAS≡EAS.

In Figure 7.6 are depicted $V-h$ envelopes for true airspeed and calibrated airspeed, accounting for both continuous and non-continuous power range.

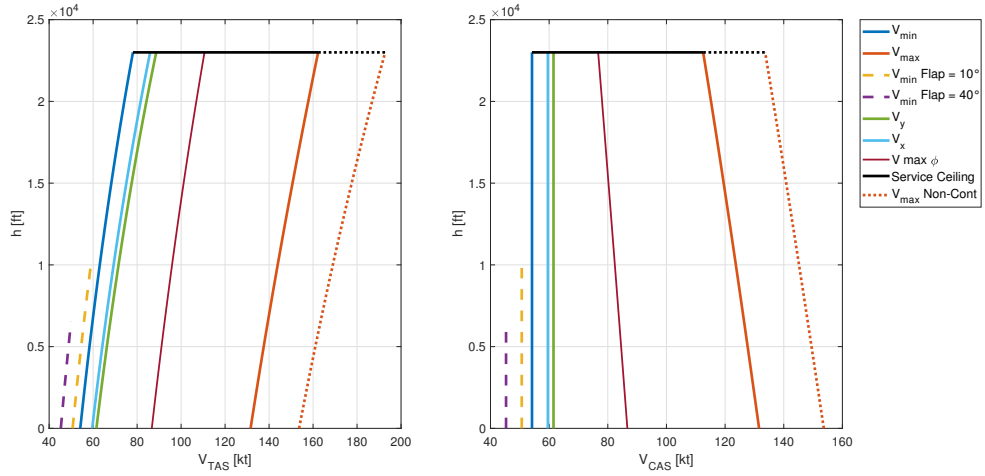

Fig. 7.6: $V-h$ flight envelope

The two envelopes have an uncommon look due to electric propulsion: while altitude increases, specific excess power raises. As there is no propulsive limitation, so absolute ceiling results well above practical altitude for GA employment, **service ceiling** is set to be **23000 ft**, equal to ICE limitation. Speed for maximum climb angle γ_{max} resulted well below minimum flight speed, therefore this is assumed to be $V_X = 1.1 \cdot V_{S1}$.

Figure 7.7 shows Penaud diagrams for thrust and power with different varying parameters, while in Figure 7.8 vertical speed and flight path angle are plotted as functions of speed.

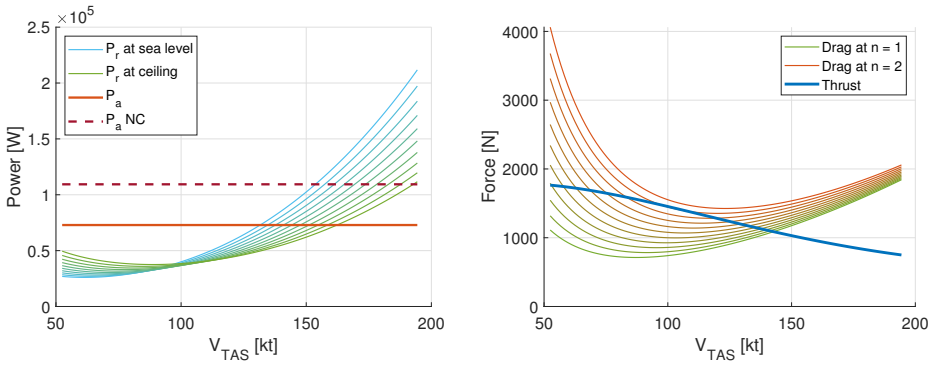

(a) Power available vs. required

(b) Drag vs. thrust at different load factors, $h = 5000\,\text{ft}$

Fig. 7.7: Penaud diagrams

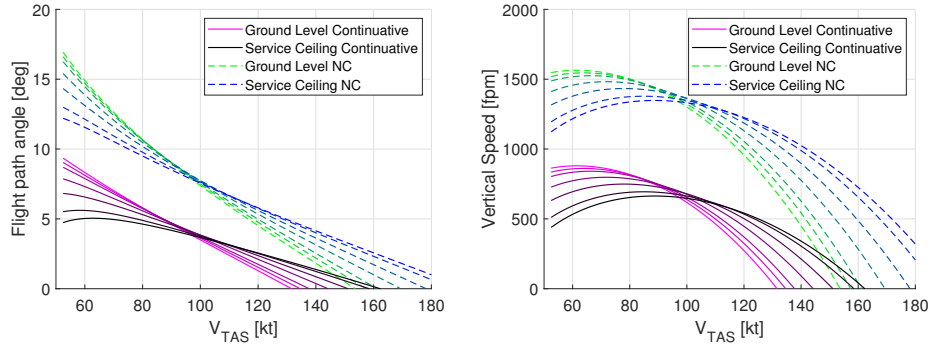

(a) Max flight path angle γ

(b) Max vertical speed V_V

Fig. 7.8: Vertical speed and flight path angle

Similalrly, Figure 7.9 is related to climb performance in most critical emergency case, i.e. with three electric motors inoperative. It is noticeable that even in the worst case it is possible to gain altitude from ground level at $V_{V_{3EMI}} = 195\,\text{fpm}$ or $\gamma_{3EMI} = 1.9\,\text{deg}$ with continuous power, while even at $V^{NC}_{V_{3EMI}} = 537\,\text{fpm}$ or $\gamma^{NC}_{3EMI} = 5.6\,\text{deg}$ exploiting non-continuous motors power.

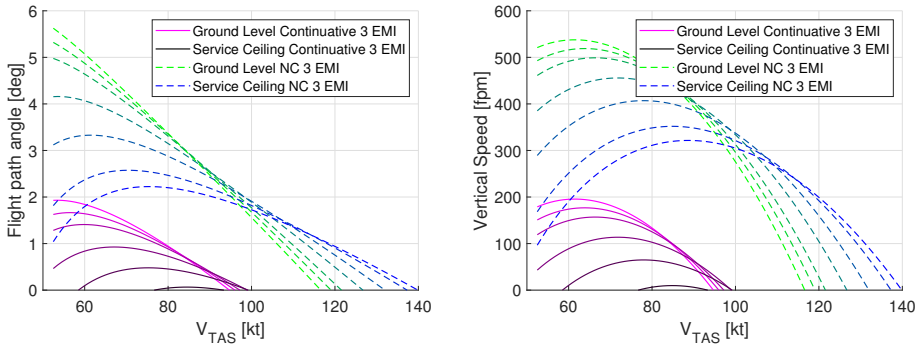

(a) Max flight path angle γ **(b)** Max vertical speed V_V

Fig. 7.9: Vertical speed and flight path angle with three electric motors inoperative

Figure 7.10 reports turning diagrams for a continuous turn.

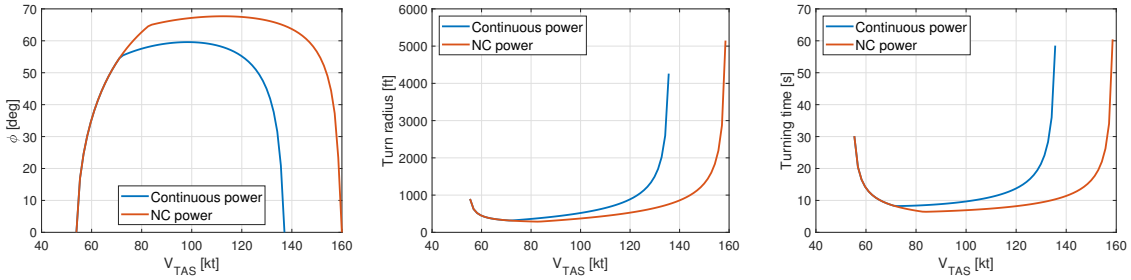

(a) Max bank angle **(b)** Min turn radius **(c)** Min turn time

Fig. 7.10: Turning diagrams for continuous turn

To conclude this analysis, the aircraft is capable of blocking EMs rotation, closing propeller to glide like a sailplane. This can be exploited in descent to save energy and to produce less noise, while in training this can allow engine-out simulation and total energy management. Lift-to-drag ratio is $L/D = 14.7$ and best glide speed is $V^{CAS} = 80\,\text{kt}$. If the aircraft undergoes a complete power loss at 2000 ft above ground level, it can sail up to a distance of 29 400 ft.

7.4 Stability and control

A trainer must be easy to fly in every condition. Every calculation is according to MIL-STD-1797-A [49] and in worst condition. Flying qualities (FQ) must undergo Category A Level 1 limitations. Input for this analysis are DATCOM stability and control derivatives [31].

7.4.1 Longitudinal static stability

In order to condense information regarding trim equilibrium and stability, a very powerful graphical tool has been used, namely Crocco's diagram [50]. The approach undertaken consists of retrieving pitching moment coefficient at trim as a function of lift coefficient and either AOA or elevator deflection. This way it is possible to obtain two different bundles of parallel lines for constant α ("isoclinic lines") or δ_e ("stick lines").

Chosen reference point for pitching moment is the location of the leading edge of the mean aerodynamic chord, in accordance with Crocco's original development. By plotting C_L vs. $-C_{\mathcal{M}_{LE}}$, it can be proven the horizontal line at $C_L = 1$ corresponds to roll axis of the aircraft. To be precise, non-dimensional position is defined with respect to leading edge of the MAC. Again, it can be proven the line passing through the origin and marking non-dimensional position of the center of gravity along horizontal line $C_L = 1$ corresponds to $C_{\mathcal{M}_{LE}}$ at trim for that specific CG location as a function of C_L. This line is referred to as "baricentric line". As a side result, each trim point along this curve corresponds to specific values for α and δ_e.

Crocco's diagram is thus a valid graphical approach thanks to which it is possible to verify excursion of center of mass position is within allowed limitations. In particular, most aft position corresponds to that of aerodynamic center, due to (stick-fixed) static stability criterion. On the other hand, most fore position is retrieved considering the intersection between the isoclinic line for $\alpha = max(\alpha)$ and the stick line for $\delta_e = max(|\delta_e^-|)$. It thus corresponds to the most fore position for which trim at stall angle of attack can be reached.

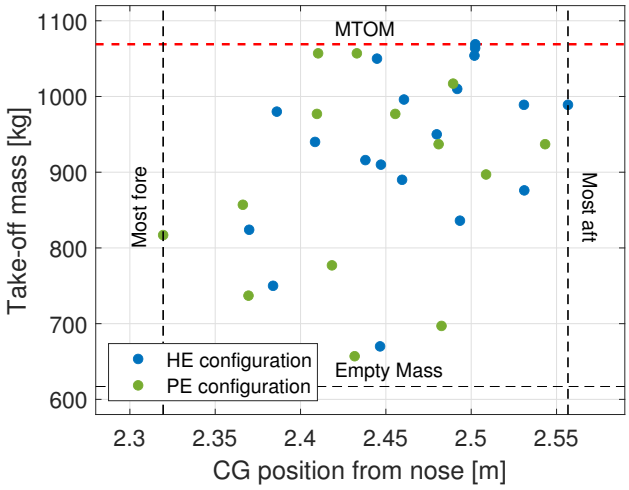

Fig. 7.11: Loading configurations and their effect on take-off mass and CG position

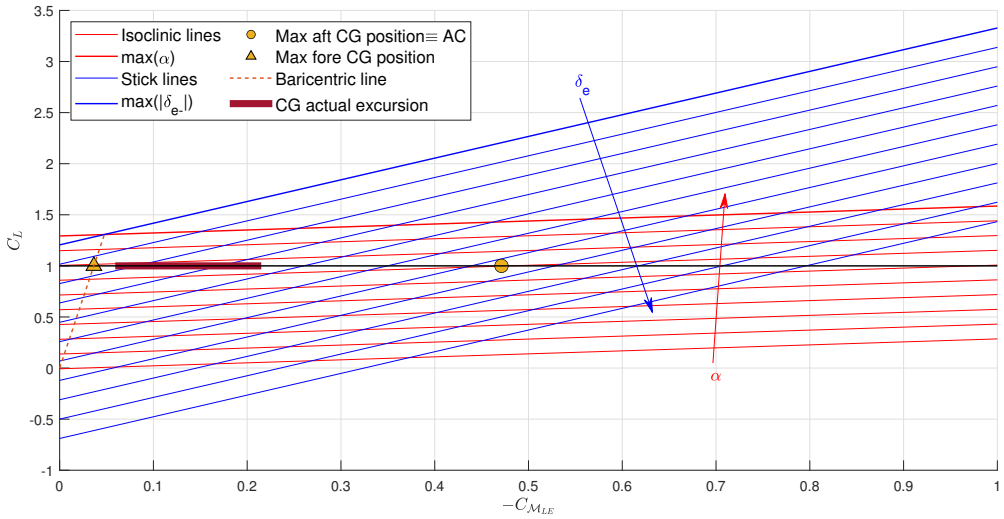

Fig. 7.12: Crocco's diagram with clean configuration

Figure 7.12 thus conjugates Crocco's diagram with actual excursion of aircraft CG, which is based on extreme loading configurations among the ones reported in Figure 7.11. It ensures **stability and control requirements are fully accomplished**. In fact, aerodynamic center is at $\boldsymbol{\xi_{AC} = 0.47}$ and excursion of aircraft CG position, described by the interval $\xi = [0.0593 \div 0.2150]$, is within limits, being static margin $H_n \geq 0.255$.

7.4.2 Dynamic response

An eigenvalue analysis is carried out for decoupled longitudinal and lateral dynamics.

Short Period and Phugoid eigenvalues location in the complex plane are depicted in Figure 7.13: their damping values are $\zeta_{SP} = 0.803$ and $\zeta_{PH} = 0.087$, while their periods are $\mathcal{T}_{SP} = 1.27\,\text{s}$ and $\mathcal{T}_{PH} = 23.37\,\text{s}$. Therefore, aircraft longitudinal dynamics is inside acceptable FQ range.

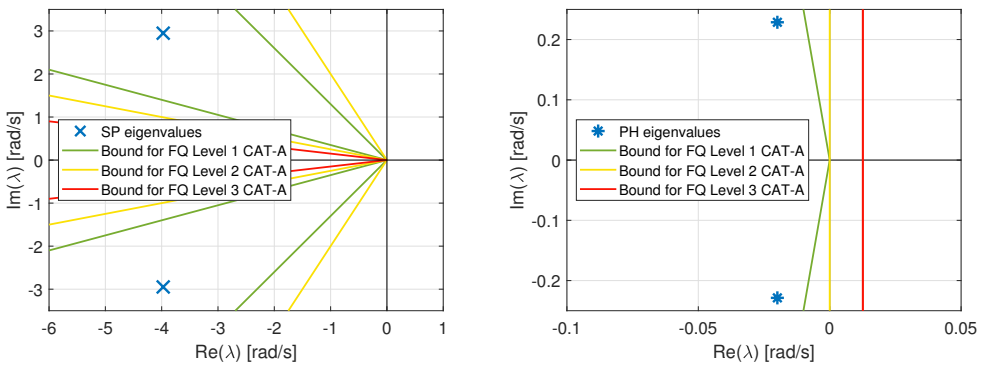

Fig. 7.13: Longitudinal eigenvalues - Short Period and Phugoid

For lateral dynamics, eigenvalues are represented in Figure 7.14. Dutch Roll damping is $\zeta_{DR} = 0.21$ and its period is $\mathcal{T}_{DR} = 2.06\,\text{s}$. Also Roll and Spiral modes are compatible with MIL-STD Level 1 Category A FQ.

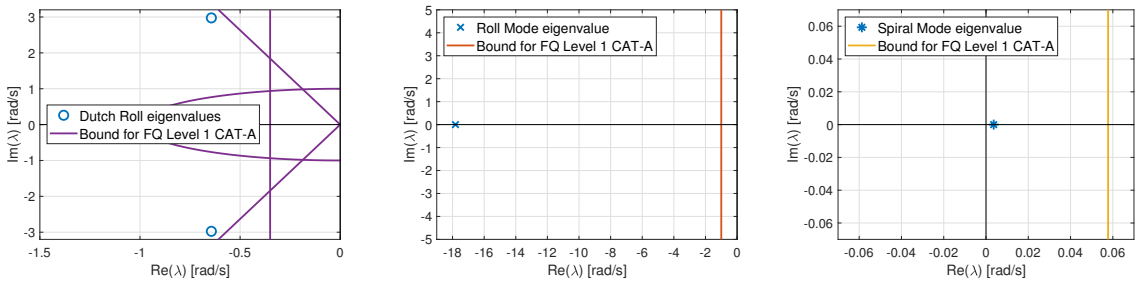

Fig. 7.14: Lateral eigenvalues - Dutch Roll, Roll Mode and Spiral Mode

7.5 Single-engine simulation effectiveness

Solving trim equations it is possible to determine differential power to enforce for SE simulation and resultant flight attitude. Some characteristic working conditions are reported in Table 7.2, combining values of airspeed and differential propeller thrust.

Airspeed V_{CAS}	100 kt	100 kt	68 kt	132 kt
Differential thrust	10%	25%	10%	10%
Angle of attack α	4.38 deg	4.38 deg	11.55 deg	2.25 deg
Angle of sideslip β	0.74 deg	1.86 deg	1.83 deg	0.42 deg
Rudder deflection δ_r	−0.98 deg	−2.46 deg	−2.42 deg	−0.56 deg
Aileron deflection δ_a	−0.06 deg	−0.17 deg	−0.16 deg	−0.04 deg

Tab. 7.2: Trim solution for several flight conditions for SE simulation at MTOM

The asymmetry needed to generate the yawing moment can be produced acting on a singular motor (10% less power on motor #1) or on two (−5% on motor #1 and +5% on #6). The latter allows to reach full nominal thrust.

Sideslip angle induced with SE simulation strongly depends on airspeed and the overall behavior perfectly reflects that of real single-engine aircraft in all aspects.

7.6 Ground noise exposure

In order to understand how this novel design could reduce noise impact in airport proximity, a noise analysis based on *CHANCES* code [51] is carried out. *CHANCES* exploits a source-bundling prediction method which sums contribution coming from airframe, ICE, EMs, propellers.

Purpose of this analysis is to compare noise produced by *Trybrid* with noise produced by one traditional single-engine, *Cessna C-172*, and one twin-engine, *Piper PA-30 Twin Comanche*.

The three aircraft fly the same pattern, namely Milano-Bresso (ICAO: LIMB) circuit, but the *Trybrid* aircraft flies the entire circuit in PE mode. Contour plots for ground noise exposure levels (SEL) are thus reported in Figure 7.15, while in Table 7.3 more emphasis is given to areas interested with different SEL: it emerges the designed aircraft is **quieter than competitors**.

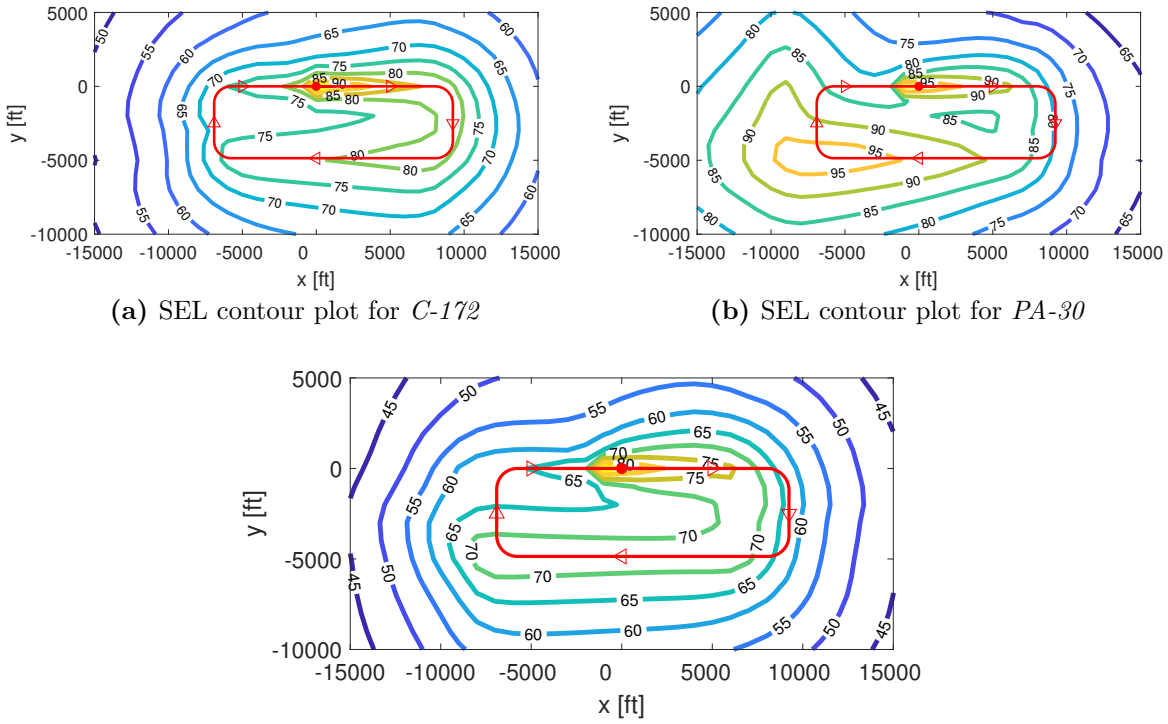

(a) SEL contour plot for *C-172*

(b) SEL contour plot for *PA-30*

(c) SEL contour plot for *Trybrid*

Fig. 7.15: Sound emission levels on ground in Bresso circuit

	60 dB [ft^2]	70 dB [ft^2]	75 dB [ft^2]	80 dB [ft^2]	85 dB [ft^2]	90 dB [ft^2]	95 dB [ft^2]	100 dB [ft^2]
Cessna C-172	$3.37 \cdot 10^8$	$1.68 \cdot 10^8$	$9.80 \cdot 10^7$	$2.72 \cdot 10^7$	$7.26 \cdot 10^6$	$3.63 \cdot 10^6$	$9.07 \cdot 10^5$	0
Piper PA-30	$4.5 \cdot 10^8$	$3.85 \cdot 10^8$	$3.27 \cdot 10^8$	$2.54 \cdot 10^8$	$1.56 \cdot 10^8$	$6.53 \cdot 10^7$	$1.54 \cdot 10^7$	$1.81 \cdot 10^6$
Trybrid	$1.85 \cdot 10^8$	$5.26 \cdot 10^7$	$7.26 \cdot 10^6$	$3.63 \cdot 10^6$	$9.07 \cdot 10^5$	0	0	0

Tab. 7.3: SEL areas for different aircraft, corresponding to Figure 7.15

7.7 Mission simulation

7.7.1 Mission 1: Hybrid long range navigation (sizing mission)

A mission analyzer is developed to simulate every kind of mission assigning loading configuration and parameters to be flown.

First mission to be tested is the sizing mission, with total payload of 345 kg, for a navigation with cruising speed of 101 kt at 10 000 ft for 500 NM, plus 30 minutes of loiter. Transition altitude from and to electric/hybrid mode is set at 4000 ft and rate of climb is set at 700 fpm; at take-off, embarked fuel is 141 l and 3 BPs are in "Hybrid bay". An idealization of mission flight path is reported in Figure 7.16*.

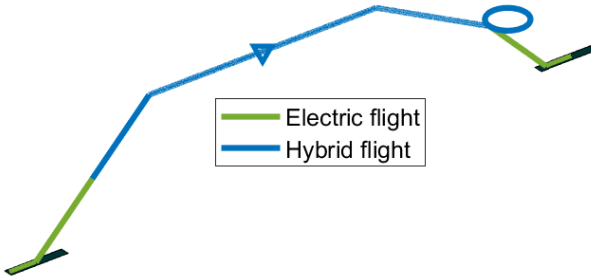

Fig. 7.16: Mission 1 flight path idealization

EPMS units can follow four different strategies:

A **"Sawtooth"**: PGS is switched off when batteries reach a value above a certain percentage of the initial charge, and turned on again when below another one;

B **"Throttling"**: engine throttle is regulated to match energy needs from systems and flight mechanics when it reaches an imposed charge value after climb;

C **"Charge Fading"**: similar to **B**, but with power coming from PGS less than power required, to reach a minimum imposed charge value at the end of cruise;

D **"Charge Catching"**: the opposite of **C** strategy.

Results for every strategy are reported in Table 7.4. Differences in performance between strategies **B**, **C** and **D** are negligible. Table 7.5 summons costs for strategies **A** and **B** while using either *MOGAS* or *AVGAS 100LL*. Strategy **B** is more efficient in terms of fuel usage and battery life cycles, but when accounting for engine TBO and maintenance costs, this gap is filled and overcame thanks to reduced ICE working time, being strategy **A** cheaper than the others. Therefore, if main target is flight cost abatement, **most successful strategy is the "Sawtooth"**.

*proportions are not respected in the representation

Parameter	A	B	C	D
Time of flight	6.28 h	=	=	=
Time of PE flight	3.07 h	42 min	42 min	42 min
Time of PGS on	3.21 h	5.60 h	5.60 h	5.60 h
Total distance	587.6 NM	=	=	=
BP energy at LND	23.3%	62.7%	33.3 %	33.3 %
Fuel needed	103.1 kg	96.2 kg	95.6 kg	94.6 kg
BP life cycles used	9.9	0.9	1.6	1.0

Tab. 7.4: Sizing mission resulting parameters

Parameter	A MOGAS	B MOGAS	A AVGAS	B AVGAS
Recharge cost	1.32 $	0.64 $	1.33 $	0.64 $
BPs TBO	10.29 $	0.98 $	10.29 $	0.98 $
Fuel cost	141.98 $	132.53 $	189.85 $	177.21 $
Engine TBO	44.42 $	78.47 $	44.42 $	78.47 $
Engine maintenance	57.97 $	102.4 $	115.95 $	204.8 $
Airframe maintenance	29.52 $	29.52 $	29.52 $	29.52 $
Total VDOC	285.52 $	344.55 $	391.36 $	491.63 $

Tab. 7.5: Sizing mission cost comparison

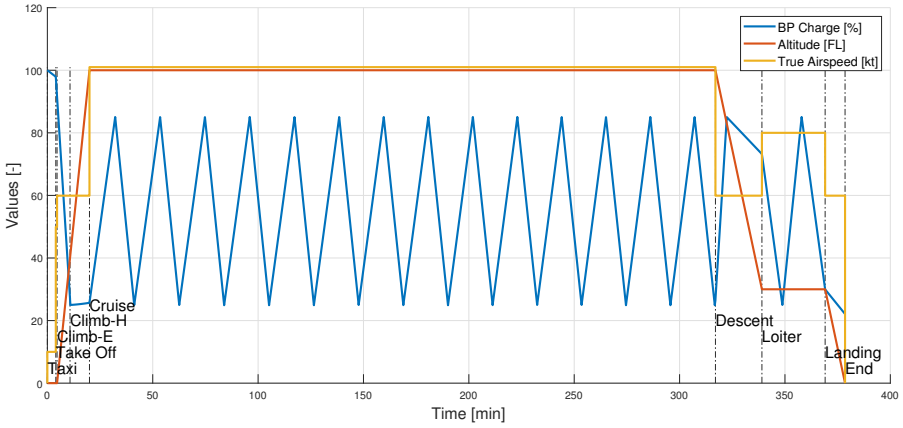

Fig. 7.17: Mission 1 strategy **A** flight parameters

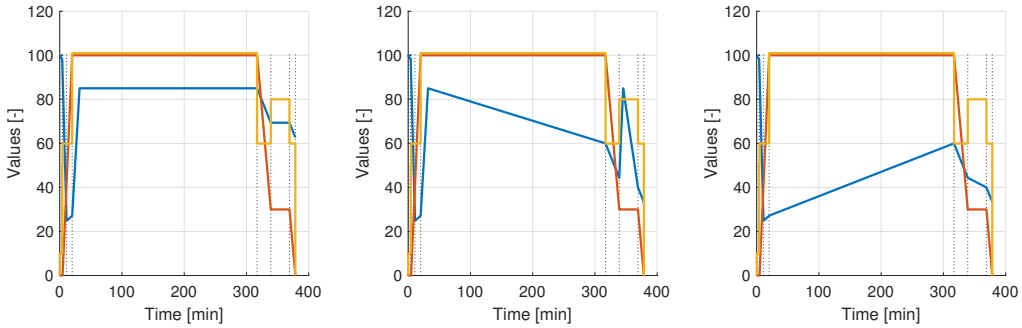

Fig. 7.18: Mission 1 flight parameters for strategies **B**, **C** and **D**

Strategy **A** is also post-processed for what concerns anti-ice system, whose effect is reported in Figure 7.19 for the case air temperature on ground is 0 °C.

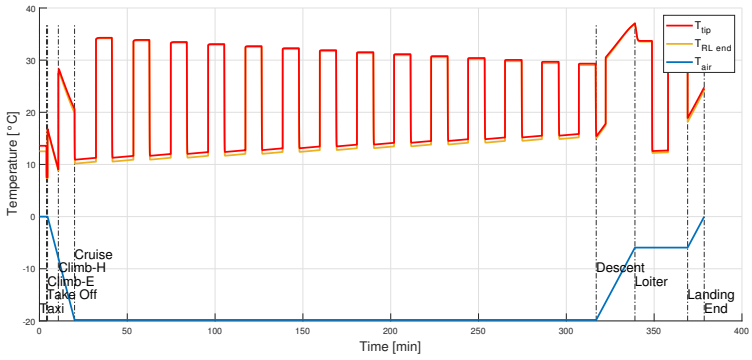

Fig. 7.19: Mission 1 strategy **A** anti-ice effectiveness

Pollutants produced are reported in Table 7.6. These are compared in the same table with pollutants calculated for the case in which a conventional powertrain was installed. Pollutants reduction is better exploited in case more BPs are embarked. For instance with 6 BPs in "Passengers bay" and strategy **A**, CO_2 production falls to 281.4 kg.

Pollutant	A	B	C	D	Conventional
CO_2	316.2 kg	295.1 kg	293.2 kg	290.1 kg	308.5 kg
CO	83.3 kg	75.5 kg	75.5 kg	73.3 kg	80.0 kg
HC	1.2 kg	1.5 kg	1.5 kg	1.5 kg	1.7 kg
NO_X	0.4 kg	0.8 kg	0.8 kg	0.8 kg	0.8 kg
Total social cost	40.9 $	46.4 $	45.8 $	46.6 $	49.9 $

Tab. 7.6: Sizing mission pollutants produced

Mission 2: Pure-electric training mission

Pure-electric flight allows big savings in hourly cost due to less maintenance, absence of TBO counting and fuel consumption, besides low-noise aircraft operations and pollution cuts.

For this flight aircraft is loaded with 17 battery pack of total mass 340.7 kg, capable of an initial charge of 78.4 kW h, with 2 people on-board, zero fuel and no PGS installed. An idealization of the mission is presented in Figure 7.20. The simulated mission includes a 1 h cruise at 90 kt and 3000 ft and one touch & go. Mission totals are reported in Table 7.7, while in Figure 7.22 is shown cooling system effect for the case air temperature on ground is 40 °C.

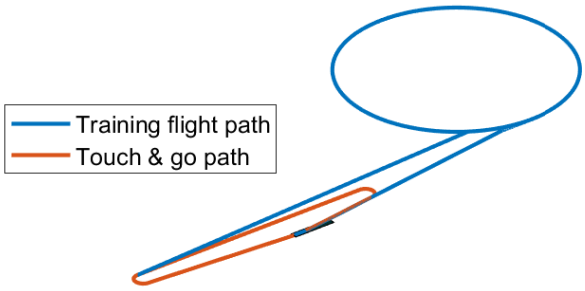

Fig. 7.20: Mission 2 flight path idealization

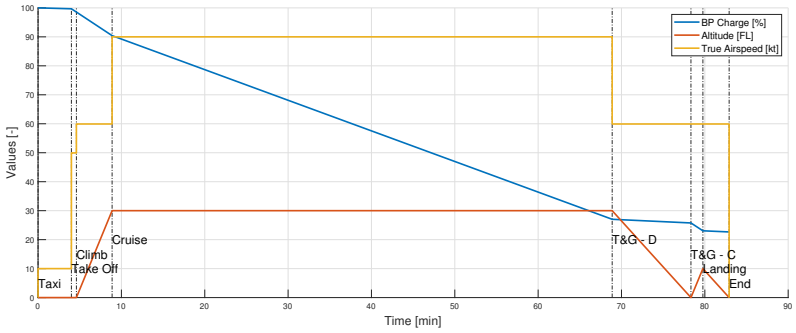

Fig. 7.21: Mission 2 flight parameters

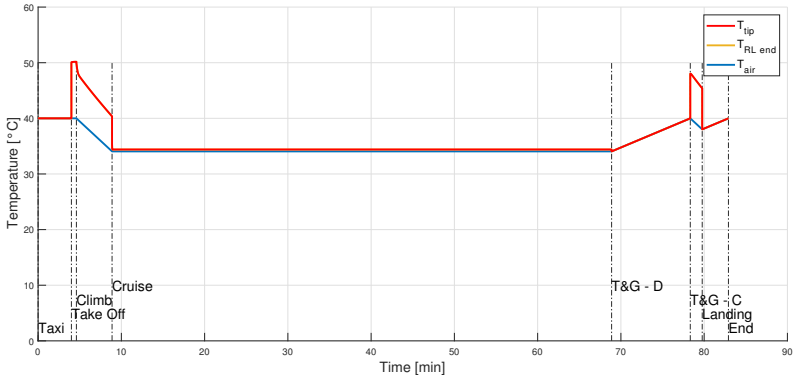

Fig. 7.22: Mission 2 BP cooling system effectiveness

Time of flight	83 min
Total distance traveled	109.1 NM
Energy required	60.6 kW h
Energy in BP after landing	22.7%
Recharge cost	7.58$
BPs TBO cost	4.55$
Airframe maintenance cost	6.47$
Total VDOC	18.6$

Tab. 7.7: Mission 2 resulting parameters and cost

Mission 3: 3-point navigation

FAA regulations specify a cross-country mission landing on at least 3 different airfields must be flown to obtain CPL license [70]. A 3-point navigation mission has thus been simulated. Flight route map is that of Figure 7.23; airport of departure is Daytona Beach International (ICAO: KDAB), from where the aircraft takes-off with student pilot, flight instructor, oxygen tank, 220.4 kg of batteries and 100 kg of *MOGAS*, for a TOM of 1063 kg. First destination is Key West International (ICAO: KEYW), which is more than 250 NM far in straight line, flying at FL 180 and 140 kt true airspeed and an electrical-hybrid transition altitude set at 6000 ft. Pilots take a rest on ground for 1 h. The second leg arrives in Miami Homestead General Aviation (FAA LID: X51), flying at a slower speed of 90 kt and cruising altitude of only 3000 ft, but the aircraft enters in a 10 min loiter due to traffic. Here pilots rest for half an hour while aircraft is refueled up to 60 kg. Last leg back to KDAB is performed at FL 90 and 90 kt, after a climb at 1000 fpm with transition altitude at 3000 ft.

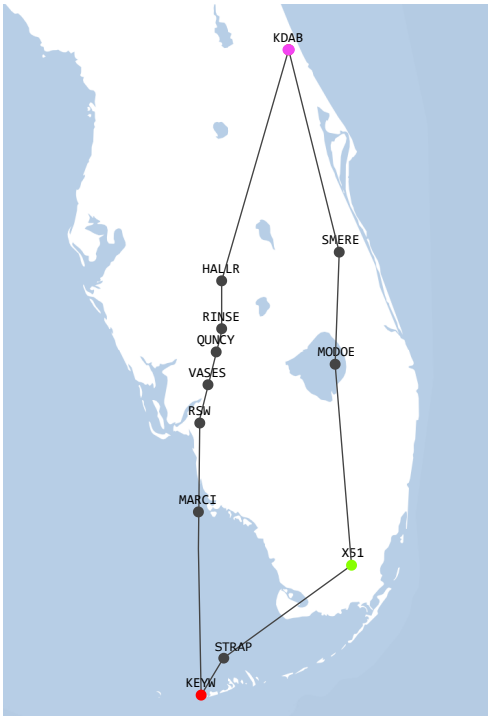

Fig. 7.23: Mission 3 flight map with interested airports and waypoints

All the legs are conducted exploiting **"Sawtooth"** strategy, but, as is visible from Figure 7.24,

in the first leg battery energy level never reach its maximum and this is due to high flight speed. In rest time batteries are never recharged. Mission totals are reported in Table 7.8.

Parameter	Leg 1	Leg 2	Leg 3	Totals
Time of flight	2.85 h	1.25 h	2.53 h	6.63 h
Time PGS on	1.62 h	36 min	1.28 h	3.52 h
Total distance traveled	283 NM	101 NM	224 NM	608 NM
Fuel needed	52.7 kg	19.4 kg	42.0 kg	114.1 kg
Energy in BP after landing	76.0%	77.7%	81.3%	81.3%
BP life cycles used	0.57	0.57	1.33	2.47
Total VDOC	141.92$	55.50$	117.61	315.03$

Tab. 7.8: Mission 3 resulting parameters and cost

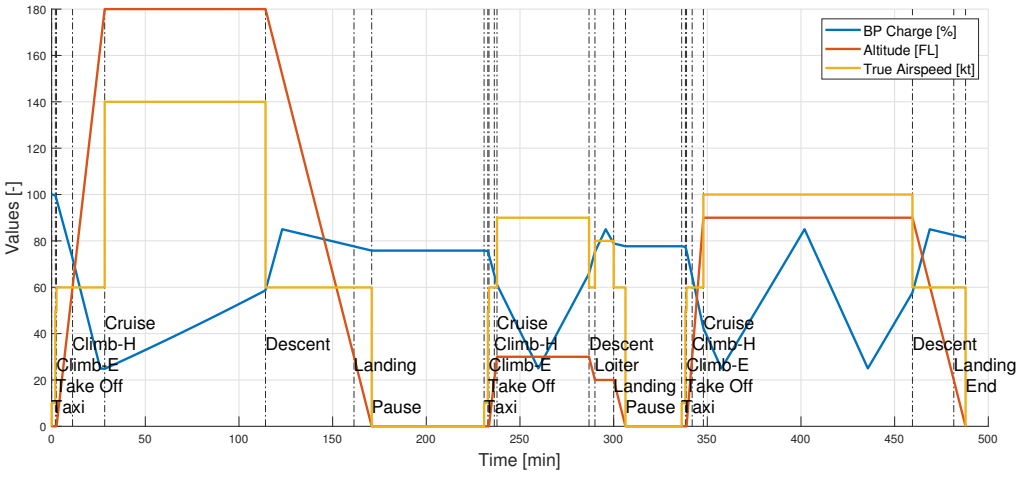

Fig. 7.24: Mission 3 results

8. Cost analysis

8.1 Production costs

A cost estimation method for hybrid-electric aircraft is employed for both production and operating costs [52]. This method is a modification of Eastlake & Blackwell model, already modified by Gudmundsson [3], to consider hybrid aircraft peculiarities. Estimations for electric generator, EMs and EPMS units are included. All other costs are corrected to account for the case under examination, as well. Each known cost has been enforced. Every quantity must be translated in 2025 USD to account for inflation acquiring Consumer Price Index (CPI) [71, 72].

Aircraft can be sold basically in three different configurations, depending on number of BPs acquired. Basic configuration (configuration **A**) is provided with just "Hybrid bay", consisting of 3 BPs. A full operating version (configuration **B**) includes all the three bays, for a total of 21 BPs. To conclude, a third selling variation boastes 3 complete sets of bays to be swapped between flights and serve as spare parts, for a total of 63 BPs (configuration **C**). Configurations **B** and **C** are also offered without PGS, called **PE-B** and **PE-C**.

Production cost breakdown, adopted for price determination, is shown in Figure 8.1. An annual production rate of 100 units/year (which is an high value but complying with analysis in Section 1.3) has been considered. The production of 4 prototypes has been included, for a total of 41 203, 40 234 and 459 232 working hours for engineering (rate 92 $/h), tooling (rate 61 $/h) and manufacturing labor (rate 53 $/h). Total fixed and variable costs respectively

	Total Cost	Cost per Unit
Engineering	$9,037,689.50	$18,075.38
Development Support	$311,471.78	$622.94
Flight Test operations	$30,465.43	$60.93
Tooling	$5,851,366.16	$11,702.73
Certification Cost	$15,230,992.87	
Manufactoring Labor	$58,029,174.35	$116,058.35
Quality control	$12,865,938.39	$25,731.88
Materials / Equipment	$7,181,558.07	$14,363.12
Unit sold in 5 years		500
Quantity Discount Factor		0.631
	Cost per Unit	Cost per Unit with QDF
Fixed landing gear discount	-$9,516.95	-$6,008.58
Power Units & H-BP	$123,014.06	$77,665.61
Propellers	$19,217.21	$12,132.89
Avionics	$51,165.00	$32,303.30
Total Cost to Produce	$370,494.65	$302,708.55
Liability Insurance		$36,325.03
Minimum Selling Price		$339,033.57
Profit	15%	
Configuration A	Configuration B	Configuration C
$389,888.61	$446,515.38	$578,643.47
	Configuration PE-B	Configuration PE-C
	$392,999.98	$525,128.06

Fig. 8.1: Aircraft production costs

amount to 15 230 993 USD_{2025} and 156 458 USD_{2025} per aircraft produced (for configuration **A**).

In Figure 8.2 selling prices are presented with a profit of 15%, in all three different configurations. Figure 8.3 provides a break-even analysis for aircraft sold in configuration **A**. It is clear aircraft manufacturer makes profit starting from the 186^{th} aircraft produced, corresponding to the 22^{nd} month of production.

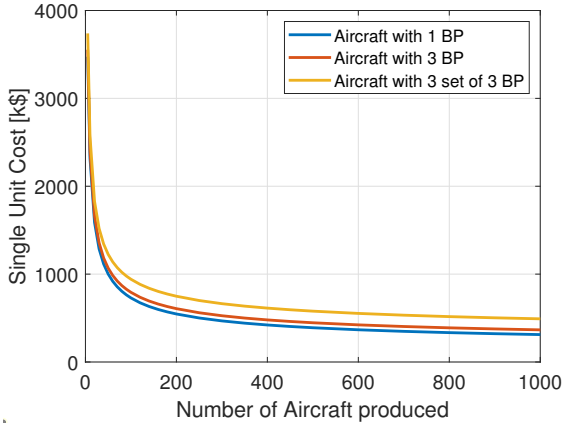

Fig. 8.2: Selling price trend

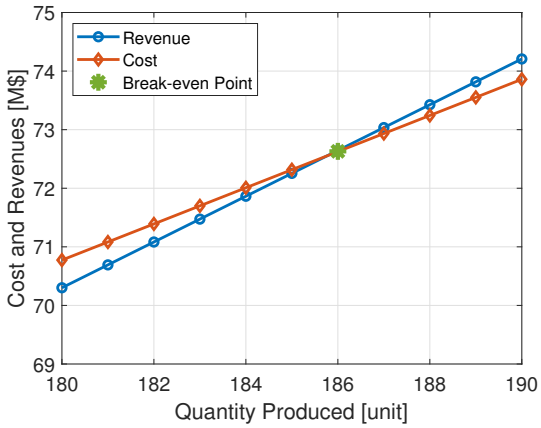

Fig. 8.3: Break-even analysis

Configuration **C** is the most expensive, but it allows to cut down aircraft recharging time and also postpones battery TBO on calendar because flight hours are spread on more battery packs.

8.2 Operating costs

Prices for electric energy [73], *MOGAS* [74] and *AVGAS 100LL* [75] are imposed from mean values of 2020, then converted into 2025 with the right CPI [76].

Operating costs are made of three components: variable direct operating costs (VDOC), fixed direct operating costs (FDOC) and indirect operating costs (IOC).

VDOC – they include fuel, engine maintenance, engine TBO and battery substitution and recharge on ground.

Airframe and systems maintenance are estimated following Gudmunsson. In particular, the ratio between total flight hours and total maintenance hours has been assumed to be $F_{MF} = 0.37$. Then, knowing exact maintenance for ICE, it is possible to correct this ratio to account only for airframe and systems. As a further correction, aircraft extra systems and PGS unloading were considered raising previous value with an extra 20%, so that eventually $F_{MF} = 0.078$.

From this information, hourly rates can be determined depending on fuel and PGS strategy employed: in pure-electric mode this is 14.9 USD_{2025}/h, while in hybrid mode this ranges from 52 USD_{2025}/h for **"Sawtooth"** strategy with *MOGAS* up to 89 USD_{2025}/h in the worst case, dealing with *AVGAS* and strategy **B**. Besides, other costs are landing charges, flight instructor rates, taxes and potential flight school profit.

FDOC – they include depreciation or loan, insurance, annual inspections and storage costs.

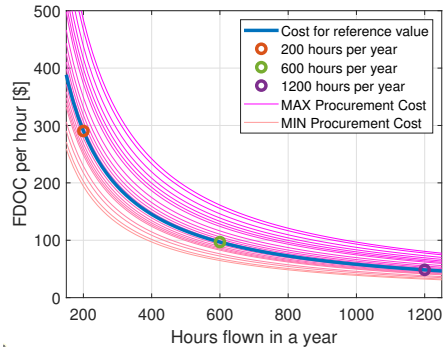

Fig. 8.4: FDOC cost envelope for variation of procurement price

Loan is made according to AOPA [77] on 80% of total aircraft price, to be payed in 15 years with an annual interest of 6%. The Team also contacted an insurance broker for clarification regarding insurance premium. He stated that increase in safety could result in a discount, but uncertainties in the novel design could raise it. Then, Gudmundsson has been followed, while other costs were assumed from typical values of US market.

As *Trybrid* has low mean VDOC, FDOC is a great percentage of total costs and strongly depends on procurement cost. Assuming a production rate of 500 aircraft in 5 years, for a mean of 8.3 aircraft per month, loan cost is 81% of total FDOC (in configuration **C**), a very great value especially compared with older aircraft for whom loan is settled. 578 643 USD_{2025} is set as reference procurement price, as reported in Figure 8.4.

IOC – they consist of general and administration expenses, like employee salaries.

Operating costs are gonna be compared with those of an aircraft of same class or capability. Typical prices for existing aircraft have been investigated with a market analysis with reference to USA. Results of this analysis are presented in Table 8.1 in terms of mean prices at 2020.

Aircraft category	Mean wet price	Example aircraft considered
Light SE	113 $	C-152, PS-28
SE VFR	151 $	C-172, PA-28, DA-40
SE IFR	230 $	C-172, C-182, PA-28, PA-32, SR-20/22
ME IFR	348 $	C-310, PA-34, PA-44, DA-42, P-2006T

Tab. 8.1: Results of market analysis for rental prices

8.3 Examples of business cases

8.3.1 Four student pilots

RFP specified the case of 4 student pilots flying for 75 minutes, interpreted as if each flies 300 hours a year for a total of 1200 hours/year for the aircraft.

Now assume a 10% profit for the flying school. Flight instructor cost can amount for instance to 60 USD for 50 hours, for a total of 3,000 USD. It is also needed to establish the percentage of flights performed in PE mode and which fuel is used in Hybrid mode. Results are reported in Figure 8.5.

In contrast, if pilots flew a *C-152* for the same amount of time this would cost 38 500 USD per year on an aircraft with worse performance and capabilities.

FDOC		
$58,074.00	Hourly FDOC	$48.40
VDOC		
Flight Mode	Percentage	Total Annual Cost
Pure Electric	100%	$4,451.17
20% MOGAS	20%	$6,680.94
40% MOGAS	40%	$8,910.70
20% AVGAS	20%	$7,820.94
40% AVGAS	40%	$11,190.70
Profit		10%
Totals	Price at Year	Mean Hourly Rate
Pure Electric	$20,866.64	$69.56
20% MOGAS	$23,319.38	$77.73
40% MOGAS	$25,772.12	$85.91
20% AVGAS	$24,573.38	$81.91
40% AVGAS	$28,280.12	$94.27

Fig. 8.5: Business case - Four student pilots

8.3.2 PPL and CPL licenses

The following analysis considered the case of acquisition of Private Pilot License and Commercial Pilot License. Reference from mean hourly rate gives a PPL minimum price, flying only with *C-152*, of 5139 USD, while for CPL-IR-ME minimum price is 36 122 USD. Cost calculations are based on nominal hours to get the license, flying missions under 1 hours and 30 minutes in pure-electric mode and the longer in Hybrid mode. Results are depicted in Figure 8.6 and strongly depend on the number of hours yearly flown, as great part of costs are relative to loan.

PPL	Total time	40 h							
FAA	Over 90 Min:	8 h							
School:	AC hours/year	Profit	FDOC	H Hours	PE Hours	MOGAS	Mean Rate	AVGAS	Mean Rate
Small	400	10%	$145.19	8	32	$7,368.01	$184.20	$7,535.21	$188.38
Medium	800	10%	$72.59	8	32	$4,173.94	$104.35	$4,341.14	$108.53
Big	1500	10%	$38.72	8	32	$2,683.37	$67.08	$2,850.57	$71.26
CPL-IR-ME	Total time	250 h							
FAA	Over 90 Min:	60 h							
School:	AC hours/year	Profit	FDOC	H Hours	PE Hours	MOGAS	Mean Rate	AVGAS	Mean Rate
Small	400	10%	$145.19	60	190	$46,458.86	$185.84	$47,712.86	$190.85
Medium	800	10%	$72.59	60	190	$26,495.92	$105.98	$27,749.92	$111.00
Big	1500	10%	$38.72	60	190	$17,179.88	$68.72	$18,433.88	$73.74

Fig. 8.6: Business case - PPL & CPL achievement

If aircraft is flown 1500 hours in one year and *MOGAS* is available, total flying cost to achieve PPL and CPL license are respectively just 2683 USD_{2025} and 17 180 USD_{2025}, including a 10% profit for the school. Again, these costs are spent to fly an aircraft that can be VFR or IFR, ME or SE, can fly with an autopilot and in known icing conditions, can fly in electric mode reducing pollution and noise over cities but also covers great distances in Hybrid mode.

8.3.3 Sport flying

A flying club purchased configuration **PE-C**. An aviation enthusiast with a PPL license flies in electric mode for 15 hours every year just for fun. No profit is expected from the association, just an annual registration fee. Results are proposed in Figure 8.7.

Club:	AC hours/year	Profit	FDOC	Flight Hours	Mean Rate	Annual Cost
Small	400	0%	$132.09	15	$146.92	$2,203.83
Medium	800	0%	$66.04	15	$66.04	$990.64
Big	1500	0%	$35.22	15	$35.22	$528.34

Fig. 8.7: Business case - Sport flying

8.3.4 Depreciation and private owners

Rate of depreciation, residual price and age of resale of the aircraft are parameters extremely uncertain. Nonetheless they have been estimated through comparison with competitor *Cirrus SR-22* (Figure 8.8). Price of used aircraft, expressed as a percentage of the price of the new ($\mathcal{P}_{\%}$), describes a profile over age ($\mathcal{A}$) that can be well approximated with a parabola of analytic expression $\mathcal{P} = a_2\mathcal{A}^2 + a_1\mathcal{A} + a_0$, being $a_2 \approx 0.2$, $a_1 \approx -8$, $a_0 = 100$.

Two friends make the decision of buying this aircraft; Pilot 1 is SE rated, while Pilot 2 is ME IFR rated. Generally their needs are different, but can be met with *Trybrid*. They buy configuration **B**, pay without a loan and plan to sell aircraft 10 years later at 178 000 USD, as assumed according to previous forecast. Difference from procurement and resell prices is spread on the time interval. They

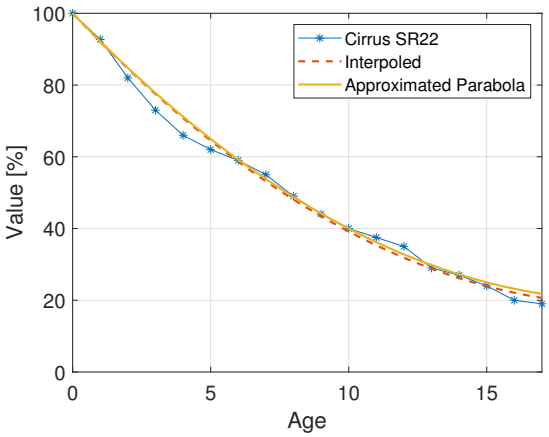

Fig. 8.8: Depreciation analysis for *Cirrus SR-22*

usually fly 100 hours on small distances, hence they could take advantage of pure-electric mode. Then, Pilot 1 flies just 20 hours in Hybrid mode, while Pilot 2 travels all the country for his job, flying for 150 hours every year in Hybrid mode. In his business trips he refills with *AVGAS 100LL* half of the time. As reported in Figure 8.9, pilot one spends only 14 844 USD_{2025} to fly for 120 hours in an aircraft safer than any other SE on the market, while pilot two spends 36 376 USD_{2025} flying 250 hours and exploiting all aircraft possibilities.

	H Hours	PE Hours	Total	PE Cost	H Cost	FDOC	Total cost
Pilot 1	20	100	120	$1,483.72	$1,040.00	$12,320.46	$14,844.18
Pilot 2	150	100	250	$1,483.72	$9,225.00	$25,667.62	$36,376.34
Aircraft Total	170	200	370	$2,967.45	$10,265.00	$37,988.08	$51,220.52

Fig. 8.9: Business case - Private owners

8.3.5 Leasing

The current section analyzes a possible leasing strategy [9]. Assume the lessor is the aircraft producer, while the lessee is a flight club or a private owner. They stipulate a contract for an operating lease, which includes employment of the aircraft for 7 years, maintenance and insurance. Maintenance crew is guaranteed and risk is transferred to the lessor. For these reasons, a lease could be convenient even if not economically cheaper than buying. In Table 8.2 is presented a comparison between leasing and buying hourly dry costs in different situations. Lease or buy comparison is made in the case of buying the aircraft in configuration **C**. These prices account for every expenses apart from fuel and energy costs.

Kind of usage	80-20 PE-HE	50-50 PE-HE	100% HE
200 h/y Lease	360$	364$	371$
200 h/y Buy	320$	325$	332$
600 h/y Lease	127$	131$	138$
600 h/y Buy	114$	118$	125$
1200 h/y Lease	69$	73$	80$
1200 h/y Buy	63$	67$	74$

Tab. 8.2: Lease or buy comparison in different scenarios

8.3.6 Flying clubs usage

A small flying club interested in *Trybrid* should sell their old, familiar, well known *C-172* (or similar) for a brand-new, high-procurement aircraft for whom their technician must be updated. Since operating costs of this aircraft are really low, members will fly more than ever. Furthermore, aircraft have more capabilities, giving to the flying club school the possibility of enlarging their pool of users, shortly rising total flight hours to higher values, cutting down rental rate.

This is also the right choice for medium or big flight clubs. They can sell one SE and one ME to replace them with *Trybrid*, saving money through less hangar space rental, paying one annual insurance, doing less total maintenance. Having an hourly rate lower than normal ME, this can be flown more, at same price. Another way is substitution of two SE and one ME: it is possible to buy just 2 aircraft leaving one always in PE and the other in Hybrid configuration, minimizing technician intervention and costs, or even buy just 1 and maximize hours flown.

8.4 Life Cycle Cost

Life cycle cost is the cost of developing, purchasing, operating and disposing of an aircraft fleet, depending on number of aircraft produced and number of hours flown.

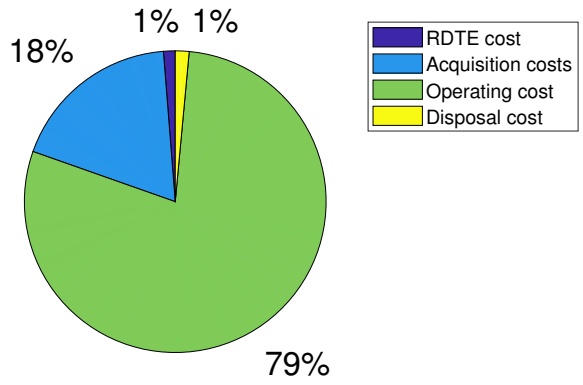

Fig. 8.10: Life cycle cost example

Figure 8.10 shows life cycle cost for one aircraft used in a flight school 1200 h every year for 20 years, running 30% of the time on *MOGAS* and remaining in PE. Percentage are based on 500 aircraft produced and disposal cost is assumed to be 1% of the total life cycle cost. For this specific case, total life cycle cost of singular aircraft is estimated to be 2 432 931 USD.

9. Certification and safety

9.1 Certification

Aircraft is required to be certified under FAR-23. This regulation has recently changed, making an openness towards innovation to respnde to recommendations of 2009 [43]. Anyway, this is still not sufficient to cope with latest technological developments as for electric or hybrid aircraft, also in *NASA*'s opinion [53].

Focal point of certification is safety. There are two main critical certification issues in this project: PGS unloading and single-engine simulation, both for aircraft certification and pilot training and flying with different ratings.

For PGS unloading and substitution with BPs bay an agreement can be negotiated accounting for mitigating actions and rightfully planning the substitution. Since weight, performance, inertia and balance in the two versions are the same, flight testing can be conducted only for one the two versions.

For the single-engine simulation, the primary difference from a conventional aircraft is to demonstrate the reliability of all the systems. Main obstacle is to acknowledge hours flown in SE mode to train SPIC for SEP certificate or simply by a single-engine rated pilot. This is not directly related to certification, but to pilot's regulation. It is desirable that, consequently to an openness of FAR-23, the same could be followed also for CFR Part-61 and for the entire regulation to include newer technological development.

9.2 Safety and risk assessment

In the current work many risk affecting aircraft and occupants safety have been considered. These are schematized in Table 9.2 along with mitigating actions undertaken and their probability and severity before and after mitigation actions [10]. In accordance with ICAO risk matrix in Table 9.1, the level of risk of every considered hazard is within acceptable limits.

	Catastrophic	Hazardous	Major	Minor	Negligible
Frequent	5A	5B	5C	5D	5E
Occasional	4A	4B	4C	4D	4E
Remote	3A	3B	3C	3D	3E
Improbable	2A	2B	2C	2D	2E
Extr Improbable	1A	1B	1C	1D	1E

Tab. 9.1: Risk matrix from ICAO STD

Risk	Probability	Severity	→ Risk mitigation →	Probability	Severity	Compliance
One EM out	Improbable	Minor	EPMS management	Improbable	Negligible	2E
Three EM out	Extr. impr.	Major	EPMS management Emergency LND	Extr. Impr.	Minor	1D
Total power loss	Improbable	Catastrophic	Integrated Power System Emergency LND	Extr. Impr.	Hazardous	1B
PGS fail	Improbable	Hazardous	Energy from BPs Emergency LND	Improbable	Minor	2D
BP Fail	Improbable	Hazardous	Energy from PGS and remaining BPs Emergency LND	Improbable	Minor	2D
EPMS Fail	Improbable	Hazardous	Second EPMS control	Improbable	Minor	2D
Midair collision	Improbable	Catastrophic	ATC and Trafic Advisory system	Extr. Impr.	Catastrophic	1A
Ice formation	Remote	Hazardous	Anti-ice system	Extr. Impr.	Hazardous	1B
Inadvertent Spin	Improbable	Catastrophic	EPMS Panic button	Improbable	Minor	1D
Bird-strike	Remote	Hazardous	Anti-bird-strike System EM number	Improbable	Major	2C
SE rated pilot flying in ME mode	Occasional	Major	Checklist, instrumentation, alerts, EPMS manage	Improbable	Minor	2D
Thermal syst. fail	Improbable	Major	Redundancy Emergency LND	Improbable	Minor	2D
Crash landing	Improbable	Hazardous	Tilted firewall, fuel tanks & G2000 AoA protection	Extr. Impr.	Major	1C

Tab. 9.2: Effect of mitigation on risk and compliance

10. Conclusion

To innovate in aviation means to accept a great challenge: look beyond the state of the art to improve safety, performance and economic and environmental sustainability. *Trybrid* incarnates this concept: one single aircraft model capable of offering handling qualities of a single-engine with the safety of a multi-engine. One aircraft capable of offering training in two different categories for the price of one airplane only. One aircraft capable of offering a flight cost lower than any other competitor.

The new "Switch concept" overcomes the dualism between single-engine and multi-engine. A patent application has been registered for this unpublished feature. In this application, six electric motors simulate by hardware and software the dynamics of a single-engine airplane.

Safety is the keyword: a single-engine pilot will never operate in unknown conditions.

In pure-electric mode *Trybrid* flies with zero emissions. Thanks to thermal engine integration, the bottleneck of battery low energy density is widely overcome and both single-engine and multi-engine requirements are satisfied. High propulsion efficiency allows to take off in less than 1500 ft, to reach the maximum cruise speed of 160 kt at high altitude and to extend ferry range over 1100 NM. In addition, *Trybrid* is capable of doing semi-autonomous flight and it is equipped with an innovative anti-ice system.

With *Trybrid* for the first time in the history a flight school will train pilots for single-engine and multi-engine rating operating just one aircraft, combining economical benefits with safety and performance advantages of innovative technology.

Bibliography

Books

[1] J. Roskam. *Airplane design*. DARcorporation, 1985.

[2] D. Raymer. *Aircraft design: a conceptual approach*. American Institute of Aeronautics and Astronautics, Inc., 2018.

[3] S. Gudmundsson. *General aviation aircraft design: Applied Methods and Procedures*. Butterworth-Heinemann, 2013.

[4] A. K. Kundu, M. A. Price, and D. Riordan. *Conceptual Aircraft Design: An Industrial Perspective*. Wiley, 2019.

[5] T. I. Yacovitch et al. *Exhaust emissions from in-use general aviation aircraft*. Project 02-54. 2016.

[6] M. H. Sadraey. *Aircraft design: A systems engineering approach*. John Wiley & Sons, 2012.

[7] B. N. Pamadi. *Performance, stability, dynamics, and control of airplanes*. American Institute of aeronautics and astronautics, 2004.

[8] E. Torenbeek. *Synthesis of subsonic airplane design: an introduction to the preliminary design of subsonic general aviation and transport aircraft, with emphasis on layout, aerodynamic design, propulsion and performance*. Springer Science & Business Media, 2013.

[9] B. Vasigh. *Foundations of airline finance: Methodology and practice*. Routledge, 2014.

[10] P. C. Cacciabue, I. Oddone, and I. Rizzolo. *Sicurezza del trasporto aereo*. Springer, 2010.

Patents

[11] L. Trainelli, C. E. Riboldi, L. Alberti, D. Pasquali, A. Santeramo, and M. Tombolini. *Velivolo plurimotore simulante un monomotore via hardware e software (Multi-engine airplane simulating a single-engine airplane by hardware and software)*. Italian patent application (priority date May 8, 2020).

[12] W. J. Nolte. *Systems and methods for modular battery replacement in aircraft*. US Patent App. 11/713,463. Sept. 2008.

[13] G. H. Piesinger. *Aircraft bird strike avoidance method and apparatus using transponder*. US Patent 8,279,109. Oct. 2012.

Articles, technical reports

[14] L. Mantecchini. "Airport noise charges and local communities: Application to regional airports". In: *Journal of Engineering Science and Technology* (Nov. 2016), pp. 1518–1527.

[15] S. Min, D. Lim, and D. N. Mavris. "Aircraft Noise Reduction Technology and Airport Noise Analysis for General Aviation Revitalization". In: *15th AIAA Aviation Technology, Integration, and Operations Conference*. 2015, p. 2389.

[16] A. Wangai et al. "Comparison of total lifecycle emission of aircraft with different propulsion system". In: *Repüléstudományi Közlemények* (2017).

[17] J. R. Akridge, Y. V. Mikhaylik, and N. White. "Li/S fundamental chemistry and application to high-performance rechargeable batteries". In: *Solid state ionics* 175.1-4 (2004), pp. 243–245.

[18] M. Kreimeier and E. Stumpf. “Benefit evaluation of hybrid electric propulsion concepts for CS-23 aircraft”. In: *CEAS Aeronautical Journal* 8.4 (2017), pp. 691–704.

[19] A. M. Stoll et al. “Drag reduction through distributed electric propulsion”. In: *14th AIAA aviation technology, integration, and operations conference*. 2014, p. 2851.

[20] C. J. Christensen and B. H. Dunn. “Fleet characteristics of collegiate aviation flight programs”. In: *The Collegiate Aviation Review International* 29.2 (2018).

[21] G. A. M. Association et al. “General aviation statistical databook & industry outlook”. In: (2010).

[22] I. A. T. Association et al. “Guidance material and best practices for the implementation of upset prevention and recovery training”. In: *Montreal, Canada/Geneva, Switzerland: Author* (2015).

[23] T. Kumar et al. “Concerns over use of leaded aviation gasoline (AVGAS) fuel”. In: *Chemical Engineering Transactions* 63 (2018), pp. 181–186.

[24] G. Zubi et al. “The lithium-ion battery: State of the art and future perspectives”. In: *Renewable and Sustainable Energy Reviews* 89 (2018), pp. 292–308.

[25] M. J. Lain, J. Brandon, and E. Kendrick. “Design Strategies for High Power vs. High Energy Lithium Ion Cells”. In: *Batteries* 5.4 (2019), p. 64.

[26] L. H. Saw, Y. Ye, and A. A. Tay. “Integration issues of lithium-ion battery into electric vehicles battery pack”. In: *Journal of Cleaner Production* 113 (2016), pp. 1032–1045.

[27] A. Misra. *Summary of 2017 NASA Workshop on Assessment of Advanced Battery Technologies for Aerospace Applications*. Tech. rep. 2018.

[28] S. Farhad and A. Nazari. “Introducing the energy efficiency map of lithium-ion batteries”. In: *International Journal of Energy Research* 43.2 (2019), pp. 931–944.

[29] L. Goldie-Scot. “A behind the scenes take on lithium-ion battery prices”. In: *Bloomberg New Energy Finance* (2019).

[30] G. Ltd. *Electrical Load Analysis GFC 700 AFCS Diamond DA 40*. Tech. rep. 2005.

[31] R. Finck. *USAF Stability and Control DATCOM (Data Compendium)*. Tech. rep. MCDONNELL AIRCRAFT CO ST LOUIS MO, 1978.

[32] C. E. Riboldi. “An optimal approach to the preliminary design of small hybrid-electric aircraft”. In: *Aerospace Science and Technology* 81 (2018), pp. 14–31.

[33] T. L. Saaty. “How to make a decision: the analytic hierarchy process”. In: *European journal of operational research* 48.1 (1990), pp. 9–26.

[34] T. Rindlisbacher. “Aircraft Piston Engine Emissions Summary Report”. In: *Switzerland: Federal Department of the Environment, Transport, Energy and Communications DETEC Federal Office of Civil Aviation FOCA Aviation Policy and Strategy Environmental Affairs* (2007).

[35] C. Lu. “The economic benefits and environmental costs of airport operations: Taiwan Taoyuan International Airport”. In: *Journal of Air Transport Management* 17.6 (2011), pp. 360–363.

[36] S. Ma et al. “Temperature effect and thermal impact in lithium-ion batteries: A review”. In: *Progress in Natural Science: Materials International* 28.6 (2018), pp. 653–666.

[37] D. Chen et al. “Comparison of different cooling methods for lithium ion battery cells”. In: *Applied Thermal Engineering* 94 (2016), pp. 846–854.

[38] J. Barbagallo. *Pilot Guide: Flight in Icing Conditions*. Advisory Circular AC No: 91-74B. Aug. 2015.

[39] O. Meier and D. Scholz. "A handbook method for the estimation of power requirements for electrical de-icing systems". In: *DLRK, Hamburg* 31 (2010).

[40] I. Abbott, A. Von Doenhoff, and L. Stivers. "NACA Report No. 824–Summary of Airfoil Data". In: *National Advisory Committee for Aeronautics* (1945).

[41] A. Matrone. "Performance-based preliminary sizing of aircraft with distributed propulsion". MA thesis. Politecnico di Milano, 2019.

[42] W. F. Phillips and D. Snyder. "Modern adaptation of Prandtl's classic lifting-line theory". In: *Journal of Aircraft* 37.4 (2000), pp. 662–670.

[43] F. A. Administration. *Part 23 – Small Airplane Certification Process Study*. Tech. rep. 2009.

[44] W. Phillips. "Estimating the low-speed sidewash gradient on a vertical stabilizer". In: *Journal of aircraft* 39.6 (2002), pp. 1088–1090.

[45] A. Ragheb, O. D. Dantsker, and M. S. Selig. "Stall/Spin Mitigation Flight Testing with a Subscale Aerobatic Aircraft". In: *31st AIAA Applied Aerodynamics Conference*. 2013, p. 2806.

[46] A. F. Tellez Velasquez. "On the preliminary structural sizing of innovative regional aircraft". MA thesis. Politecnico di Milano, 2019.

[47] M. C. Chambers et al. "Analytical fuselage and wing weight estimation of transport aircraft". In: (1996).

[48] C. Cardani and P. Mantegazza. "Continuation and direct solution of the flutter equation". In: *Computers Struct* 8 (1978), pp. 185–192.

[49] M. Standard. "Flying qualities of piloted aircraft". In: *US Dept. of Defense MIL-STD-1797A* (1990).

[50] M. Borri and L. Trainelli. "Basic airplane equilibrium and stability revisited". In: *International Conference on Aeronautical Science and Air Transportation (ICASAT) Tripoli*. Vol. 23. 2007, p. 25.

[51] C. E. Riboldi et al. "Predicting the effect of electric and hybrid-electric aviation on acoustic pollution". In: *Noise Mapping* 7.1 (2020), pp. 35–56.

[52] D. F. Finger et al. "Cost Estimation Methods for Hybrid-Electric General Aviation Aircraft". In: *2019 Asia-Pacific International Symposium on Aerospace Technology (APISAT 2019)*. 2019.

[53] H. Schlickenmaier, M. G. Voss, and R. E. Wilkinson. *Certification Gap Analysis*. 2019.

Internet pages

[54] *FAA: Noise Issues*. `https://www.faa.gov/about/office_org/headquarters_offices/apl/noise_emissions/airport_aircraft_noise_issues/`.

[55] *FAA 2018 Survey*. `https://www.faa.gov/data_research/aviation_data_statistics/general_aviation/CY2018/`.

[56] *ICAO Circular on upset prevention training*. `https://www.faa.gov/documentLibrary/media/Advisory_Circular/AC_120-111_CHG_1.pdf`.

[57] *Second-life EV batteries: newest value pool in energy storage*. https://www.mckinsey.com/industries/automotive-and-assembly/our-insights/second-life-ev-batteries-the-newest-value-pool-in-energy-storage.

[58] *MH 116 Airfoil*. https://www.mh-aerotools.de/airfoils/mh116koo.htm.

[59] *Epoxy/Carbon Fiber Composite*. http://www.matweb.com/search/datasheet_print.aspx?matguid=39e40851fc164b6c9bda29d798bf3726.

[60] *Sigraflex APX Flexible Graphite Foil*. https://carrara.it/media/product/DS_Sigraflex_APX_1.pdf.

[61] *Aluminium Oxygen Cylinder*. https://www.preciseflight.com/general-aviation/shop/product/22-cu-ft-aluminum-cylinder/.

[62] *Kelly Aerospace Thermacool*. https://www.kellythermal.com/copy-of-cessna-182t-and-t182t-therm-1.

[63] *Turbulence Modeling Resource*. https://turbmodels.larc.nasa.gov/naca4412sep_val.html.

[64] *Turbulence Calculator*. http://ichrome.com/blogs/archives/342.

[65] *Minimum Standards for Construction of Aircraft Hangars*. https://clevelandtn.gov/DocumentCenter/View/887/Hangar-Construction-Minimum-Standards?bidId=.

[66] *Flying Magazine article on Cirrus SR-22*. https://books.google.it/books?id=bU6O2QwqfcIC&lpg=RA1-PA93&ots=V09qFIANsE&dq=beveled%20firewall%20crash&hl=it&pg=RA1-PA93#v=onepage&q=beveled%20firewall%20crash&f=false.

[67] W. Mason. *Software for aerodynamics and aircraft design*. http://www.dept.aoe.vt.edu/~mason/Mason_f/MRsoft.html#LateralDirectional.

[68] *Goodyear Tires Databook*. https://www.goodyearaviation.com/resources/pdf/databook-6-2018.pdf.

[69] *Big achievements by a small manufacturer*. https://generalaviationnews.com/2017/10/08/big-achievements-by-a-small-manufacturer/.

[70] *FAA Pilot Training Regulation*. https://www.ecfr.gov/cgi-bin/text-idx?m=03&d=12&y=2020&cd=20200323&submit=GO&SID=c02d9828f37d12ccdd2a200a10c7f922&node=se14.2.61_1109&pd=20180727.

[71] *CPI Inflation Calculator*. https://www.bls.gov/data/inflation_calculator.htm.

[72] *CPI Conversion Factors*. https://liberalarts.oregonstate.edu/sites/liberalarts.oregonstate.edu/files/polisci/faculty-research/sahr/inflation-conversion/pdf/cv2015.pdf.

[73] *Average Electricity Prices*. https://www.ovoenergy.com/guides/energy-guides/average-electricity-prices-kwh.html.

[74] *EIA Electricity Data*. https://www.eia.gov/electricity/monthly/epm_table_grapher.php?t=epmt_5_6_a.

[75] *NPR Electricity Prices*. https://www.npr.org/sections/money/2011/10/27/141766341/the-price-of-electricity-in-your-state?t=1575646283589&t=1583431819873.

[76] *Fuel Price Report*. https://www.airnav.com/fuel/report.html.

[77] *AOPA Loan Rates*. https://finance.aopa.org/resources/2016/july/12/sample-aircraft-loan-rates. 2020.